Simulations of Turbulent Boundary Layers with Heat Transfer

by

Qiang Li

October 2009
Technical Reports
Royal Institute of Technology
Department of Mechanics
SE-100 44 Stockholm, Sweden

Akademisk avhandling som med tillstånd av Kungliga Tekniska Högskolan i Stockholm framlägges till offentlig granskning för avläggande av teknologie licentiatsexamen torsdagen den 22 oktober 2009 kl 15.15 i sal E3, Kungliga Tekniska Högskolan, Osquarsbacke 14, Stockholm.

Universitetsservice US–AB, Stockholm 2009

Simulations of Turbulent Boundary Layers with Heat Transfer

Qiang Li
Linné Flow Centre, KTH Mechanics, Royal Institute of Technology
SE-100 44 Stockholm, Sweden

Abstract

A new parallelisation of the existing fully spectral research code has been implemented and validated, and used to perform simulations on massively parallel computer architectures with $\mathcal{O}(1000)$ cores. Using the parallelised code, direct numerical simulations (DNS) and large-eddy simulations (LES) of a spatially developing turbulent boundary layer with and without passive scalars over a flat plate under zero-pressure gradient (ZPG) have been carried out. The Navier-Stokes equations are solved employing a spectral method with up to 600 M grid points. The Reynolds numbers obtained are the highest for a turbulent boundary layer obtained to date with such a numerical setup. An extensive number of turbulence statistics for both flow and scalar fields are computed and compared to the well-established experimental/numerical database. In general, good agreements are found. Premultiplied spanwise and temporal spectra are also used to identify the large-scale motions in the outer part of the boundary layer. The similarities shared by the streamwise velocity and the scalar with $Pr = 0.71$ indicate that they might be generated by the same mechanism. The effects from the different Prandtl numbers and wall boundary conditions are also discussed in detail. Furthermore, the effects of the free-stream turbulence (FST) on the heat transfer on the wall are examined. This problem is of great interest in industrial applications. The momentum and heat transfer on the wall are compared with those obtained with a clean free stream and augmentations of both momentum and heat transfer in the turbulent region are found. In addition, the boundary layer structures are studied and a change of the structures in the outer region are found due to the presence of the free-stream turbulence. By examining the one-dimensional spanwise spectrum, it is speculated that the increase of the momentum and heat transfer are associated with the large-scale motions in the outer layer.

Descriptors: direct numerical simulation (DNS), large-eddy simulation (LES), turbulent boundary layer, passive scalar, large-scale structures, massively parallel simulations

Preface

This thesis deals with spatially evolving turbulent boundary-layer flows including heat transfer. A brief introduction on the basic concepts and methods is presented in the first part. The second part is a collection of the following articles:

Paper 1. Q. Li, P. Schlatter & D. S. Henningson,
Spectral simulations of wall-bounded flows on massively-parallel computers. Internal report (2008)

Paper 2. P. Schlatter, R. Örlü, Q. Li, G. Brethouwer, J. H. M. Fransson, A. V. Johansson, P. H. Alfredsson & D. S. Henningson,
Turbulent boundary layers up to $Re_\theta = 2500$ *studied through numerical simulation and experiments.* Published in Phys. Fluids **21**, 051702 (2009)

Paper 3. P. Schlatter, Q. Li, G. Brethouwer, A. V. Johansson & D. S. Henningson,
Simulations of high-Reynolds number turbulent boundary layers. Submitted to Int. J. Heat Fluid Flow, invited paper from TSFP-6, Seoul, South Korea, 2009

Paper 4. Q. Li, P. Schlatter, L. Brandt, & D. S. Henningson,
Direct numerical simulation of a spatially developing turbulent boundary layer with passive scalar transport. Int. J. Heat Fluid Flow, in press (2009)

Paper 5. Q. Li, P. Schlatter & D. S. Henningson,
Simulations of heat transfer in a boundary layer subject to free-stream turbulence. Published in TSFP-6, Seoul, South Korea, 2009

Division of work between authors
The research project was initiated by Dr. Philipp Schlatter (PS) who has acted as co-advisor and Prof. Dan S. Henningson (DH) who has been the main supervisor.

Paper 1
The code development was performed by Qiang Li (QL) with the help from PS. The paper has been written by QL with input from PS and DH.

Paper 2
The simulation code validation, problem setup and the performance and optimisation tuning was performed by QL and PS. The simulations were performed by PS and the paper was written by PS with input from the co-authors.

Paper 3
The simulation code validation, problem setup and the performance and optimisation was performed by QL and PS. The computations were performed by PS and the paper was written by PS with input from QL, Dr. Geert Brethouwer, Prof. Arne V. Johansson and DH.

Paper 4
The simulations were performed by QL and the paper has been written by QL with input from PS, Dr. Luca Brandt and DH.

Paper 5
The code adaptation and the computations were performed by QL and the paper was written by QL with input from PS and DH.

Contents

Part II

Part I

Introduction

CHAPTER 1

Introduction

Most flows in nature and engineering applications are turbulent and thus characterised by rapid fluctuations in both time and space. Over hundred years have passed and people still do not fully understand turbulence even though it is a universal phenomenon. Examples of such flows include billowing of clouds in the sky, oceanic currents, the flow over the wing of an aircraft or over gas turbine blades. Even the blood flow in our bodies is sometimes turbulent, e.g. the blood in the heart, especially in the left ventricle. Moreover, some flows in everyday life are deliberately made to be turbulent, e.g. coffee stirring, tea pouring and cocktail shaking. Such inherent random and complex characteristics make turbulence to be an intellectual challenge for a great number of scientists and engineers and will continue to pose this challenge in the future. Consequently, a huge amount of theoretical and experimental work has been performed during the last centuries to shed light on this mysterious field.

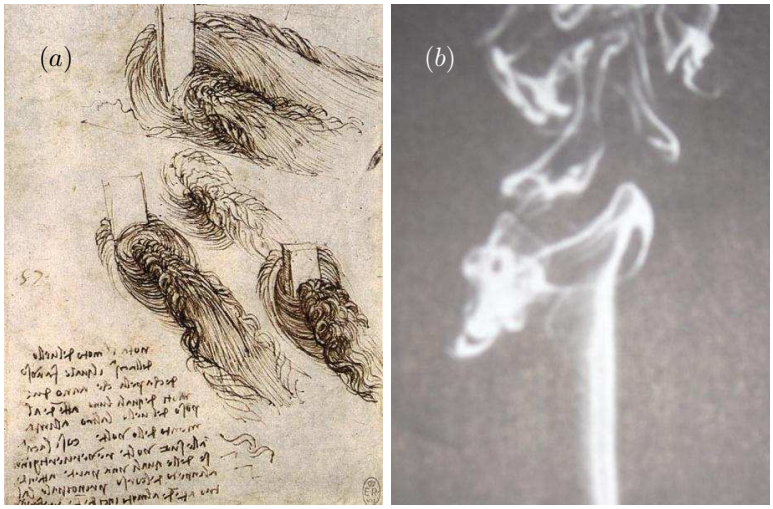

FIGURE 1.1. (*a*) Sketch from Leonardo da Vinci's notebooks. The picture is taken from Geurts (2003). (*b*) Meandering of smoke from a cigarette. The picture is taken from Libby (1996).

Dating back to early 16th century, the Italian genius Leonardo da Vinci sketched the famous "Old Man with Water Studies" (see Figure 1.1 (a)) and the following observations (Piomelli 2001) are made: "The water has eddying motions, one part of which is due to the principal current, the other to the random and reverse motion." These pure observations may be seen as a precursor to the Reynolds' decomposition which is a sophisticated way to study turbulence. The first example of a visualisation of a flow developing from laminar into turbulent motion is the famous experiment carried out by Osborne Reynolds in 1883. He studied the flow of water in a glass tube using ink as a dye. For low flow rates a steady dye stream was observed to follow a straight path through the tube. As the flow rate was increased, at some point, "the colour band would all at once mix up with the surrounding water, and fill the rest of the tube with a mass of coloured water", see e.g. Jackson & Launder (2007). In order to quantify these experimental results, he introduced a non-dimensional number $Re = \frac{UL}{\nu}$, now known as the Reynolds number, in his classic paper (Here U denotes the velocity scale, L the length scale and ν is the kinematic viscosity). Now it is known that the flow will become turbulent in practice, if the Reynolds number exceeds a value about 2000.

Another typical example demonstrating the nature of a turbulent flow is the meandering of the smoke from a cigarette (see Figure 1.1 (b)). The smoke first moves straight upward and suddenly changes to a turbulent status. This experiment not only provides the visualisation of the turbulent motion but also the spreading of a passive scalar in a turbulent flow. A passive scalar is a diffusive contaminant in a fluid flow that, due to its low concentration, has no influence on the fluid motion but is however influenced by the fluid motion. Typical passive scalars are e.g. small amounts of heat, salt in the sea or pollutants in atmospheric or oceanic flows. An understanding and prediction of the passive scalar behaviour in a turbulent flow is crucial since the turbulent momentum and scalar transport play a key role in many engineering applications and will be of growing importance in global environmental problems (Kasagi & Iida 1999).

When fluids flow above a solid body, the fluid elements in a thin layer near the body surface will be retarded due to the effect of friction while the other elements outside this thin layer are not affected. This thin layer is usually called boundary layer. The concept of the boundary layer was first proposed by Ludwig Prandtl in 1905. He hypothesised that the viscous effects are negligible everywhere except in the boundary layer. Furthermore, many interesting parameters of the aerodynamic property of a body, e.g. drag coefficient, are determined in precisely this boundary layer. Thus it is of great engineering significance in most applications to understand and (numerically or experimentally) fully resolve this thin layer of fluid.

Although the phenomena of turbulent flows vary from one to the other, the governing equations describing the motion of the Newtonian fluids are always the same. These equations are the so-called Navier-Stokes (NS) equations,

named after Claude-Louis Navier and George Gabriel Stokes who first formulated them in the 19th century. Together with the continuity equation (conservation of mass) and the scalar transport equation which governs the evolution of the scalar field, a system of equations consisting of five variables (three velocity components, pressure and scalar concentration) is established. However, the full equation system is non-linear and time dependent partial differential equations, and thus no analytical solutions exists except for the non-turbulent cases. Therefore, one has to calculate approximate solutions numerically with the aid of computers as an alternative to experiments.

Thanks to the rapid progress in high-performance computers, direct numerical simulation (DNS) and large-eddy simulation (LES) became important tools for turbulence research in the last couple of decades (Rogallo & Moin 1984; Moin & Mahesh 1998) whereas it is still dominated by the Reynolds-averaged Navier-Stokes (RANS) type of simulations in commercial codes. Additional reviews of the turbulent heat transfer and passive scalars are made by e.g. Kasagi & Iida (1999) and Warhaft (2000). DNS provides three-dimensional, time-dependent numerical solutions to the NS equations and the scalar transport equation. These equations are supposed to be solved as accurately as possible without employing any turbulence models, hence the errors come only from the numerical approximations and domain truncation. On the other hand, LES solves the equations with less grid points but supplemented with a so-called sub-grid scale (SGS) model to compensate for the omitted grid points. The overall performance of a LES calculation thus to a large extent depends on the chosen SGS model assuming sufficient grid points to resolve the relevant physics. RANS only gives averaged solutions to the Navier-Stokes equations with the so-called $k - \varepsilon$ model being most commonly used. One may refer to Pope (2000) for more detailed discussions about RANS models.

One important feature of turbulent flow is that it consists of temporal and spatial scales with a broad spectrum. The smallest scale arising in turbulent flows is usually the so-called Kolmogorov microscale η which is determined by the flow properties itself while the largest scales are commonly restricted by the flow geometry, e.g. the channel height or the boundary-layer thickness. A simple dimensional scaling argument leads to the conclusion that the resolution (number of grid points) of a DNS calculation required in each direction is proportional to $Re^{\frac{3}{4}}$ (Piomelli 2001; Jiménez 2003) and the exponent can increase up to 0.9 depending on the definitions of the Reynolds number (Reynolds 1989). The total computational time is then roughly proportional to Re^3 (Geurts 2003). This means a doubling of the Reynolds number would be feasible every 6 to 7 years if the rate of increase of the computer performance was maintained (Sandham 2002). Up to now, it seems that there is no signs of the computational capacity to slow down and especially recently there is a trend of using massively parallel processing (MPP) system, e.g. the Blue Gene systems, for large calculations.

For wall-bounded flows, the resolution requirement of a well-resolved LES calculation is that the number of grid points has to be sufficient to resolve the wall layer according to Piomelli (2001), i.e. to capture the energy-producing structures, e.g. the so-called streaks. The cost of the LES calculations also depends on the Reynolds number. As estimated by Chapman (1979), the resolution required to resolve the viscous sub-layer ($y^+ < 5$) is proportional to $Re^{1.8}$. The + denotes the wall scaling, i.e. scaled by $\frac{\nu}{u_\tau}$ where $u_\tau = \sqrt{\frac{\tau_w}{\rho}}$ is the friction velocity and τ_w the wall shear stress. Jiménez (2003) made a similar estimation that the resolution is proportional to Re_τ^2 where Re_τ is the Reynolds number based on the friction velocity u_τ. This means that using LES one can obtain results at higher Reynolds number than DNS for equivalent cost, but the Reynolds number reached is still not high enough for practical engineering flows. Recent studies have shown especially for wall-bounded turbulent flows, that a good LES is almost as expansive as a DNS, e.g. see the discussion in Fröhlich & Rodi (2002). Therefore, one has to resort to the wall models (Piomelli & Balaras 2002) or hybrid LES/RANS or detached eddy simulation (DES) (Spalart 2009) approach to perform calculations in an acceptable time for practical engineering applications. This in turn requires a good RANS model.

For the DNS of scalar transfer in turbulent flows, not only the Reynolds number but also the molecular Prandtl number (Pr) has to be considered. The molecular Prandtl number is a dimensionless number which is a measure of the ratio between viscous diffusion and scalar diffusion. Typical values for Pr are 0.71 for air, around 7 for water, between 100 and 40,000 for engine oil and around 0.025 for mercury (White 2006). For turbulent flows with scalar transport, the smallest scales in the scalar fluctuations decrease with the increase of Pr which makes the calculation even more expensive. The ratio of the largest to the smallest scales is approximately proportional to $Re^{\frac{3}{4}}Pr^{\frac{1}{2}}$ at very high Pr (Batchelor 1959; Tennekes & Lumley 1972).

In 1960s, the first LES calculations were performed by meteorologists (Smagorinsky 1963; Deardorff 1970) to predict atmospheric flows. A brief history of LES can be found in Lesier *et al.* (2005). The first DNS of turbulent flow starts with decaying isotropic turbulence using spectral methods, see the historical account by Canuto *et al.* (1988), on a 32^3 grid by Orszag & Patterson (1972). Later, Kim et al. (1987) simulated a fully developed channel flow using Fourier/Chebyshev algorithms at $Re_\tau = 180$ where Re_τ is the Reynolds number based on the friction velocity u_τ and the channel half width h. The first simulation of a fully turbulent boundary layer was performed by Spalart (1988) using an innovative spatio-temporal approach at $Re_\theta = 300, 670, 1410$ where the Reynolds number Re_θ is based on the free-stream velocity U_∞ and momentum thickness θ. The first DNS with passive scalars was performed by Rogers et al. (1986) in a homogeneous shear flow and by Kim and Moin (1989) in a channel flow of $Pr = 0.1$, 0.71 and 2.0 at $Re_\tau = 180$. DNS of turbulent

boundary layer were performed for the first time by Bell and Ferziger (1993) with $Pr = 0.1$, 0.71 and 2.0 up to a medium Reynolds number of $Re_\theta = 700$.

For canonical geometries, such as channel or flat-plate boundary layer, usually highly accurate and efficient algorithms, e.g. spectral methods (Canuto *et al.* 1988) which have barely no dissipation and dispersion errors, can be employed. However, spectral methods have difficulties in handling complex geometries. One way to overcome this drawback is to use the so-called spectral-element method first introduced by Patera (1984) and later developed by many others, see e.g. Maday & Patera (1989); Karniadakis & Sherwin (2005). The latter method combines the geometric generality/flexibility of the finite element method with the accuracy of spectral methods. However, the running cost, inefficient algorithms and stability issues have limited the applications of this method so far mainly to laminar and early transitional flows. Other possibilities are the use of the low-order schemes with extra grid points to compensate for the low accuracy. See more discussions in Sandham (2002).

One unique feature of numerical simulations is that they are able to simulate "wrong" physics as mentioned in Jiménez & Pinelli (1999), e.g. such as spurious modes, wrong thresholds, incorrect reattachment points, underestimated/overestimated functions due to under-resolved simulations, irrelevant size of the computational box, not appropriate boundary conditions or unrealistic parameters, etc. Thus, to generate simulation data with good quality is not simple or cheap at all. Therefore, the validation of the results becomes relatively important. Suggestions made in Sandham (2002) for DNS calculations are summarised here:

- validate the code against analytical solutions (if possible), asymptotic limits and well-established database;
- carry out systematic studies by varying the resolutions, box sizes, time steps and numerical methods.

For LES, Geurts (1999) interpreted it as a balancing between different sources of errors, i.e. modelling and numerical ones. This makes the validation of LES results even more complicated. In addition to the guidelines suggested for DNS, one should also follow the rules (Geurts & Leonard 2002)

- avoid dissipative numerical methods;
- vary the filter width while fixing the resolution;
- use dynamic modelling.

Moreover, to validate a given SGS model, one could conduct either *a priori* or *a posteriori* tests during which accurate data from either DNS or experiments are required. In *a priori* test, no actual simulations are carried out. The SGS model is evaluated based on the available DNS or experimental data and compared with the exact SGS stress. However, care has to be taken when interpreting the results since a successful *a priori* test does not guarantee good results in an actual LES calculation; sometimes the simulations can be even unstable (Vreman *et al.* 1995). On the other hand, a poor *a priori* test does not

necessarily lead to poor results in an actual run (Meneveau 1994). Therefore, to judge whether a SGS model performs well or not, one has to run a simulation with the correctly implemented model and then compare the results with DNS or experimental data. This approach is known as *a posteriori* test (Piomelli *et al.* 1988) in the LES community. To correctly compare the obtained LES results with DNS or experimental database, one should refer to e.g. Winckelmans *et al.* (2002); Sagaut (2005) for more detail.

CHAPTER 2

Theoretical formulation

2.1. Governing equations

2.1.1. *Direct numerical simulation (DNS)*

The governing equations for the direct numerical simulation (DNS) of an incompressible (laminar, transitional or turbulent) flow with passive scalars are the Navier-Stokes equations and the scalar transport equation, here written in non-dimensional form and tensor notation as

$$\begin{aligned} \frac{\partial u_i}{\partial t} + u_j \frac{\partial u_i}{\partial x_j} &= -\frac{\partial p}{\partial x_i} + \frac{1}{Re} \frac{\partial^2 u_i}{\partial x_j \partial x_j} \ , \\ \frac{\partial u_i}{\partial x_i} &= 0 \ , \\ \frac{\partial \theta}{\partial t} + u_i \frac{\partial \theta}{\partial x_i} &= \frac{1}{RePr} \frac{\partial^2 \theta}{\partial x_i \partial x_i} \ , \end{aligned} \tag{2.1}$$

where $(x_1, x_2, x_3) = (x, y, z)$ are the Cartesian coordinates in the streamwise, wall-normal and spanwise direction, respectively. $(u_1, u_2, u_3) = (u, v, w)$ are the corresponding instantaneous velocity fields, p is the pressure and θ the scalar concentration. The Reynolds number Re is defined as

$$Re = \frac{U_{\text{ref}} L_{\text{ref}}}{\nu} \ ,$$

where U_{ref}, L_{ref} and ν are the dimensional reference velocity and length and kinematic viscosity, respectively, which are also used for non-dimensionalisation. Pr is the Prandtl number defined by

$$Pr = \frac{\nu}{\alpha} \ ,$$

where α is the scalar diffusivity.

The summation convention is implied over repeated indices throughout this thesis unless stated otherwise. The streamwise and spanwise directions will be alternatively termed as the horizontal/wall-parallel directions.

2.1.2. *Large-eddy simulation (LES)*

The governing equations for large-eddy simulation (LES) are the spatially filtered Navier-Stokes equations and the scalar transport equation which in dimensionless form read

$$\begin{aligned} \frac{\partial \widetilde{u}_i}{\partial t} + \widetilde{u}_j \frac{\partial \widetilde{u}_i}{\partial x_j} &= -\frac{\partial \widetilde{p}}{\partial x_i} + \frac{1}{Re} \frac{\partial^2 \widetilde{u}_i}{\partial x_j \partial x_j} - \frac{\partial \tau_{ij}}{\partial x_j} \ , \\ \frac{\partial \widetilde{u}_i}{\partial x_i} &= 0 \ , \\ \frac{\partial \widetilde{\theta}}{\partial t} + \widetilde{u}_i \frac{\partial \widetilde{\theta}}{\partial x_i} &= \frac{1}{RePr} \frac{\partial^2 \widetilde{\theta}}{\partial x_i \partial x_i} - \frac{\partial \sigma_i}{\partial x_i} \ , \end{aligned} \tag{2.2}$$

where the so-called SGS stresses $\tau_{ij} = \widetilde{u_i u_j} - \widetilde{u}_i \widetilde{u}_j$ and $\sigma_i = \widetilde{u_i \theta} - \widetilde{u}_i \widetilde{\theta}$ represent the impact of the unresolved velocities/scalar on the resolved ones and have to be modelled. Mathematically, they arise from the nonlinearity of the convection term which does not commute with the linear filtering operation.

A filtered quantity $\widetilde{f}(x)$ in one dimension is defined by

$$\widetilde{f}(x) = G^P * f = \int_\Omega G^P(x, x', \Delta) f(x') \mathrm{d}x' \ ,$$

where Ω is the computational domain, G^P is the primary filter with Δ being the filter width. A three-dimensional filter can be easily formulated and the common filters are the sharp cut-off filter, Gaussian filter and top-hat filter. For more mathematical properties of these filters, one could refer to e.g. Pope (2000). The filtering operation separates the large and small scales and the filter function G^P determines the size and structures of the large scales. For the differentiation and the filtering operation to commute, G^P has to be a function of $x - x'$ only (Leonard 1974). A rough classification of the LES models can be made depending on the primary filter G^P: implicitly filtered models if the primary filter G^P is the grid filter, e.g. the ones used in the classical eddy-viscosity models; explicitly filtered models where an explicit filter operation is taken, e.g. the graded primary filter used in the approximate deconvolution model (ADM) (Stolz & Adams 1999).

2.2. Sub-grid scale modelling

In LES, the effects of the unresolved scales on the resolved ones have to be provided via the sub-grid scale (SGS) model. Therefore, a good SGS model is in generally desirable.

2.2.1. *Smagorinsky model (SM)*

The Smagorinsky model proposed first by Smagorinsky (1963) is the most widely used SGS model today. It belongs to the class of eddy-viscosity models since the traceless/deviatoric part of the SGS stresses τ_{ij} is modelled as

$$\tau_{ij} - \frac{\delta_{ij}}{3} \tau_{kk} = -2\nu_t \widetilde{S}_{ij} \ ,$$

where δ_{ij} is the Kronecker delta, defined by

$$\delta_{ij} = \begin{cases} 1 & \text{if } i = j \\ 0 & \text{if } i \neq j \end{cases} .$$

The strain rate of the resolved velocity field $\widetilde{S}_{ij}$ is calculated according to

$$\widetilde{S}_{ij} = \frac{1}{2}\left(\frac{\partial \widetilde{u}_i}{\partial x_j} + \frac{\partial \widetilde{u}_j}{\partial x_i}\right) .$$

The eddy viscosity ν_t is obtained by

$$\nu_t = (C_s\Delta)^2|\widetilde{S}| ,$$

where $|\widetilde{S}|$ is defined by

$$|\widetilde{S}| = \sqrt{2\widetilde{S}_{ij}\widetilde{S}_{ij}} .$$

Δ is a typical length scale of the primary filter usually computed from the grid size as $\Delta = (\Delta x \Delta y \Delta z)^{\frac{1}{3}}$ (Deardorff 1970). The model coefficient C_s known as the Smagorinsky constant is actually not a constant and has to be determined *a priori* based on the flow case. Lilly (1967) derived an approximate value for the Smagorinsky constant $C_s \approx 0.18$ in homogeneous isotropic turbulence. However, this value is found to cause excessive damping in wall-bounded flows and has to be reduced to $C_s \approx 0.1$ to sustain turbulence as reported by Deardorff (1970); Moin & Kim (1982); Piomelli *et al.* (1988). McMillan *et al.* (1980) confirmed in *a priori* tests that in homogeneous turbulence C_s does decrease with increasing strain rate.

Despite that SM with constant coefficient is successful in certain flow types, it suffers from a number of drawbacks. One major drawback is that the sub-grid scale stress does not vanish close to solid walls. One remedy is to use the so-called van Driest wall damping function (van Driest 1956). Other drawbacks are that e.g. the model does not predict the correct growth rate of the initial disturbances due to excessive damping and it does not account for the so-called "backscatter", i.e. energy transfer from unresolved scales to resolved scales, which in certain circumstances can be significant (Piomelli *et al.* 1991; Härtel *et al.* 1994). The capability of accounting for backscatter is usually considered as a merit of a LES model.

2.2.2. *High-pass filtered Smagorinsky model (HPF-SM)*

Alternatively, high-pass filtered (HFP) velocities can be used instead of the low-pass filtered ones to calculate the SGS model contribution. Ducros *et al.* (1996) showed that the filtered structure function (FSF) model based on the structure function (SF) model proposed by Métais & Lesieur (1992) was able to predict transitional flow. Later, Sagaut *et al.* (2000) employed a high-pass filtered velocity to calculate the eddy viscosity. Not only the eddy viscosity, but also the strain rate could be calculated based on high-pass filtered quantities. These models were first proposed by Vreman (2003) and Stolz *et al.* (2005) based on SM closure. With the high-pass filtered velocities $H * \widetilde{u}$ where H is a

high-pass filter, the computation of the SGS stress τ_{ij}, the strain rate $S_{ij}(H*\widetilde{u})$ and the eddy viscosity ν_t^{HPF} become

$$\begin{aligned}
\tau_{ij} - \frac{\delta_{ij}}{3}\tau_{kk} &= -2\nu_t^{HPF} S_{ij}(H*\widetilde{u}) \ , \\
S_{ij}(H*\widetilde{u}) &= \frac{1}{2}\left(\frac{\partial H*\widetilde{u}_i}{\partial x_j} + \frac{\partial H*\widetilde{u}_j}{\partial x_i}\right) \ , \\
\nu_t^{HPF} &= (C_s^{HPF}\Delta)^2 |S(H*\widetilde{u})| \ , \\
|S(H*\widetilde{u})| &= \sqrt{2S_{ij}(H*\widetilde{u})S_{ij}(H*\widetilde{u})} \ .
\end{aligned}$$

There is a close relation between the HPF models and the variational multiscale (VMS) method presented by Hughes *et al.* (2000, 2001). The two methods differ in how the scale separation is treated. In the HPF methodology, the filtering approach is adopted while in the VMS method, the scale separation is performed by projection onto disjunct functional spaces.

One advantage of the HPF-SM is that the model contribution vanishes on solid boundaries so that no near-wall damping is needed. Moreover, the ability to handle transitional flows is shown in Stolz *et al.* (2005) and it accounts for backscatter (Schlatter *et al.* 2005). However, the model constant C_s^{HPF} does not have the correct asymptotic behaviour which gives rise to restricted time steps (Jeanmart & Winckelmans 2007). Therefore, more general remedies other than the ad-hoc near-wall damping have been proposed. This leads to the introduction of the wall-adapting local eddy viscosity (WALE) model (Nicoud & Ducros 1999) and the dynamic procedure (Germano *et al.* 1991; Lilly 1992).

Using the square of the velocity tensor, the WALE model evaluates the viscosity in such a way that it has the proper near-wall behaviour. However, the more widely used method is the dynamic procedure first proposed by Germano *et al.* (1991) and later refined by Lilly (1992). The idea is to use the local flow information to calculate the model coefficient rather than determine it *a priori*. Here SM will be used as an example to show the formulation of the dynamic procedure.

Filtering the LES equations (2.2) by a second filter, the so-called test filter, denoted by $\widehat{\ }$, one obtains

$$\frac{\partial \widehat{\widetilde{u}}_i}{\partial t} + \frac{\partial \widehat{\widetilde{u}}_i \widehat{\widetilde{u}}_j}{\partial x_j} = -\frac{\partial \widehat{\widetilde{p}}}{\partial x_i} + \frac{1}{Re}\frac{\partial^2 \widehat{\widetilde{u}}_i}{\partial x_j \partial x_j} - \frac{\partial T_{ij}}{\partial x_j} \ , \tag{2.3}$$

where $T_{ij} = \widehat{\widetilde{u}_i \widetilde{u}_j} - \widehat{\widetilde{u}}_i \widehat{\widetilde{u}}_j$ is the SGS stress at the test filter level. The test filter is usually chosen to be a sharp cut-off filter applied only in wall-parallel planes leaving the wall-normal direction unfiltered. Although not fully justified, this two-dimensional filtering approach is widely used in LES community. The test filter width is usually set to $\widehat{\Delta} = 2\Delta$. Different widths have been tested in channel flow simulations but no noticeable difference has been reported (Germano *et al.* 1991). By simple mathematical manipulations of equations (2.2) and (2.3), the so-called Germano identity (Germano *et al.* 1991; Germano 1992)

is recovered

$$L_{ij} = \widehat{\tau}_{ij} - T_{ij} \tag{2.4}$$

where $L_{ij} = \widehat{\widetilde{u}_i}\widehat{\widetilde{u}}_j - \widehat{\widetilde{u}_i\widetilde{u}_j}$ is the so-called resolved turbulent stress (Germano *et al.* 1991; Lilly 1992). Applying the Smagorinsky closure to both τ_{ij} and T_{ij}, one obtains

$$\tau_{ij} - \frac{\delta_{ij}}{3}\tau_{kk} = -2(C_s\Delta)^2|\widetilde{S}|\widetilde{S}_{ij} \ ,$$

$$T_{ij} - \frac{\delta_{ij}}{3}T_{kk} = -2(C_s\widehat{\Delta})^2|\widehat{\widetilde{S}}|\widehat{\widetilde{S}}_{ij} \ .$$

Inserting into the Germano identity (2.4) yields

$$L_{ij} - \frac{\delta_{ij}}{3}L_{kk} = 2(C_s\widehat{\Delta})^2|\widehat{\widetilde{S}}|\widehat{\widetilde{S}}_{ij} - 2(C_s\Delta)^2\widehat{|\widetilde{S}|\widetilde{S}_{ij}} = 2C_{dyn}M_{ij} \tag{2.5}$$

where $M_{ij} = \widehat{\Delta}^2|\widehat{\widetilde{S}}|\widehat{\widetilde{S}}_{ij} - \Delta^2\widehat{|\widetilde{S}|\widetilde{S}_{ij}}$ is used as an abbreviation and C_s^2 is replaced by C_{dyn}. In Germano *et al.* (1991), equations (2.5) were contracted with the resolved strain rate $\widetilde{S}_{ij}$ to determine C_{dyn} without physical justification. Note that C_{dyn} solved in this way can become negative and this will account for the backscatter. Lilly (1992) suggested a least-squares approach to minimise the residual $Q = (L_{ij} - \frac{\delta_{ij}}{3}L_{kk} - 2C_{dyn}M_{ij})^2$ and this leads to

$$C_{dyn} = \frac{1}{2}\frac{M_{ij}L_{ij}}{M_{lm}M_{lm}} \ .$$

In practise, averaging in homogeneous direction is usually applied to smoothen C_{dyn} which is considerably fluctuating otherwise. However, this will limit the dynamic model to flows with at least one homogeneous direction.

The dynamic model formulation for the HPF-SM follows the same recipe and will not be repeated here. One may refer to Bruhn (2006); Schlatter *et al.* (2006*a*) for more details.

2.2.3. *Inverse model*

It was realised some time ago that, to some extent, an accurate approximation of a sub-grid scale quantity can be reconstructed from the resolved quantities. The first model based on this idea is introduced by Leonard (1974). Later, the so-called tensor-diffusivity model (TDM) was proposed where the filtered non-linear term is expressed in filtered quantities using Taylor expansions (Leonard & Winckelmans 1999; Winckelmans *et al.* 2001). The SGS stress τ_{ij} with uniform filter width Δ then reads

$$\tau_{ij} = \Delta^2\frac{\partial\widetilde{u}_i}{\partial x_k}\frac{\partial\widetilde{u}_j}{\partial x_k} + \frac{\Delta^4}{2!}\frac{\partial^2\widetilde{u}_i}{\partial x_k\partial x_l}\frac{\partial^2\widetilde{u}_j}{\partial x_k\partial x_l} + \frac{\Delta^6}{3!}\frac{\partial^3\widetilde{u}_i}{\partial x_k\partial x_l\partial x_m}\frac{\partial^3\widetilde{u}_j}{\partial x_k\partial x_l\partial x_m} + \cdots \ ,$$

where summation is assumed over triply repeated indices. For more general filters, one could refer to e.g. Carati *et al.* (2001). If the expansion is truncated after the second-order term, one recovers the so-called gradient model (Clark

et al. 1979). However, these SGS models tend to provide not enough dissipation, therefore, a Smagorinksy eddy-viscosity term is usually supplemented as a regularisation.

Another approach sharing the same idea is the so-called approximate deconvolution model (ADM) which was proposed by Stolz & Adams (1999) for both incompressible and compressible flows (Stolz *et al.* 2001*a*,*b*; Stolz & Adams 2003). Following the notation used in Stolz *et al.* (2001*a*), the approximation of the unfiltered velocity u_i is denoted by $u_i^\star$ and the SGS stress is modelled by

$$\tau_{ij} = \widetilde{u_i^\star u_j^\star} - \widetilde{u}_i \widetilde{u}_j \ ,$$

where the approximately deconvolved quantities $u_i^\star$ is defined by

$$u_i^\star = Q_N * \widetilde{u}_i \tag{2.6}$$

with

$$Q_N = \sum_{\nu=1}^{N} (I - G)^\nu \approx G^{-1} \ , \tag{2.7}$$

where I is the identity operator, G the primary filter and Q_N the approximate inverse of G. N is usually set to 5 and results obtained by using $N > 5$ do not give significant improvements (Stolz *et al.* 2001*a*). Combining equations (2.6) and (2.7), $u_i^\star$ can be approximated by

$$u_i^\star = Q_N * \widetilde{u}_i = 3\widetilde{u}_i - 3\widetilde{\widetilde{u}}_i + \widetilde{\widetilde{\widetilde{u}}}_i + \cdots \ .$$

For high level deconvolution, the van Cittert iterative method used in the ADM is more efficient than evaluating the higher-order terms in the direct reconstruction series as in the TDM (Winckelmans *et al.* 2001). Furthermore, a relaxation regularisation is also needed for ADM which models the interaction of the resolved scales and those not represented on the numerical grid.

Schlatter *et al.* (2006,*b*) showed that for simulations using spectral methods the deconvolution operation applied in the ADM approach is usually not necessary. This leads to a promising and simple LES model, i.e. the relaxation-term (RT) model. In this model, the 3D primary filter only applies to the relaxation term while the non-linear terms are directly computed from the resolved quantities. The SGS forcing then simply reads

$$\frac{\partial \tau_{ij}}{\partial x_j} = \chi (I - Q_N * G) * \widetilde{u}_i = \chi (I - G)^{N+1} * \widetilde{u}_i = \chi H_N * \widetilde{u}_i$$

where $H_N = (I - G)^{N+1}$ is a high-pass filter and χ is the model constant. The constant χ can be determined dynamically, however, tests showed that the results are rather insensitive to it (Stolz *et al.* 2001*a*; Schlatter *et al.* 2006).

The RT model has been shown to obtain accurate results in transitional and turbulent incompressible wall-bounded flows (Schlatter *et al.* 2004, 2006, 2009*a*) and is related to the spectral vanishing viscosity approach by Karamanos & Karniadakis (2000). Since $(I - Q_N * G)$ is positive semidefinite (Stolz *et al.* 2001*a*), the relaxation term is always dissipative and only the small scales

are affected while the large ones are not directly influenced by the model contributions.

2.2.4. *Eddy-diffusivity model*

The sub-grid scale (SGS) model for the passive scalar corresponding to eddy-viscosity models is the so-called eddy-diffusivity model. The SGS stress σ_i is obtained by

$$\sigma_i = -\frac{\nu_t}{Pr_t}\frac{\partial\widetilde{\theta}}{\partial x_i}$$

or

$$\sigma_i = -\frac{\nu_t^{HPF}}{Pr_t}\frac{\partial H*\widetilde{\theta}}{\partial x_i}$$

for classic or high-pass filtered eddy-viscosity models and

$$\sigma_i = -\frac{\chi}{Pr_t}\frac{\partial H_N*\widetilde{\theta}}{\partial x_i}$$

for RT model. A constant turbulent Prandtl number $Pr_t = 0.6$ is usually assumed. Note that all the drawbacks of the models for the velocity are present in the scalar models as well. It should be noted that the literature on SGS modelling of passive scalars is much less extensive than that for the velocities. In particular high Péclet numbers (high Re or Pr) are seldomly addressed.

2.3. Inner and outer scaling of wall turbulence

In many applications, it is the mean flow rather than the rapid fluctuations that is interesting and important. Naturally the Reynolds decomposition of the flow field variables into a mean and a fluctuating quantity is introduced by

$$u_i = \langle u_i\rangle + u_i' \ ,$$
$$p = \langle p\rangle + p' \ ,$$
$$\theta = \langle\theta\rangle + \theta' \ ,$$

where the angular brackets denote a suitably defined mean and a prime denotes the fluctuating part. In a statistically stationary turbulent flow, the mean value of a flow quantity can be taken as the time average or as an average in the homogeneous directions. Generally the mean of a quantity is the ensemble average over an infinite number of realisations. In the present case the mean of a quantity $f(x,y,z,t)$ is defined by

$$\langle f\rangle(x,y) = \lim_{T\to\infty}\frac{1}{T}\int_0^T f(x,y,z,t)\mathrm{d}t \ ,$$

where the spanwise (z) dependence disappears since it is a homogeneous direction.

The behaviour of the flow in the near wall region is of great importance and it was first treated by Ludwig Prandtl. A usual measure of the boundary-layer thickness is δ_{99} which is defined as the wall-normal position at which

the mean streamwise velocity $\langle u \rangle$ reaches the 99% of the free-stream velocity U_∞. However, this is a poorly conditioned quantity both experimentally and numerically, since it depends on the measurement of a small velocity difference (Pope 2000). Therefore, other measures have been proposed based on integral quantities such as the displacement thickness

$$\delta^* = \int_0^\infty \left(1 - \frac{\langle u \rangle}{U_\infty}\right) \mathrm{d}y \ ,$$

and the momentum thickness

$$\theta = \int_0^\infty \frac{\langle u \rangle}{U_\infty} \left(1 - \frac{\langle u \rangle}{U_\infty}\right) \mathrm{d}y \ .$$

The Rotta-Clauser length is also often used and defined by

$$\Delta = \frac{U_\infty \delta^*}{u_\tau} \ .$$

Another quantity known as the shape factor H_{12} which indicates the "fullness" of the mean velocity profile can be defined based on δ^* and θ as

$$H_{12} = \frac{\delta^*}{\theta} \ .$$

For the laminar Blasius boundary layer profile the shape factor $H_{12} = 2.59$ and decreases with increasing Re with an asymptotic value being unity (Nagib et al. 2007).

In the vicinity of the wall, i.e. $y/\delta_{99} \ll 1$, one can show that the total shear stress τ is nearly constant and the viscous effects are important, see e.g. Pope (2000). This is true for all canonical wall-bounded flows, i.e. channel, pipe and turbulent boundary-layer flows. Therefore, the so-called friction velocity u_τ and viscous length scale l_* are chosen to be the velocity and length scales and defined as

$$u_\tau \equiv \sqrt{\frac{\tau_w}{\rho}} = \sqrt{\nu \frac{\partial \langle u \rangle}{\partial y}\Big|_{y=0}} \quad \text{and} \quad l_* = \frac{\nu}{u_\tau} \ ,$$

where ρ is the density.

Using the viscous scalings derived above, the mean streamwise velocity very close to the wall can be written in the form

$$u^+ = \frac{\langle u \rangle}{u_\tau} = \Phi(\frac{y}{l_*}) = \Phi_1(y^+) \ , \tag{2.8}$$

where the "+" denotes normalisation in viscous (wall) units and equation (2.8) is referred to as the law of the wall. Far away from the wall, say $y \sim \delta_{99}$, the viscous effects are not crucial, in contrast, the dynamics are dominated by the turbulence. In this outer region, the so-called velocity-defect law describes the mean streamwise velocity distribution and reads

$$\frac{\langle u \rangle - U_\infty}{u_\tau} = \Psi(\frac{y}{\Delta^*}) = \Psi_1(\eta) \ ,$$

where Δ^* is the outer length scale.

Following the argument by Millikan (1938), a so-called overlap region, i.e. $l_* \ll y \ll \Delta^*$, exists and within which the derivatives of the law of the wall and of the velocity-defect law should asymptoticly match. This yields

$$y^+ \frac{\mathrm{d}\Phi(y^+)}{\mathrm{d}y^+} = \eta \frac{\mathrm{d}\Psi(\eta)}{\mathrm{d}\eta} = \frac{1}{\kappa} \ .$$

This equation can be satisfied only when both sides are constant, which leads to the introduction of the von Kármán constant κ. Integrating the equation one obtains logarithmic velocity profiles

$$\Phi_1(y^+) = \frac{\langle u \rangle}{u_\tau} = \frac{1}{\kappa} \ln(y^+) + A \ ,$$

$$\Psi_1(\eta) = \frac{\langle u \rangle - U_\infty}{u_\tau} = \frac{1}{\kappa} \ln(\eta) + B \ ,$$

where A and B are the integration constants.

The von Kármán constant κ and integration constants are generally considered to be universal, i.e. independent of Reynolds number and flow geometries. However, there is no generally agreed values for these constants since these constants are different from one experiment/simulation to the other, see e.g. Nagib & Chauhan (2008). Except for the log-law, there are other proposed scalings for the overlap region, e.g. a power-law description. For more discussion about power law, one may refer to George & Castillo (1997) and the references therein.

Similarly, one can also derive the law of the wall, the defect law and the log-law for the scalar field. The resulting equations read

$$\theta^+ = \frac{\theta_w - \langle \theta \rangle}{\theta_\tau} = \Phi_\theta(y^+, Pr) \ ,$$

$$\frac{\langle \theta \rangle - \theta_\infty}{\theta_\tau} = \Psi_\theta(\eta, Pr) \ ,$$

$$\Phi_\theta(y^+, Pr) = \frac{\theta_w - \langle \theta \rangle}{\theta_\tau} = \frac{1}{\kappa_\theta} \ln(y^+) + A_\theta(Pr) \ ,$$

$$\Psi_\theta(\eta, Pr) = \frac{\theta_\infty - \langle \theta \rangle}{\theta_\tau} = \frac{1}{\kappa_\theta} \ln(\eta) + B_\theta(Pr) \ ,$$

where κ_θ is the von Kármán constant for the scalar field with A_θ and B_θ being functions of Pr. θ_w and θ_∞ are the scalar concentration at the wall and in the free stream, respectively. The friction scalar θ_τ is analogous to the friction velocity u_τ and defined by

$$\theta_\tau = \frac{q_w}{\rho c_p u_\tau} \ ,$$

where ρ is the density of the fluid, c_p is the scalar capacity of the fluid, u_τ is the friction velocity and q_w is the rate of the scalar transfer from the wall to the flow which is defined by Fick's first law $q_w = -k \frac{\partial \langle \theta \rangle}{\partial y}\Big|_{y=0}$, where k is the scalar conductivity.

CHAPTER 3

Turbulent boundary layer

3.1. Mean statistics

Figure 3.1 depicts the mean velocity profiles at four different Reynolds numbers ranging from $Re_\theta = 671$ to $Re_\theta = 2512$ obtained from DNS. As the Reynolds number increases, the logarithmic region becomes much more extended and clearer. The data at $Re_\theta = 1410$ obtained by Spalart (1988) differs from the one by Schlatter et al. (2009), probably due to a suspected lower actual Re_θ in the former simulation. The excellent agreement between the simulation data and the experimental one indicates that the mean statistics are insensitive to the numerical and experimental setup. The root-mean-square (RMS) values of the scalar fluctuation are shown in Figure 3.2. With increasing Pr, the RMS values increase and the peak positions move towards the wall. Due to isoflux wall boundary condition, the RMS values remain constant near the wall while the ones with isoscalar wall boundary condition decrease to zero.

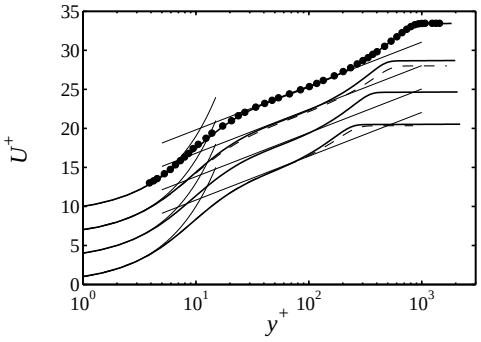

FIGURE 3.1. Mean streamwise velocity profiles U at $Re_\theta = 671, 1000, 1412, 2512$. ——DNS by Schlatter et al. (2009), • experimental data by Schlatter et al. (2009), - - -DNS by Spalart (1988). The thin lines indicate the linear and logarithmic laws, using $\frac{1}{\kappa}\ln y^+ + 5.2$ with $\kappa = 0.41$. A detailed discussion of the figure is found in Paper 2.

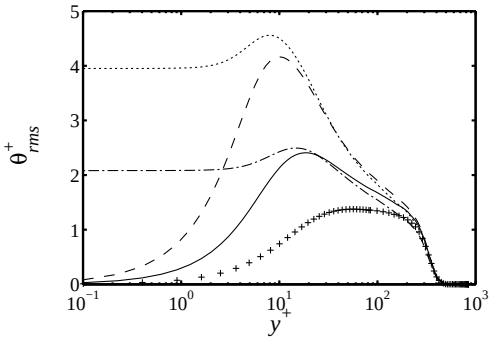

FIGURE 3.2. Profiles of the RMS values of the scalar fluctuation θ_{rms} at $Re_\theta = 830$. + θ_1 with $Pr = 0.2$, ——θ_2 with $Pr = 0.71$, –·–θ_3 with $Pr = 0.71$, – – –θ_4 with $Pr = 2.0$, ····· θ_5 with $Pr = 2.0$. Isoscalar wall: θ_1, θ_2 and θ_4. Isoflux wall: θ_3 and θ_5. A detailed discussion of the figure is found in Paper 4.

3.2. Coherent structures

Even though wall-bounded turbulence is characterised by chaotic and random motions, there are actually recurrent and well-organised features, i.e. coherent structures and motions present in the flow. Taking the definition used in Robinson (1991), a coherent structure or motion is defined as "a three-dimensional region of the flow over which at least one fundamental flow variable (velocity component, density, temperature, etc.) exhibits significant correlation with itself or with another variable over a range of space and/or time that is significantly larger than the smallest local scales of the flow."

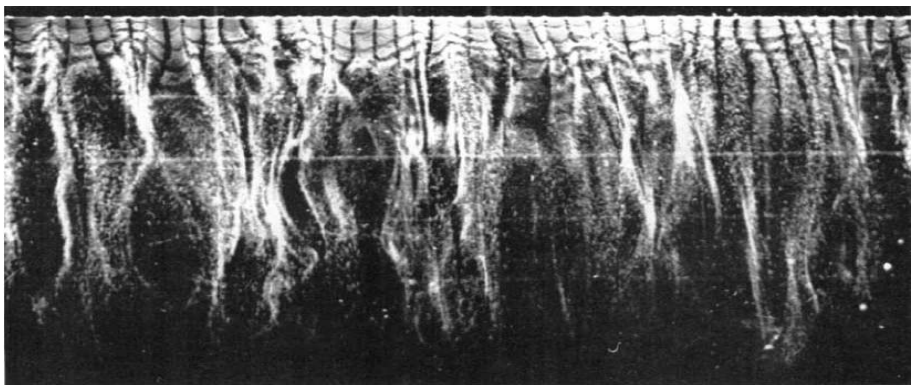

FIGURE 3.3. Photograph of the structure of a flat-plate turbulent boundary layer at $y^+ \approx 2.7$. The picture is taken from Kline *et al.* (1967).

The most widely studied structure in wall-bounded flow is the so-called near-wall streaks which are alternating high- (positive fluctuation) and low-speed (negative fluctuation) regions elongated in the streamwise direction. Figure 3.3 shows such streaky structures near the wall in a water channel taken from Kline *et al.* (1967) using tiny hydrogen bubbles released periodically from a thin platinum wire on the top. These streaky structures have a spanwise spacing of about $\Delta z^+ \approx 100$, and a streamwise spacing $\Delta x^+ > 1000$ (Smith & Metzler 1983). However, recent simulations (Li *et al.* 2009; Schlatter et al. 2009) and experiments (Lin *et al.* 2008) reported a value around 120 for the spanwise spacing of the streaks. These structures are relatively quiescent most of the time. However, the low-speed fluid near the wall occasionally erupts violently into the outer region of the boundary layer (ejection motion). Kline *et al.* (1967) and Kim *et al.* (1971) were among the first to name this process as "bursting" which was later used by Wallace *et al.* (1972), Willmarth & Lu (1972) and Lu & Willmarth (1973) among others. During a bursting process, as described by Kim *et al.* (1971), the low-speed streaks were observed first to lift up slowly away from the wall, then start a growing oscillation and finally break up into more chaotic motion. Intermittently, the high-speed fluid also rushes in toward the wall at a shallow angle (sweep motion). Together with the ejection motion, these two events contribute to most of the production of the turbulence and are considered to be a self-sustained and quasi-cyclic sequence (Robinson 1991). Jiménez & Pinelli (1999) showed that both the formation of streaks and the generation of vortices from the instability of streaks are important to maintain the turbulence.

Besides the near-wall streaks, there are also structures existing in the outer region of the boundary layer (Kim & Adrian 1999; del Álamo and Jiménez 2003; Abe *et al.* 2004; Hutchins & Marusic 2007; Schlatter et al. 2009). These

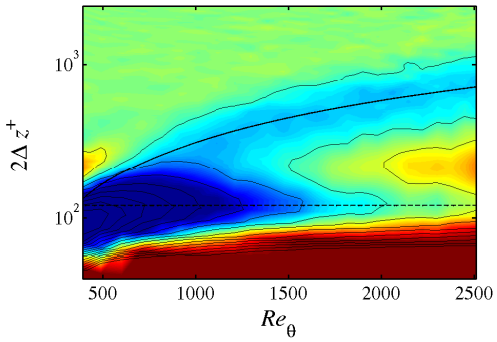

FIGURE 3.4. Spanwise two-point correlation $R_{\tau\tau}$ of the wall-shear stress τ_w. ——— corresponds to $0.85\delta_{99}$, - - - corresponds to $2\Delta z^+ = 120$. A detailed discussion of the figure is found in Paper 2.

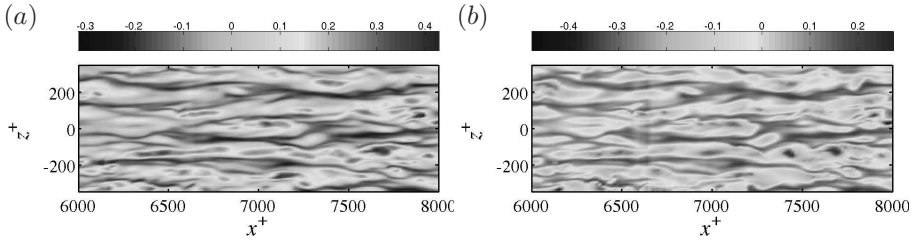

FIGURE 3.5. Instantaneous streamwise velocity and scalar fields at $y^+ \approx 7$. (a) u', (b) θ' with $Pr = 0.71$. A detailed discussion of the figure is found in Paper 4.

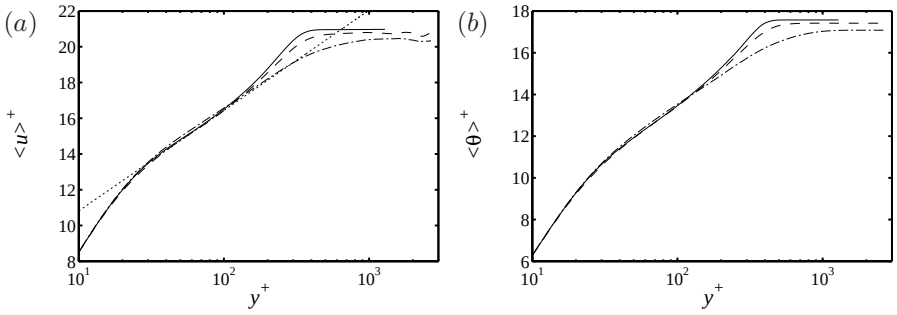

FIGURE 3.6. Mean velocity and temperature fields with FST at $Re_\theta \approx 850$. (a) $\langle u \rangle$, (b) $\langle \theta \rangle$ with $Pr = 0.71$. ——no FST, – – –$Tu = 4.7\%$ at the inlet, —·—$Tu = 40\%$ at the inlet, ····· log-law. A detailed discussion of the figure is found in Paper 5.

structures relate to the "inactive" motion by Townsend (1976) and usually scale with outer units, e.g. the channel height h or the boundary-layer thickness δ_{99}. Even though the near-wall cycle seems to be self-sustained, it is believed that the outer structures have at least a modulating influence on the near-wall events (Robinson 1991). This has been observed both in simulation and experiments, see e.g. Hutchins & Marusic (2007*b*); Schlatter et al. (2009). One such example is shown in Figure 3.4 where the spanwise two-point correlation of the wall-shear stress τ_w is shown as a function of Reynolds number. Except for the near-wall peak at $2\Delta z^+ \approx 120$ (dash line) showing the existence of the streaks, a second peak (solid line) is clearly visible for $Re_\theta > 1500$ which indicates the footprints of the large-scale structure onto the fluctuating wall-shear stress.

Kim and Moin (1989) reported that the correlation coefficient between the streamwise velocity and the scalar ($Pr = 0.71$) is as high as 0.95 in the near-wall region. Therefore, it is expected that the mean spanwise spacing of the scalar/thermal streaks is about 100 in wall units as well. Furthermore, it is also

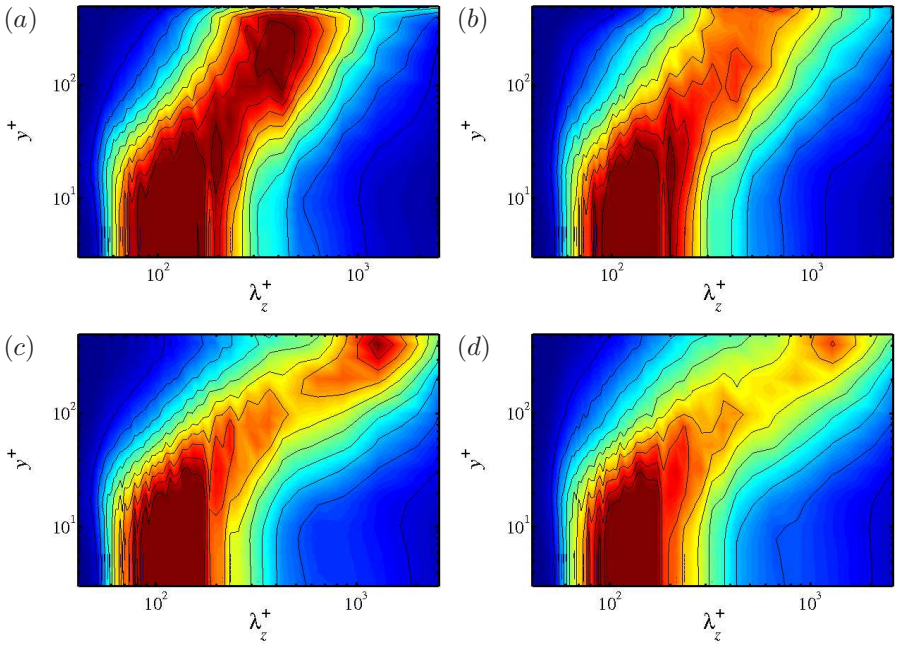

FIGURE 3.7. Premultiplied spanwise energy spectra of $\Phi_{uu}(\lambda_z)/u^2_{rms}$ and $\Phi_{\theta\theta}(\lambda_z)/\theta^2_{rms}$ with $Pr = 0.71$ at $Re_\theta \approx 900$. (a) $\Phi_{uu}(\lambda_z)/u^2_{rms}$ with no FST at inlet, (b) $\Phi_{\theta\theta}(\lambda_z)/\theta^2_{rms}$ with no FST at inlet, (c) $\Phi_{uu}(\lambda_z)/u^2_{rms}$ with $Tu = 40\%$ at inlet, (d) $\Phi_{\theta\theta}(\lambda_z)/\theta^2_{rms}$ with $Tu = 40\%$ at inlet.

confirmed that the low-speed fluids are associated with low scalar concentration regions and high-speed fluids with high scalar concentration regions (Iritani *et al.* 1985; Kong et al. 2000; Li *et al.* 2009). A visualisation of near-wall velocity and scalar streaks is shown in Figure 3.5. However, when there are disturbances present in the free stream, differences start to appear. Previous experimental work by Simonich & Bradshaw (1978); Blair (1983*a*,*b*) found that the heat transfer on the wall grows with increasing turbulence intensity in the free stream. This is very crucial for the industry application since it has direct influences on the cooling design and the hardware durability. Moreover, the wake region of the mean velocity and temperature profiles is depressed due to a high free-stream turbulence (FST) as also shown in Figure 3.6.

For the large-scale structures of the scalar without FST, Abe and Kawamura (2002) reported the existence of such structures in channel flow for $Re_\tau = 640$ with $Pr = 0.025$ and 0.71, but no detailed discussion was provided. Li *et al.* (2009) also observed the large-scale structure in the outer region of the boundary layer at $Re_\theta = 830$. But at such a relatively low Reynolds number, the outer peak in the energy spectra is not obvious due to insufficient scale

separation. With FST present, the spanwise scale of the outer structures grows from $\mathcal{O}(\delta_{99})$ to $3 \sim 4\mathcal{O}(\delta_{99})$, see Figure 3.7. It is speculated that it is these large structures which cause the increase of the heat transfer from the wall.

CHAPTER 4

Numerical method

The results presented in this thesis are obtained using the simulation code **SIMSON** (Chevalier *et al.* 2007) developed at KTH Mechanics over many years. The governing equations are discretised based on a standard spectral method (Canuto *et al.* 1988). The discretisation in the horizontal directions uses Fourier expansions assuming periodic solutions. In the wall-normal direction, Chebyshev polynomials with the Chebyshev tau method (CTM) (Canuto *et al.* 1988) are used to discretise the solution and the boundary condition. The time advancement used is a third-order Runge-Kutta method for the non-linear terms and a second-order Crank-Nicolson method for the linear terms. Adaptive time stepping is adopted to exploit the maximum stable time step. The non-linear terms are calculated in physical space rather than spectral space (pseudo-spectral method). Aliasing errors from the evaluation of the non-linear terms are removed by the 3/2-rule (Canuto *et al.* 1988) when the horizontal FFTs are performed.

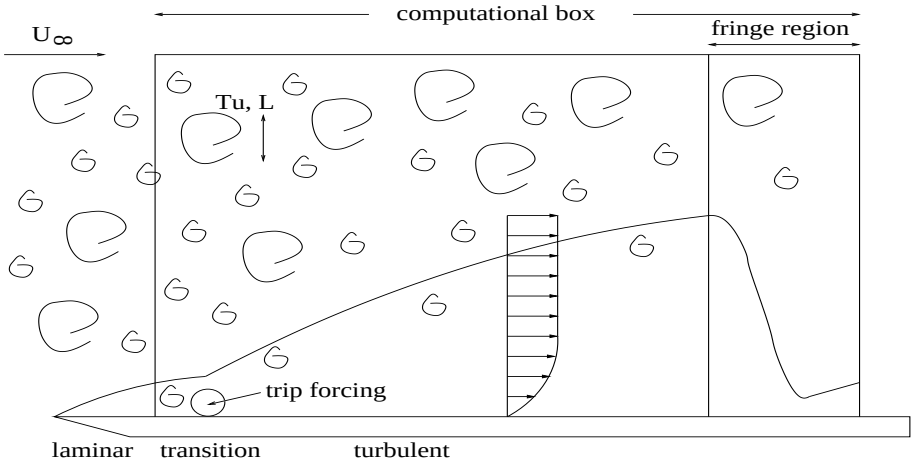

FIGURE 4.1. Sketch of the computational domain with free-stream turbulence.

A sketch of the computational box is shown in Figure 4.1. The periodicity in the wall parallel directions is fulfilled by adding a so-called "fringe region" (Bertolotti et al. 1992; Nordström et al. 1999) at the downstream end of the

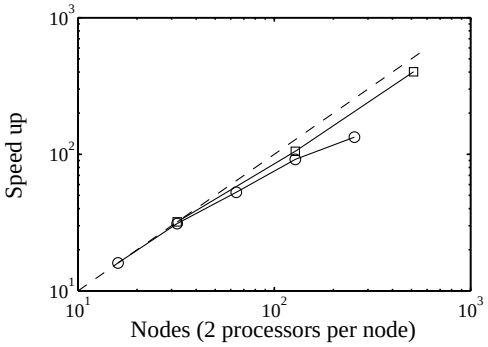

FIGURE 4.2. Speedup curve for the benchmark case. ◯ 1D parallelisation, □ 2D parallelisation, – – –linear speedup.

domain. In this region, the outflow is forced by a prescribed volume force to the laminar Blasius inflow. In addition, to trigger rapid (natural) laminar-turbulent transition, a random volume forcing directed normal to the wall is located at a short distance downstream of the inlet. The turbulent field generated by the trip force leads to very good quality at the expense of a slightly enlarged transitional inflow region. In particular, there are no streamwise correlations in the fluctuations as opposed to e.g. the rescaling and recycling method proposed by Lund *et al.* (1998).

SIMSON is also capable of simulating free-stream turbulence (FST). As described in Grosch & Salwen (1978), the continuous eigenmodes of the Orr-Sommerfeld/Squire operator provide a basis for the FST. Therefore, the generation of the FST is by a superposition of eigenmodes of the Orr-Sommerfeld/Squire operator with prescribed energy spectrum, i.e. the von Kármán spectrum. For more details about the generation of FST, one could refer to Brandt *et al.* (2004); Schlatter (2001); Jacobs & Durbin (2000). The FST is homogeneous and isotropic, and satisfies the continuity constraint as well.

The numerical code is written in FORTRAN 77/90 and consists of two major parts: one linear part where the equations are solved in spectral space, and one non-linear part where the non-linear terms are computed in physical space. The main computational effort in these two parts is in the FFT which consumes more than 55% of the total execution time. Thanks to the parallelisation, the expensive computation of the FFTs is not the main problem; the communication between processors being the bottle neck. The present code has been highly parallelised either using OpenMP (Multi Processing) on shared memory machines or MPI (Message Passing Interface) on distributed memory machines. Recently, a new parallelisation has been implemented in which the data is distributed in a "pencil-based" 2D manner instead of the previous "slice-based" 1D way. Figure 4.2 shows a performance of the benchmark case ($512 \times 513 \times 512$) and very good speedup of the code is obtained.

CHAPTER 5

Summary of the papers

Paper 1

Spectral simulations of wall-bounded flows on massively-parallel computers.
In order to take advantages of the large number of processors which the massively parallel computer systems usually have, a new 2D parallelisation of the code **SIMSON** is introduced in this report. The performance of the major subroutines is analysed in detail to identify the bottle-necks of the code. The overall performance of the new 2D version is promising. In addition, a performance model is proposed and it predicts the performance well for the benchmark cases.

Paper 2

Turbulent boundary layers up to $Re_\theta = 2500$ *studied through simulation and experiment.*
Twenty years passed since the first numerical simulation of turbulent boundary layer was done. However, the Reynolds number achieved then is still among the highest despite the rapid development of super computers and algorithms. This article is about a joint experimental/DNS work of a flat-plate turbulent boundary layer aiming at providing the research community with reliable data for a truly spatially developing flow. It is the fist time that the Reynolds number is high enough to compare DNS to carefully obtained experimental data. On the other hand, it is also a big challenge for the experimentalists to conduct an experiment at such a low Reynolds number with good quality. The excellent match of the data obtained from both simulation and experiments indicates that quantities of interest are not sensitive to the experimental and numerical limitations.

Paper 3

Simulations of high-Reynolds number turbulent boundary layers.
This paper is a continuation of the previous work of a flat-plate turbulent boundary layer using LES technique reaching the high $Re_\theta = 4300$. A promising LES model is used with comparably good resolution and the results obtained at lower Reynolds number $Re_\theta = 2500$ compare very well with the DNS data. With the high Reynolds number reached in this study, the scale separation is much more clearer and the outer structures are studied through

one-dimensional spanwise and temporal premultiplied spectra. The coherent structures observed in the simulation compare very well with previous experimental studies at similar Reynolds number.

Paper 4

DNS of a spatially developing turbulent boundary layer with passive scalar transport.
A turbulent boundary layer is simulated together with five different passive scalars upto $Re_\theta = 830$. The focus is on the outer region behaviour of the scalar statistics which is distinct from channel flows. The influences of the different boundary conditions and Prandtl numbers are also discussed. With such a variety of scalars, the Reynolds number reached in this study is the highest in the current literature.

Paper 5

Simulations of heat transfer of a boundary layer subject to free-stream turbulence.
This proceeding article is a continuation of the work presented in Paper 4 but with additional influence of the free-stream turbulence. It has been long time that researchers have observed that in the presence of free-stream turbulence, the heat transfer on solid walls increases dramatically. Since there are difficulties in experiments to measure very close to the wall, numerical simulations become a good alternative to shed light on the physical mechanisms. The present study summarises the previous experimental and simulation results, and furthermore attributes the increase of the heat transfer on the wall to the large-scale structures residing in the outer region of the boundary layer.

CHAPTER 6

Conclusions and outlook

In the present thesis, spatially evolving turbulent boundary layers together with passive scalars are investigated numerically. The research code is parallelised so that it can run on more than 1000 processors and this together with the quickly developing parallel computer systems opens the possibility to study wall turbulence at numerically very high Reynolds numbers.

The close agreement with the experimental data at $Re_\theta = 2500$ increases the credibility of obtained statistics at the low to medium Reynolds numbers. It further validates that the results are insensitive to the details of the experimental and numerical setup, e.g. the surface roughness, tripping device, streamwise pressure gradients, boundary conditions. By analysing the spanwise and temporal spectra, the large-scale structure is found to be about $0.85\delta_{99}$ in width and persists for about $10\delta_{99}/U_\infty$ time units.

For the results pertaining to heat transfer, the mean scalar profiles are independent of the different boundary conditions whereas the effects on the scalar variances and high-order statistics are obvious in the near-wall region. The scalar with isoscalar boundary condition is highly correlated with the streamwise velocity component in the near-wall region. However, near the boundary-layer edge, only a mild correlation between these two quantities was observed. With the presence of free-stream turbulence, a more prominent depression of the wake region can be observed with increasing turbulence intensity for the mean velocity and temperature profiles. As much as 15% increases of both the skin-friction coefficient and the Stanton number are found for a turbulence intensity of 20% at the inlet.

Therefore, a natural extension of the present work is to simulate such canonical flows at even higher Reynolds numbers since most engineering applications happen at very high Reynolds numbers. With the present increasing speed of the computer power, by the middle of 21 century, to simulate the wing of an airplane will not be a dream anymore. Another possibility is to study the vortical structures residing in the outer layer of the boundary layer in details. One and two-dimensional spectra will be analysed and visualisations of those structures will be done, see also Figure 6.1.

For the SGS modelling, the various models used in the present work have been shown to be very efficient and accurate. Recently, a new variant of mixed model, e.g. HPF-WALE model, also shows promising results in channel flows.

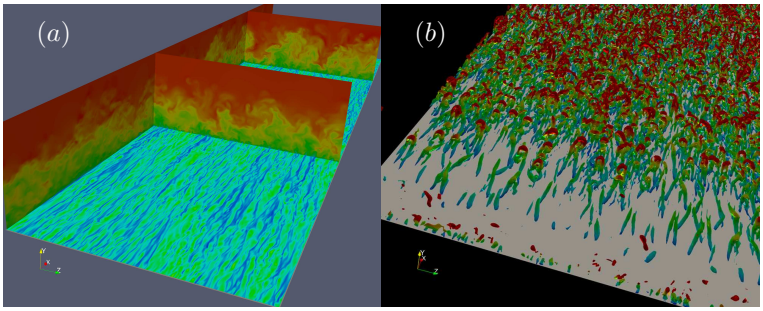

FIGURE 6.1. (*a*) A visualisation of an instantaneous flow field at $Re_\theta \approx 4000$. (*b*) Iso-surfaces of the second invariant of the velocity gradient tensor Q. See also Wu & Moin (2009).

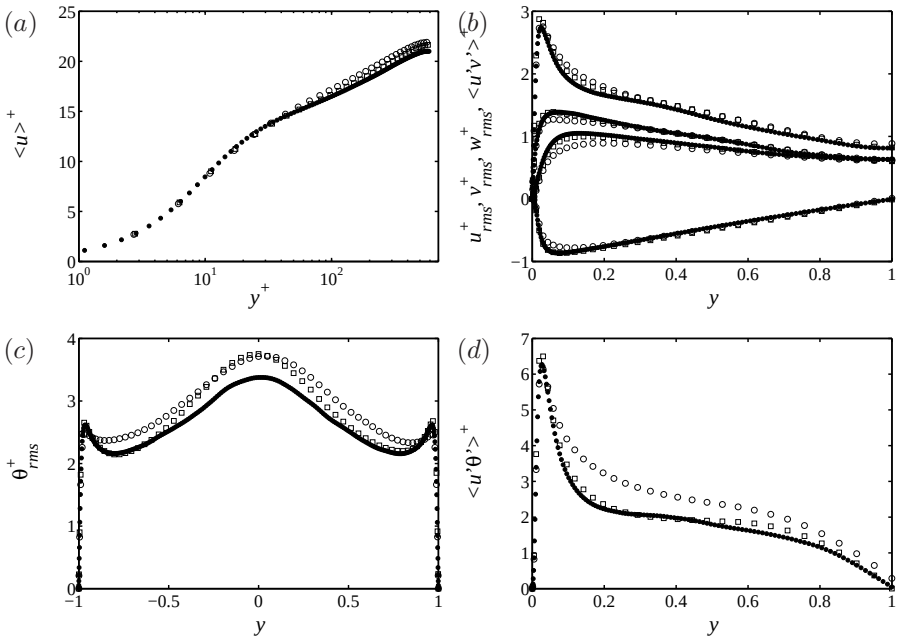

FIGURE 6.2. LES results of channel flow with passive scalar ($Pr = 0.71$) at $Re_\tau = 590$. • DNS (unfiltered), ∘ DSM model, ▫ HPF-WALE model.

Extensions of these models including passive scalar are interesting. Preliminary results of channel flow simulations with heat transfer ($Pr = 0.71$) at $Re_\tau = 590$ are shown in Figure 6.2 with comparison to the results obtained using DSM model and DNS data. In general, the results obtained with the new HPF-WALE model outperform those from DSM model. Both models overpredict the

mean velocity and scalar variance profiles in the centre of the channel. However, the resolved stresses and scalar fluxes predicted by the HPF-WALE model are in good agreement with the unfiltered DNS data. Further validation of these models will be performed in zero-pressure gradient turbulent boundary layers since whether the LES models are able to reproduce the high Reynolds number effects in turbulent boundary layer flows or not is still an open question. Other alternatives will be to investigate LES models which account for anisotropy, e.g. the explicit algebraic Reynolds stress model (EARSM) developed by Marstorp (2008). It is also interesting to combine the stochastic modelling approach with the available models. Furthermore, to test the SGS models in non-equilibrium situations and flows with separation induced by adverse pressure gradient would also be interesting.

Acknowledgements

The present thesis is the summary of about two and a half years of research in Prof. Dan S. Henningson's group at KTH Mechanics. During this time I did not only learn a lot on fluid mechanics and numerical simulation but I also enjoyed the kindly atmosphere in our group.

I would like to thank my supervisor Prof. Dan Henningson for guiding me through my studies and taking me as a student. Many many thanks to my co-advisor Dr. Philipp Schlatter for sharing his vast knowledge and experience in numerical simulations and persistent patience with me. Dr. Ardeshir Hanifi and Dr. Luca Brandt are also acknowledged for their help and sense of humour.

Thanks a lot to Dr. Schlatter, Dr. Duguet and Dipl.-Ing. Schrader for comments on the manuscript.

I would also like to thank: Andreas Vallgren, Antonios Monokrousos, David Tempelmann, Espen Åkervik, Gataneo Sardina, Hanno Essén, Johan Ohlsson, Lars-Uve Schrader, Linus Marstorp, Onofrio Semeraro, Peter Lenaers, Ramis Örlü, Shervin Bagheri, Stefan Ivanell, Yohann Duguet, and all the others at Mechanics for making social life enjoyable.

Thanks a lot for the funding supplier. In addition, computer time was provided by SNIC (Swedish National Infrastructure for Computing). The simulations were run at the Centre for Parallel Computers (PDC) at the Royal Institute of Technology (KTH) and the National Supercomputer Centre (NSC) at Linköping University in Sweden.

Gan xie jia ren he qin qi peng you dui wo de guan huai!

Bibliography

Abe, H. & Kawamura, H. 2002 A study of turbulence thermal structure in a channel flow through DNS up to $Re_\tau = 640$ with $Pr = 0.025$ and 0.71. In *Advances in Turbulence IX* (ed. I. P. Castro, P. E. Hancock & T. G. Thomas), pp. 399–402. CIMNE, Barcelona, Spain.

Abe, H., Kawamura, H. & Choi, H. 2004 Very large-scale structures and their effects on the wall shear-stress fluctuations in a turbulent channel flow up to $Re_\tau = 640$. *ASME J. Fluids Engng.* **126** (5), 835–843.

del Álamo, J. C. & Jiménez, J. 2003 Spectra of the very large anisotropic scales in turbulent channels. *Phys. Fluids* **15** (6), L41–L44.

Batchelor, G. K. 1959 Small-scale variation of convected quantities like temperature in turbulent fluid: Part 1. General discussion and the case of small conductivity. *J. Fluid Mech.* **5**, 113–133.

Bell, D. M. & Ferziger, J. H. 1993 Turbulent boundary layer DNS with passive scalars. In *Near-Wall Turbulent Flows* (ed. R. M. C. So, C. G. Speziale & B. E. Launder), pp. 327–366. Elsevier, Amsterdam, The Netherlands.

Bertolotti, F. P., Herbert, T. & Spalart, P. R. 1992 Linear and nonlinear stability of the Blasius boundary layer. *J. Fluid Mech.* **242**, 441–474.

Blair, M. F. 1983*a* Influence of free-stream turbulence on turbulent boundary layer heat transfer and mean profile development, Part I – Experimental data. *ASME J. Heat Transfer* **105**, 33–40.

Blair, M. F. 1983*b* Influence of free-stream turbulence on turbulent boundary layer heat transfer and mean profile development, Part II – Analysis of results. *ASME J. Heat Transfer* **105**, 41–47.

Brandt, L., Schlatter, P. & Henningson, D. S. 2004 Transition in boundary layers subject to free-stream turbulence. *J. Fluid Mech.* **517**, 167–198.

Bruhn, T. 2006 Large-eddy simulation of zero-pressure gradient turbulent boundary layers. Master's thesis, KTH Mechanics, Stockholm, Sweden.

Canuto, C., Hussaini, M. Y., Quarteroni, A. & Zang, T. A. 1988 *Spectral Methods in Fluid Dynamics*. Springer, Berlin, Germany.

Carati, D., Winckelmans, G. S. & Jeanmart, H. 2001 On the modelling of the subgrid-scale and filtered-scale stress tensors in large-eddy simulation. *J. Fluid Mech.* **441**, 119–138.

Chapman, D. R. 1979 Computatisnal aerodynamics development and outlook. *AIAA J.* **17** (12), 1293–1313.

Chevalier, M., Schlatter, P., Lundbladh, A. & Henningson, D. S. 2007 A pseudo-spectral solver for incompressible boundary layer flows. *Tech. Rep* TRITA-MEK 2007:07. Royal Institute of Technology, Stockholm.

Clark, R. A., Ferziger, J. H. & Reynolds, W. C. 1979 Evaluation of subgrid-scale models using an accurately simulated turbulent flow. *J. Fluid Mech.* **91** (1), 1–16.

Deardorff, J. W. 1970 A numerical study of three-dimensional turbulent channel flow at large Reynolds numbers. *J. Fluid Mech.* **41** (2), 453–480.

van Driest, E. R. 1956 On the turbulent flow near a wall. *J. Aero. Sci.* **23**, 1007–1011.

Ducros, F., Comte, P. & Lesieur, M. 1996 Large-eddy simulation of transition to turbulence in a boundary layer developing spatially over a flat plate. *J. Fluid Mech.* **326**, 1–36.

Fröhlich, J. & Rodi, W. 2002 Introduction to large-eddy simulation of turbulent flows. In *Closure Strategies for Turbulent and Transitional Flows* (ed. B. E. Launder & N. D. Sandham), pp. 267–298. Cambridge University Press, Cambridge, U.K.

George, W. K. & Castillo, L. 1997 Zero-pressure-gradient turbulent boundary layer. *ASME Appl. Mech. Rev.* **50** (12), 689–729.

Germano, M. 1992 Turbulence: the filtering approach. *J. Fluid Mech.* **238**, 325–336.

Germano, M., Piomelli, U., Moin, P. & Cabot, W. H. 1991 A dynamic subgrid-scale eddy viscosity model. *Phys. Fluids A* **3** (7), 1760–1765.

Geurts, B. J. 1999 Balancing errors in LES. In *Direct and Large-Eddy Simulation III* (ed. N. D. Sandham, P. R. Voke & L. Kleiser), pp. 1–12. Springer-Verlag, Berlin, Germany.

Geurts, B. J. 2003 *Elements of Direct and Large-Eddy Simulation*. R.T. Edwards, U.S.A.

Geurts, B. J. & Leonard, A. 2002 Is LES ready for complex flows? In *Closure Strategies for Turbulent and Transitional Flows* (ed. B. E. Launder & N. D. Sandham), pp. 720–739. Cambridge University Press, Cambridge, U.K.

Grosch, C. E. & Salwen, H. 1978 The continuous spectrum of the Orr-Sommerfeld equation. Part 1. The spectrum and the eigenfunctions. *J. Fluid Mech.* **87** (1), 33–54.

Härtel, C., Kleiser, L., Unger, F. & Friedrich, R. 1994 Subgrid-scale energy transfer in the near-wall region of turbulent flows. *Phys. Fluids* **6** (9), 3130–3143.

Hughes, T. J. R., Mazzei, L. & Jansen, K. E. 2000 Large eddy simulation and the variational multiscale method. *Comput. Visual. Sci.* **3**, 47–59.

Hughes, T. J. R., Oberai, A. A. & Mazzei, L. 2001 Large eddy simulation of turbulent channel flows by the variational multiscale method. *Phys. Fluids* **13** (6), 1784–1799.

Hutchins, N. & Marusic, I. 2007*a* Evidence of very long meandering features in the logarithmic region of turbulent boundary layers. *J. Fluid Mech.* **579**, 1–28.

Hutchins, N. & Marusic, I. 2007*b* Large-scale influences in near-wall turbulence. *Proc. Roy. Soc. Lond. Ser. A* **365**, 647–664.

Iritani, Y., Kasagi, N. & Hirata, M. 1985 Heat transfer mechanism and associated turbulence structure in a near wall region of a turbulent boundary layer. In

Turbulent Shear Flows 4 (ed. L. J. S. Bradburry, F. Durst, B. E. Launder, F. W. Schmidt & J. H. Whitelaw), pp. 223–234. Springer-Verlag, Berlin, Germany.

Jackson, D. & Launder, B. 2007 Osborne Reynolds and the publication of his papers on turbulent flow. *Ann. Rev. Fluid Mech.* **39**, 19–35.

Jacobs, R. G. & Durbin, P. A. 2000 Bypass transition phenomena studies by computer simulation. *Tech. Rep* TF-77. Stanford University, U.S.A.

Jeanmart, H. & Winckelmans, G. S. 2007 Investigation of eddy-viscosity models modified using discrete filters: A simplified "regularized variational multiscale model" and an "enhanced field model". *Phys. Fluids* **19** (5), 055110.

Jiménez, J. 2003 Computing high-Reynolds-number turbulence: will simulations ever replace experiments? *J. Turbulence* **4** (22), 1–14.

Jiménez, J. & Pinelli, A. 1999 The autonomous cycle of near-wall turbulence. *J. Fluid Mech.* **389**, 335–359.

Karamanos, G.-S. & Karniadakis, G. E. 2000 A spectral vanishing viscosity method for large-eddy simulations. *J. Comp. Phys.* **163**, 22–50.

Karniadakis, G. & Sherwin, S. 2005 *Spectral/hp element methods for computational fluid dynamics*. Oxford University Press, Oxford, U.K.

Kasagi, N. & Iida, O. 1999 Progress in direct numerical simulation of turbulent heat transfer. In *Proceedings of the 5th ASME/JSME Joint Thermal Engineering Conference, San Diego, U.S.A.*.

Kim, H. T., Kline, S. J. & Reynolds, W. C. 1971 The production of turbulence near a smooth wall in a turbulent boundary layer. *J. Fluid Mech.* **50**, 133–160.

Kim, J. & Moin, P. 1989 Transport of passive scalars in a turbulent channel flow. In *Turbulent Shear Flows 6* (ed. J.-C. André, J. Cousteix, F. Durst, B. E. Launder & F. W. Schmidt), pp. 85–96. Springer-Verlag, Berlin, Germany.

Kim, J., Moin, P. & Moser, R. 1987 Turbulence statistics in fully developed channel flow at low Reynolds number. *J. Fluid Mech.* **177**, 133–166.

Kim, K. C. & Adrian, R. J. 1999 Very large-scale motion in the outer layer. *Phys. Fluids* **11** (2), 417–422.

Kline, S. J., Reynolds, W. C., Schraub, F. A. & Runstadler, P. W. 1967 The structure of turbulent boundary layers. *J. Fluid Mech.* **30**, 741–773.

Kong, H., Choi, H. & Lee, J. S. 2000 Direct numerical simulation of turbulent thermal boundary layers. *Phys. Fluids* **12** (10), 2555–2568.

Leonard, A. 1974 Energy cascade in large eddy simulation of turbulent fluid flows. *Adv. Geophys.* **18** (A), 237–248.

Leonard, A. & Winckelmans, G. S. 1999 A tensor-diffusivity subgrid model for large-eddy simulation. In *Proc. Isaac Newton Institute Symposium / ERCOFTAC Workshop*, pp. 12–14. Kluwer, Dordrecht, The Netherlands.

Lesier, M., Métais, O. & Comte, P. 2005 *Large-Eddy Simulation of Turbulence*. Cambridge University Press, Cambridge, U.K.

Li, Q., Schlatter, P., Brandt, L. & Henningson, D. S. 2009 DNS of a spatially developing turbulent boundary layer with passive scalar transport. *Int. J. Heat Fluid Flow* In press.

Libby, P. A. 1996 *Introduction to Turbulence*. Taylor & Francis, New York, U.S.A.

Lilly, D. K. 1967 The representation of small-scale turbulence in numerical simulation experiments. In *Proc. IBM Scientific Computing Symp. on Environmental Sciences, Yorktown Heights, New York* (ed. H. H. Goldstine), pp. 195–210.

Lilly, D. K. 1992 A proposed modification of the Germano subgrid-scale closure method. *Phys. Fluids A* **4** (3), 633–635.

Lin, J., Laval, J. P., Foucaut, J. M. & Stanislas, M. 2008 Quantitative characterization of coherent structures in the buffer layer of near-wall turbulence. Part 1: streaks. *Exp. Fluids* **45**, 999–1013.

Lu, S. S. & Willmarth, W. W. 1973 Measurements of the structure of the Reynolds stress in a turbulent boundary layer. *J. Fluid Mech.* **60**, 481–511.

Lund, T. S., Wu, X. & Squires, K. D. 1998 Generation of turbulent inflow data for spatially-developing boundary layer simulations. *J. Comp. Phys.* **140**, 133–158.

Maday, Y. & Patera, A. T. 1989 Spectral element methods for the incompressible navier-stokes equations. In *State-of-the-art surveys on computational mechanics, ASME, New York* (ed. A. K. Noor & J. T. Oden), pp. 71–143.

Marstorp, L. 2008 Modelling of subgrid-scale stress and passive scalar flux in large-eddy simulations of wall bounded turbulent flows. PhD thesis, Department of Mechanics, KTH, Stockholm, Sweden.

McMillan, O. J., Ferziger, J. H. & Rogallo, R. S. 1980 Tests of subgrid-scale models in strained turbulence. In *13th AIAA Fluid and Plasma Dynamics Conference, Snowmass, Colo., U.S.A.*.

Meneveau, C. 1994 Statistics of turbulence subgrid-scale stresses: Necessary conditions and experimental tests. *Phys. Fluids* **6** (2), 815–833.

Métais, O. & Lesieur, M. 1992 Spectral large-eddy simulation of isotropic and stably stratified turbulence. *J. Fluid Mech.* **239**, 157–194.

Millikan, C. M. 1938 A critical discussion of turbulent flows in channels and circular tubes. In *Proceedings of the 5th International Congress on Applied Mechanics, Cambridge, M.A., U.S.A.* (ed. J. P. Den Hartog & H. Peters), pp. 386–392. Wiley, New York, U.S.A.

Moin, P. & Kim, J. 1982 Numerical investigation of turbulent channel flow. *J. Fluid Mech.* **118**, 341–377.

Moin, P. & Mahesh, K. 1998 Direct numerical simulation: A tool in turbulence research. *Ann. Rev. Fluid Mech.* **30**, 539–578.

Nagib, H. M. & Chauhan, K. A. 2008 Variations of von Kármán coefficient in canonical flows. *Phys. Fluids* **20** (10), 101518.

Nagib, H. M., Chauhan, K. A. & Monkewitz, P. A. 2007 Approach to an asymptotic state for zero pressure gradient turbulent boundary layers. *Proc. Roy. Soc. Lond. Ser. A* **365**, 755–770.

Nicoud, F. & Ducros, F. 1999 Subgrid-scale stress modelling based on the square of the velocity gradient tensor. *Flow Turbulence Combust.* **62**, 183–200.

Nordström, J., Nordin, N. & Henningson, D. S. 1999 The fringe region technique and the Fourier method used in the Direct Numerical Simulation of spatially evolving viscous flows. *SIAM J. Sci. Comp.* **20** (4), 1365–1393.

Orszag, S. A. & Patterson, G. S. 1972 Numerical simulation of three-dimensional homogeneous isotropic turbulence. *Phys. Lett. Rev.* **28** (2), 76–79.

Patera, A. T. 1984 A spectral element method for fluid dynamics - laminar flow in a channel expansion. *J. Comp. Phys.* **54**, 468–488.

Piomelli, U. 2001 Large-eddy and direct simulation of turbulent flows. In *CFD2001 - 9e conférence annuelle de la société Canadienne de CFD*. Kitchener, Ontario, Canada.

Piomelli, U. & Balaras, E. 2002 Wall-layer models for large-eddy simulations. *Ann. Rev. Fluid Mech.* **34**, 349–374.

Piomelli, U., Cabot, W. H., Moin, P. & Lee, S. 1991 Subgrid-scale backscatter in turbulent and transitional flows. *Phys. Fluids A* **3** (7), 1766–1771.

Piomelli, U., Moin, P. & Ferziger, J. H. 1988 Model consistency in large eddy simulation of turbulent channel flows. *Phys. Fluids* **31** (7), 1884–1891.

Pope, S. B. 2000 *Turbulent Flows*. Cambridge University Press, Cambridge, U.K.

Reynolds, W. C. 1989 The potential and limitations of direct and large eddy simulations. In *Whither Turbulence? Turbulence at the Crossroads* (ed. J. L. Lumley), *Lecture Notes in Physics*, vol. 357, pp. 313–343. Springer-Verlag, Berlin, Germany.

Robinson, S. K. 1991 Coherent motions in the turbulent boundary layer. *Ann. Rev. Fluid Mech.* **23**, 601–639.

Rogallo, R. S. & Moin, P. 1984 Numerical simulation of turbulent flows. *Ann. Rev. Fluid Mech.* **16** (1), 99–137.

Rogers, M., Moin, P. & Reynolds, W. 1986 The structure and modeling of the hydrodynamic and passive scalar fields in homogeneous turbulent shear flow. *Tech. Rep* TF-25. Stanford University, U.S.A.

Sagaut, P. 2005 *Large Eddy Simulation for Incompressible Flows, An Introduction*, 3rd edn. Springer, Berlin, Germany.

Sagaut, P., Comte, P. & Ducros, F. 2000 Filtered subgrid-scale models. *Phys. Fluids* **12** (1), 233–236.

Sandham, N. D. 2002 Introduction to direct numerical simulation. In *Closure Strategies for Turbulent and Transitional Flows* (ed. B. E. Launder & N. D. Sandham), pp. 248–266. Cambridge University Press, Cambridge, U.K.

Schlatter, P. 2001 Direct numerical simulation of laminar-turbulent transition in boundary layer subject to free-stream turbulence. Master's thesis, Institute of Fluid Dynamics, ETH, Zürich, Switzerland.

Schlatter, P., Brandt, L., Bruhn, T. & Henningson, D. S. 2006*a* Dynamic high-pass filtered eddy-viscosity models for LES of turbulent boundary layers. In *Bulletin American Physical Society*, , vol. 51, p. 213.

Schlatter, P., Li, Q., Brethouwer, G., Johansson, A. V. & Henningson, D. S. 2009*a* Towards large-eddy simulations of high-Reynolds number turbulent boundary layers. In *TSFP-7, June 2009, Seoul, Korea* (ed. N. Kasagi, J. K. Eaton, R. Friedrich, J. A. C. Humphrey, A. V. Johansson & H. J. Sung), , vol. I, pp. 271–276.

Schlatter, P., Örlü, R., Li, Q., Brethouwer, G., Fransson, J. H. M., Johansson, A. V., Alfredsson, P. H. & Henningson, D. S. 2009*b* Turbulent boundary layers up to $Re_\theta = 2500$ studied through numerical simulation and experiments. *Phys. Fluids* **21** (5), 051702.

Schlatter, P., Stolz, S. & Kleiser, L. 2004 LES of transitional flows using the approximate deconvolution model. *Int. J. Heat Fluid Flow* **25** (3), 549–558.

Schlatter, P., Stolz, S. & Kleiser, L. 2005 Evaluation of high-pass filtered eddy-viscosity models for large-eddy simulation of turbulent flows. *J. Turbulence* **6** (5), 1–21.

Schlatter, P., Stolz, S. & Kleiser, L. 2006*b* Analysis of the SGS energy budget for deconvolution- and relaxation-based models in channel flow. In *Direct and*

Large-Eddy Simulation VI (ed. R. Friedrich, B. J. Geurts & O. Métais), pp. 135–142. Kluwer, Dordrecht, The Netherlands.

Schlatter, P., Stolz, S. & Kleiser, L. 2006*c* LES of spatial transition in plane channel flow. *J. Turbulence* **7** (33), 1–24.

Simonich, J. C. & Bradshaw, P. 1978 Effect of free-stream turbulence on heat transfer through a turbulent boundary layer. *ASME J. Heat Transfer* **100** (4), 671–677.

Smagorinsky, J. 1963 General circulation experiments with the primitive equations. *Mon. Wea. Rev.* **91**, 99–164.

Smith, C. R. & Metzler, S. P. 1983 The characteristics of low-speed streaks in the near-wall region of a turbulent boundary layer. *J. Fluid Mech.* **129**, 27–54.

Spalart, P. R. 1988 Direct simulation of a turbulent boundary layer up to $Re_\theta = 1410$. *J. Fluid Mech.* **187**, 61–98.

Spalart, P. R. 2009 Detached-eddy simulation. *Ann. Rev. Fluid Mech.* **41** (1), 181–202.

Stolz, S. & Adams, N. A. 1999 An approximate deconvolution procedure for large-eddy simulation. *Phys. Fluids* **11** (7), 1699–1701.

Stolz, S. & Adams, N. A. 2003 Large-eddy simulation of high-Reynolds-number supersonic boundary layers using the approximate deconvolution model and a rescaling and recycling technique. *Phys. Fluids* **15** (8), 2398–2412.

Stolz, S., Adams, N. A. & Kleiser, L. 2001*a* An approximate deconvolution model for large-eddy simulation with application to incompressible wall-bounded flows. *Phys. Fluids* **13** (4), 997–1015.

Stolz, S., Adams, N. A. & Kleiser, L. 2001*b* The approximate deconvolution model for large-eddy simulations of compressible flows and its application to shock-turbulent-boundary-layer interaction. *Phys. Fluids* **13** (10), 2985–3001.

Stolz, S., Schlatter, P. & Kleiser, L. 2005 High-pass filtered eddy-viscosity models for large-eddy simulations of transitional and turbulent flow. *Phys. Fluids* **17** (6), 065103.

Tennekes, H. & Lumley, J. L. 1972 *A First Course in Turbulence*. The MIT Press, Cambridge, U.S.A.

Townsend, A. A. 1976 *The Structure of Turbulent Shear Flow*. Cambridge University Press, Cambridge, U.K.

Vreman, A. W. 2003 The filtering analog of the variational multiscale method in large-eddy simulation. *Phys. Fluids* **18**, L61–L64.

Vreman, B., Geurts, B. & Kuerten, H. 1995 A priori test of large eddy simulation of the compressible plane mixing layer. *Journal of Engineering and Mathematics* **29** (4), 299–327.

Wallace, J. M., Eckelmann, H. & Brodkey, R. S. 1972 The wall region in turbulent shear flow. *J. Fluid Mech.* **54**, 39–48.

Warhaft, Z. 2000 Passive scalars in turbulent flows. *Ann. Rev. Fluid Mech.* **32**, 203–240.

White, F. M. 2006 *Viscous Fluid Flow*, 3rd edn. McGraw-Hill, New York, U.S.A.

Willmarth, W. W. & Lu, S. S. 1972 Structures of the Reynolds stress near the wall. *J. Fluid Mech.* **55**, 65–92.

Winckelmans, G. S., Jeanmart, H. & Carati, D. 2002 On the comparison of

turbulence intensities from large-eddy simulation with those from experiment or direct numerical simulation. *Phys. Fluids* **14** (5), 1809–1811.

Winckelmans, G. S., Wray, A. A., Vasilyev, O. V. & Jeanmart, H. 2001 Explicit-filtering large-eddy simulation using the tensor-diffusivity model supplemented by a dynamic Smagorinsky term. *Phys. Fluids* **13** (5), 1385–1403.

Wu, X. & Moin, P. 2009 Direct numerical simulation of turbulence in a nominally zero-pressure-gradient flat-plate boundary layer. *J. Fluid Mech.* **630**, 5–41.

Part II

Papers

1

Paper 1

Spectral simulations of wall-bounded flows on massively-parallel computers

By Qiang Li, Philipp Schlatter & Dan S. Henningson

Linné Flow Centre, KTH Mechanics
SE-100 44 Stockholm, Sweden

Technical report

1. Introduction

Due to the rapid development of high-performance super-computers for the last several decades, highly resolved time-dependent numerical simulations, i.e. direct numerical simulation (DNS) and large-eddy simulation (LES), have become an important tool for transition and turbulence research (Moin & Mahesh 1998; Sagaut 2005).

Such super-computers can be primarily classified into two groups with respect to the architecture of the processor: vector processor and scalar processor. A vector processor, or array processor, is designed with the so-called vector registers which are able to operate on multiple data elements simultaneously, thus the operations are done in parallel at least to some extent. In contrast, a scalar processor has registers for data as a scalar quantity and in principle only processes one data element at a time. Vector processors were widely used to form the basis of most super computers in the 1980s and 1990s, but have nearly disappeared in super-computers nowadays. Another classification of super-computers is according to the memory configuration. Shared and distributed memory are the two main memory configurations. In the former case, all the processors share the same memory while in the latter one, each processor has its own memory so that data has to be sent and received if used by another processor. According to the categories above, there are four different combinations of the types of the computers as shown in Table 1. Throughout this report, only the first combination, i.e. scalar processors with distributed memory, is considered and discussed since this is the most dominant architecture in use with most Linux clusters at the moment. The term "processor" means central processing unit (CPU) and will alternatively be termed "core".

	distributed memory	shared memory
scalar processor	1	2
vector processor	3	4

TABLE 1. The four combinations of the types for the parallel computers.

The simplest parallel computing architecture might be the multi-core architecture usually consisting of two or more independent cores. The cores may or may not share the memory and message passing or shared memory inter-core communication methods may be implemented. Another type is a distributed memory computer system, e.g. a computer cluster, consisting of a group of independent computers which are connected by network such that they can work together and can be viewed as a single parallel machine. A cluster has usually about 200 to 300 processors in total. However, in order to obtain higher performance to solve large-size problems, a massively parallel computer system has to be used. A massively parallel computer system is a single machine with a very large number of processors, usually more than 1000 processors. In such a system, a single processor may have a lower performance compared to a processor of a regular cluster, but this is compensated by the larger amount of processors. All the processors are connected via a high speed interconnection. Therefore, the overall performance might be better than a common cluster depending on the application.

Once equipped with a modern parallel computer, the availability of an efficient numerical code for simulating turbulent flow becomes more important. An efficient numerical code (**SIMSON**) to solve the Navier–Stokes equations for incompressible channel and boundary-layer flows has been developed at KTH Mechanics for the last years, see the reports by Lundbladh *et al.* (1992), Lundbladh *et al.* (1999) and Chevalier *et al.* (2007). The numerical method is based on a standard fully spectral Fourier/Chebyshev discretization, leading to high numerical accuracy and efficiency. The nonlinear convective terms are evaluated pseudo-spectrally in physical space using fast Fourier transforms (FFT) to avoid the evaluation of convolution sums. Aliasing errors are removed by using the 3/2-rule (Canuto *et al.* 1988) in the wall-parallel directions. The governing equations are then solved and the prescribed boundary conditions are applied in Fourier/Chebyshev space. Time integration is done by a mixed third order Runge–Kutta/Crank–Nicolson method. The code can be run in either temporal mode or spatial mode. It also supports disturbance formulation and linearised formulation. Multiple passive scalars, e.g. a temperature field, can be solved together with the velocity field. For boundary-layer flows, the "fringe region" is added to fulfil the periodic boundary condition in the streamwise direction (Nordström et al. 1999).

2. Parallelisation

2.1. *Code structure*

The numerical code **SIMSON** is written in FORTRAN 77 and the coarse structure can be divided into four steps (Chevalier *et al.* 2007). In the first step, initialisation of the flow solver is done, e.g. reading in the input files, setting the initial parameter values, opening the output files, etc. In the second step, the time integration loop is started and the computations in physical space, i.e. the evaluation of non-linear terms, are executed. In the third step, the linear

part of the evolution equations are solved in Fourier/Chebyshev space and the time-stepping parameters are recalculated for the next time step. In the last step, the output files are written after the time integration loop is finished. The major computational effort of the code is in the subroutines `nonlinbl` (step 2) in which the nonlinear terms are calculated in physical space and `linearbl` (step 3) in which the linear part of the governing equations are solved and the boundary conditions are evaluated in Fourier/Chebyshev space, see also Figure 1. For a typical run in serial mode, it turns out that about 55% of the total execution time is spent in subroutine `nonlinbl` and 40% in subroutine `linearbl`.

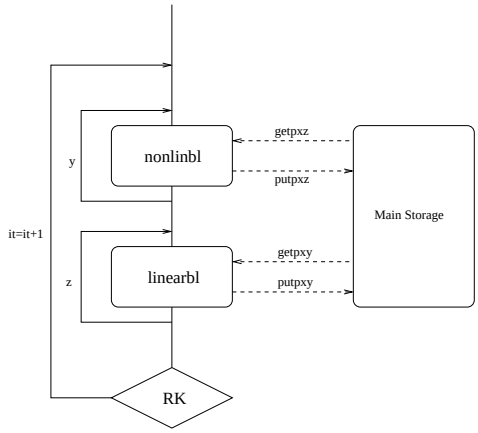

FIGURE 1. The main structure of the code for the 1D parallelisation.

2.2. *Domain decomposition*

The most straightforward parallelisation method is to use data parallelisation or domain decomposition through which the work has been divided among the processors so that each processor has approximately the same amount of work to do. Thus the efficiency is maximised and therefore the overall performance is greatly increased.

2.2.1. *1D parallelisation*

The main structure of the code for the 1D parallelisation is shown in Alvelius & Skote (2000). The computations are done plane by plane, i.e. in an xy-plane in `linearbl` and an xz-plane in `nonlinbl` where x, y and z are the spatial coordinates representing the streamwise, wall-normal and spanwise direction, respectively. Outside these subroutines, there is a loop over the third direction, i.e. z for `linearbl` and y for `nonlinbl`. This means that the calculation in each plane is independent of any other one. If one processor calculates one plane at each time, as many processors as there are planes can be used running in parallel. As seen from Figure 1, in order to get the data from the main

storage onto planes, the subroutines `getpxz` for `nonlinbl` and `getpxy` for `linearbl` are called. The corresponding subroutines for putting data back to the main storage after the calculations in `nonlinbl` and `linearbl` are `putpxz` and `putpxy`, respectively.

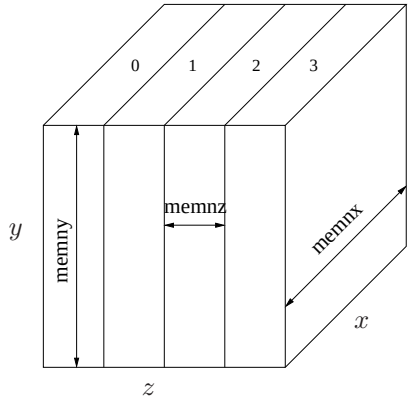

FIGURE 2. Data distribution among all the processors.

The code supports parallelisation with both shared memory (OpenMP) and distributed memory (MPI). Here only the distributed memory machines based on MPI communication are discussed in detail. The main storage is distributed in the z-direction only; a sketch of that distribution is shown in Figure 2. The data in the horizontal plane, i.e. xz-plane, is stored in Fourier space while the data in the wall-normal direction is in physical space. The total number of the processors is denoted by $nproc$. In the sketch $nproc = 4$ is chosen as an example. Then the amount of data stored on each processor is $2 \times memnx \times memny \times memnz$ where $memnx = \frac{nx}{2}$, $memny = nyp$ and $memnz = \frac{nz}{nproc}$. nx, nyp and nz are the number of collocation points in the streamwise, wall-normal and spanwise direction, respectively. $memnx$ is $\frac{nx}{2}$ becuase complex Fourier modes are considered; the factor 2 represents the real and imaginary parts. nyp has to be an odd number since it represents the total number of Chebyshev modes. By distributing the data in this way, the calculations in the subroutine `linearbl` are easily done in parallel since each processor has full access to the data on one xy-plane in each z-loop. Note that the subroutines `getpxy` and `putpxy` are called by all the processors at the same time and they operate on $nproc$ wall-normal planes seperated in z in each z-loop without involving communication between any two processors. However, when doing the calculations in the subroutine `nonlinbl`, in order to obtain full access to the data on an xz-plane, each processor has to collect data from all the other processors. The data collection is accomplished by calling the subroutines `getpxz` and `putpxz`. This global data transfer gives rise to a significant amount of communication among all the processors. In fact, the majority of the total communication among the processors happens in the

subroutine `nonlinbl`, more precisely in the subroutines `getpxz` and `putpxz`. As similarly for the subroutines `getpxy` and `putpxy`, the subroutines `getpxz` and `putpxz` are also called by all the processors at the same time but they operate on *nproc* consecutive wall-parallel planes in each y-loop.

The data distribution after the global communication is shown in Figure 3. After the global communication in `getpxz`, each processor has full access to the data in one xz-plane and is thus able to perform the 2D FFTs on this xz-plane to transform the data from spectral space to physical space. Since the cost of the communication is relatively high for parallel computers with distributed memory, the best way to implement the 2D FFTs is to perform the FFTs by each processor. Thus 1D FFTs have to be performed twice in both directions on each xz-plane. Following the FFTs, all the data is stored in physical space and then the nonlinear terms can be evaluated pseudo-spectrally. To remove the aliasing errors from the evaluation of the nonlinear terms, the 3/2-rule has been used. Once the calculation of the nonlinear terms is finished, inverse FFTs have to be performed to transform the data back to spectral space. Last, another global communication has to be done in `putpxz` to write the data back to the storage location as shown in Figure 2. Then the calculations in `linearbl` can be easily done. It turns out that the evaluation of FFTs are the main computational cost of the whole code which may take up to 55% of the total execution time for a serial run, i.e. without communication.

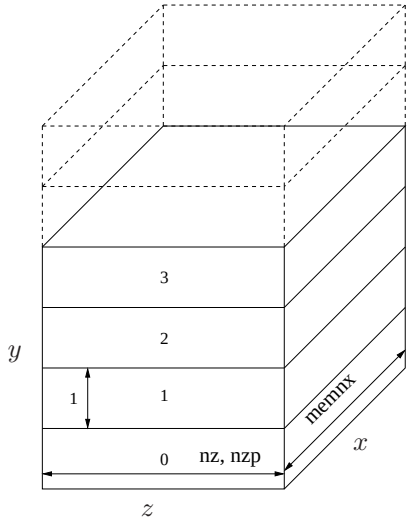

FIGURE 3. Data distribution after the global communication.

For the global communication needed in the subroutines `getpxz` and `putpxz`, two different ways are currently implemented. On the one hand, a self-written version of the global transpose which is based on the explicit point to point communication using MPI commands **MPI_ISEND**, **MPI_WAIT**

and **MPI_RECV** is available. For more details about this implementation, see Alvelius & Skote (2000). On the other hand, an alternative version is to adopt the standard collective communication command **MPI_ALLTOALL**. This standard MPI command transfers a subset of data from all members to

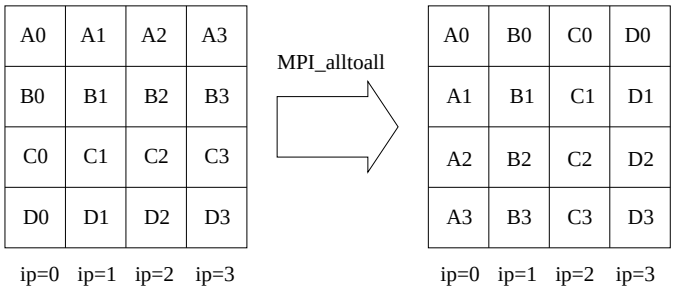

FIGURE 4. The **MPI_ALLTOALL** command illustrated for a group of four processors $ip = 0, 1, 2, 3$.

all members within a group. Each processor sends distinct data to each of the other processor. How the data is transfered is illustrated in Figure 4. As seen from the figure, the **MPI_ALLTOALL** actually does a global transpose of the data among all the members in the group. A performance model for the **MPI_ALLTOALL** is developed, see the later chapter for more detail.

Both versions of implementation for the global communication essentially perform approximately the same in terms of speed and memory requirement. However, if the collective communication version is used, the amount of data stored on each processors is slightly larger and thus the amount of communication compared to the hand-written version is marginally increased. This is because *memny* has to be $(\mathrm{int}(\frac{nyp}{nproc}) + 1) \times nproc$ instead of *nyp* to fulfil the requirement of the **MPI_ALLTOALL** command. The operation "int" means taking only the integer part. Another issue concerning the collective communication version is that user-defined data types including the **MPI_TYPE_STRUCTURE** and **MPI_UB** commands have to be used in order to fit the data structure of the code. These user-defined data types in the subroutines `getpxz` and `putpxz` are *realg*1 and *realg*2. *realg*1, representing the data type as in the Figure 2, has *memnz* blocks, *memnx* elements in each block and $memnx \times memny$ elements between the start of each block. An upper-bound of size *memnx* has to be added to the data type *realg*1 to give the correct displacement between consecutive elements. The upper-bound data type can be considered as a "pseudo-data type" which extends the upper bound of a data type. It does not have any effects on the content or the size of the data type and does not influence the message defined by the data type. What it changes is the spatial extent of the data type in the memory. The data type *realg*2, representing the data type as in the Figure 3,

has also $memnz$ blocks, $memnx$ elements in each block, but $(\frac{nxp}{2}+1)$ elements between the start of each block where $nxp = \frac{3}{2}nx$. An upper-bound of size $(\frac{nxp}{2}+1) \times memnz$ has also to be added to the data type $realg2$. Note that the two data types $realg1$ and $realg2$ have exactly the same size, i.e. they contain the same amount of real numbers. Different blocks of the same data type or different data types can be constructed as a general data type by using MPI command **MPI_TYPE_STRUCTURE**. For more about the user-defined data type, refer to MPI standard documentation.

2.2.2. *2D parallelisation*

The distribution of the main storage in only the spanwise direction introduced in the previous section naturally imposes a restriction to the code, i.e. the upper limit of the maximum possible number of processors to be nz. For typical flow cases, nz is not larger than 256. Nowadays, as the computer clusters become more powerful with more and more processors and cores available, a new way to parallelise the code is strongly needed such that more processors than just nz processors can be used.

There are potentially three possible spatial directions along which the data can be distributed among the different processors. The number of grid points in y, discretized by Chebyshev expansion, is required to be odd and thus not evenly divisible by the number of processors. So choosing y (the wall-normal) direction is out of consideration. Either x (the streamwise) or z (the spanwise) direction can be easily chosen as the direction to parallelise over since the number of the grid points in these two directions are naturally even and can be chosen to be divisible by the number of processors. The number of grid points in the streamwise direction is usually larger than that in the spanwise direction. If the streamwise direction is chosen to be the direction to parallelise over, it is possible to use more processors, however again limited by the number of modes in x. In addition, there might be a local load-levelling when treating the y and z directions with much less collocation points. Therefore, in order to fully exploit massively parallel computer systems with large amounts of processors and without being limited by the number of grid points in either the x or z direction, parallelising in both the x and z directions, i.e. a 2D parallelisation operating on a number of pencils, becomes a natural choice.

Hence the whole field (velocity, pressure or scalar) is distributed in both x and z direction among the different processors. A sketch of the data distribution is shown in Figure 5.

The main structure of the code for the 2D parallelisation is shown in Figure 6. It looks quite similar to the structure of the 1D parallelisation given in Figure 1. As seen from Figure 6, in order to get the data from the main storage onto part of the planes, subroutines `getpxz_z` in `nonlinbl` and `getpxy` in `linearbl` have to be called. The corresponding subroutines for putting data back to the main storage after calculations are `putpxz_z` for `nonlinbl` and `putpxy` for `linearbl`. In a similar way as for the 1D parallelisation, FFTs in both

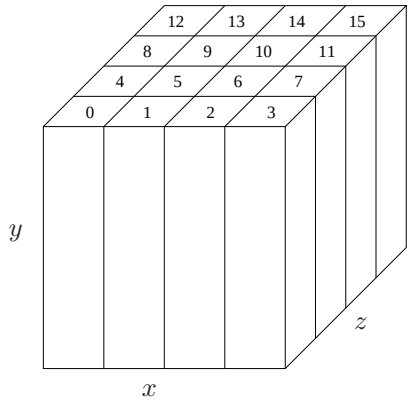

FIGURE 5. Initial data distribution among all the processors.

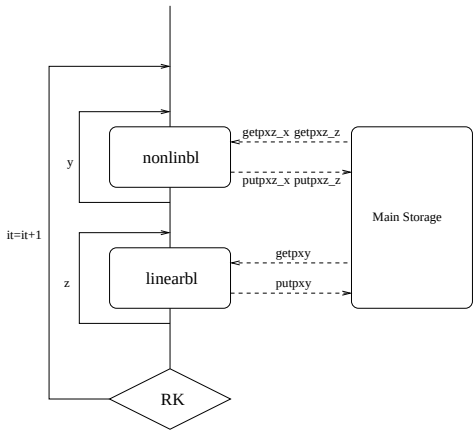

FIGURE 6. The main structure of the code for the 2D parallelisation. Note that there exist FFTs between calls to the subroutines `getpxz_z` and `getpxz_x` and inverse FFTs between calls to `putpxz_z` and `putpxz_x`.

directions in each xz-plane have to be performed by each processor. However, due to the data distribution on each xz-plane now, only the 1D FFT in the spanwise direction is possible to do without further communication. Thus in order to perform the 1D FFT in the streamwise direction, another global data communication has to be performed. This is done by calling the subroutine `getpxz_x`. The corresponding subroutine for putting data back to the temporary storage is `putpxz_x`. The details about both global data communications will be explained in later sections. Note that the global communication will inherently not scale linearly with the number of processors that are involved in the communication. This will pose a challenge for using large number of

processors. Again, most of the total communication of the code is in `nonlinbl` and the main computational effort is the FFTs.

Due to the 2D parallelisation, none of the processors has full access to the data of any whole xz-plane. When carrying out the communication and calculations, the processors are divided into different groups. These groups are different from the default MPI communication group, **MPI_COMM_WORLD**, which contains all the processors. At each time, only a certain fraction of the total number of the processors will be involved in each group to do the communication in each plane and different groups take care of the different planes. In this way all the processors then run in parallel. Again, similar to the 1D parallelisation, the subroutines `getpxz_z`, `getpxz_x`, `putpxz_z` and `putpxz_x` in `nonlinbl` are called by all the processors at the same time and $nprocz$ consecutive wall-parallel planes are treated in each y-loop. Remember that in the 1D parallelisation, the subroutines `getpxy` and `putpxy` in `linearbl` are called by all the processors at the same time and $nproc$ wall-parallel planes are treated simultaneously.

A short description of how the data is transferred in `nonlinbl` is given now. As depicted in Figure 5, initially the field is equally distributed among all the processors, here 16 processors are used as an example. $nproc$, $nprocx$ and $nprocz$ represent the number of the total processors, the processors in the x and z direction, respectively. Thus in this case $nproc = 16$ and $nprocx = nprocz = 4$. Note that with the present implementation of the 2D parallelisation, it is required that the number of processors should be equally distributed along both the x and z directions, i.e. $nprocx = nprocz = \sqrt{nproc}$. The size of the domain is $\frac{nx}{2}$ in x-direction, nz in z-direction and nyp in y-direction where nx, nyp and nz are the same as defined in the 1D parallelisation. Note that the size of the domain in the x-direction is $\frac{nx}{2}$ rather than nx which is due to the fact that the real and imaginary parts of the complex numbers are stored in separate arrays. The amount of data stored on each processor is $memnx \times memny \times memnz$ where $memnx = \frac{nx}{2nprocx}$, $memny = (\mathrm{int}(\frac{nyp}{nprocz}) + 1) \times nprocz$ and $memnz = \frac{nz}{nprocz}$.

For the 2D parallelisation, the global communication is implemented only using the standard collective MPI command **MPI_ALLTOALL**, so $memny$ needs to be $(\mathrm{int}(\frac{nyp}{nprocz}) + 1) \times nprocz$. To make the transfer of data more efficient, user-defined data type rather than the default ones provided by the MPI library have to be used. The data types used in the subroutines `getpxz_z` and `putpxz_z` are $realg1$ and $realg2$. $realg1$ has $memnz$ blocks, $memnx$ elements in each block and $memnx \times memny$ elements between the start of each block. As detailed previously, an upper-bound (**MPI_UB**) of $memnx$ has to be added to the data type $realg1$. The data type $realg2$ has $memnz$ blocks, $memnx$ elements in each block and $memnx$ elements between the start of each block. Note that no explicit upper-bound element is needed here. In the subroutines `getpxz_x` and `putpxz_x`, the data types used are $realg3$ and $realg4$. The data

type $realg3$ has $\frac{nzp}{nprocz}$ blocks, $memnx$ elements in each block and $memnx$ elements between the start of each block while $realg4$ has $\frac{nzp}{nprocz}$ blocks, $memnx$ elements in each block and $(\frac{nxp}{2}+1)$ elements between the beginning of each block, again a upper-bound of size $memnx$ has to be used for $realg4$. Similar to the 1D parallelisation, $realg1$ and $realg2$ have the exact same size and represent the data types before and after the transpose. This is also true for $realg3$ and $realg4$. nxp and nzp are related to the dealiasing and will be defined later.

Before calculating the nonlinear terms, the FFTs in both x and z direction have to be performed as mentioned before. Due to the data storage after `getpxz_z`, the FFTs can be performed in only z-direction. Thus it is necessary to transfer the data among different processors once more such that every processor can perform the FFTs in the x-direction.

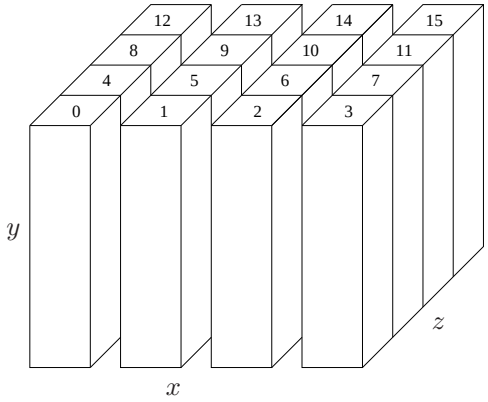

FIGURE 7. The configuration of the groups for the first transpose.

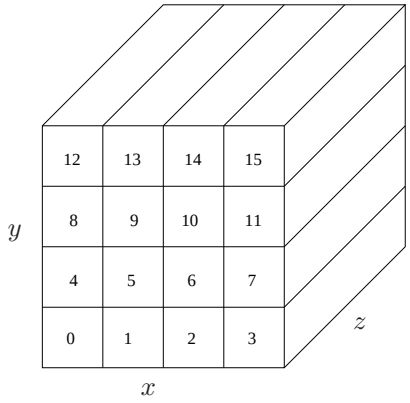

FIGURE 8. The data distribution after `getpxz_z`.

First, the processors are separated into *nprocx* groups and each group contains *nprocz* processors. The creation of groups is shown in Figure 7. Then the standard MPI command **MPI_ALLTOALL** is used to transpose the data within each group. This is done by calling the subroutine `getpxz_z`. The data storage configuration after the transpose is shown in Figure 8. For convenience only the first consecutive *nprocz* planes in the wall-normal direction are plotted. The layout of the other wall-parallel planes is just a repetition of the first *nprocz* planes. The creation of groups and the data storage for the second global data transpose are shown in Figures 9 and 10 and will be discussed later. Now, aliasing errors which are caused by representing higher wavenumber data at lower wavenumbers have to be considered. A detailed description can be found in e.g. Canuto *et al.* (1988). In order to eliminate the aliasing errors, the standard 3/2-rule is employed which means to expand the original grid and pad high-wavenumber part with zeros. The original grid, as shown in Figure 11 (a), is therefore expanded to a finer grid which has a dimension of $\frac{nx}{2}$ in the x-direction and nzp in the z-direction where $nzp = \frac{3}{2}nz$, see Figure 11 (b). If nzp is not divisible by $nprocz$, the dealiasing grid needs to be $(\frac{nzp}{nprocz} + \min(1, \mathrm{mod}(nzp, nprocz))) \times nprocz$, where the operation "min" is to take the minimum and "mod" is the modulo operation. Then part of the data denoted by the "slashed area" is moved to the upper part of the fine grid and the middle part is padded with zeros denoted by the $\bigcirc$. The so-called "oddball mode" is also set to zero which is denoted by the grided lines, in Figure 11. For more details about the oddball mode, refer to Chevalier et al. (2007). At the end of this step, each processor can perform the backward FFTs in the z-direction on the fine grid.

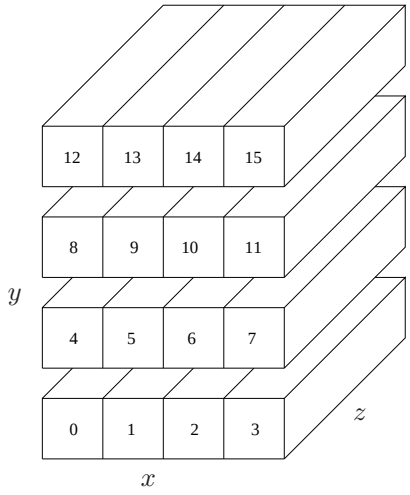

FIGURE 9. The configuration of the groups for the second transpose.

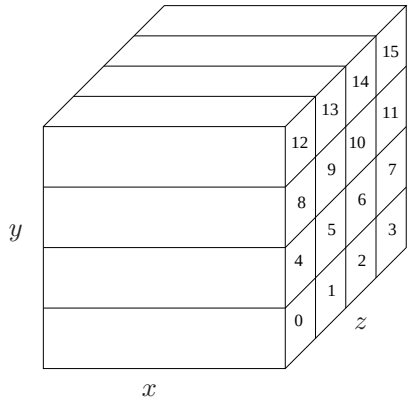

FIGURE 10. The data distribution after `getpxz_x`.

In a second step, *nprocz* new groups are created and each group contains *nprocx* processors. This is to prepare for the FFTs in the x-direction to be performed. The newly created groups are sketched in Figure 9. Then another transpose of the data in each group can be executed. This second data transpose is done by calling subroutine `getpxz_x`. After the data transpose, the data storage configuration on each processor is shown in Figure 10. The grid is expanded in the x-direction this time in order to account for the 3/2-rule and the dimension of the dealiasing grid is $\frac{nxp}{2}+1$ in the x-direction where $nxp = \frac{3}{2}nx$. In the spanwise direction, nzp are continued to be used. This grid is shown in Figure 11 (c). The additional grid point in streamwise direction is due to requirement of the FFT. For a complex to real FFT, two more points, i.e. two zeros for the imaginary parts, are added. One is for the zero frequency component and the other for the Nyquist frequency component. Since the real and imaginary parts are stored separately, this leads to the additional point in the x-direction. The right-hand part is padded with zeros and the oddball mode is also set to zero. Last, the FFTs in the x-direction on each processor are performed. After the FFTs, all the data is in physical space and the nonlinear terms can be calculated. Afterwards, all the data has to be transformed back to the spectral space to match the configuration shown in Figure 5. This will be exactly a reverse process of the steps mentioned above.

In the subroutine `linearbl`, the data is put onto xy-planes by calling the subroutine `getpxy`. As shown in Figure 12, each processor only calculates a portion of one xy-plane at each time, therefore the computation is carried out in parallel and there is no communication involved between any two processors as the same for 1D parallelisation. After the calculation, the data is put back to the main memory through subroutine `putpxy`, again without requiring any MPI communication.

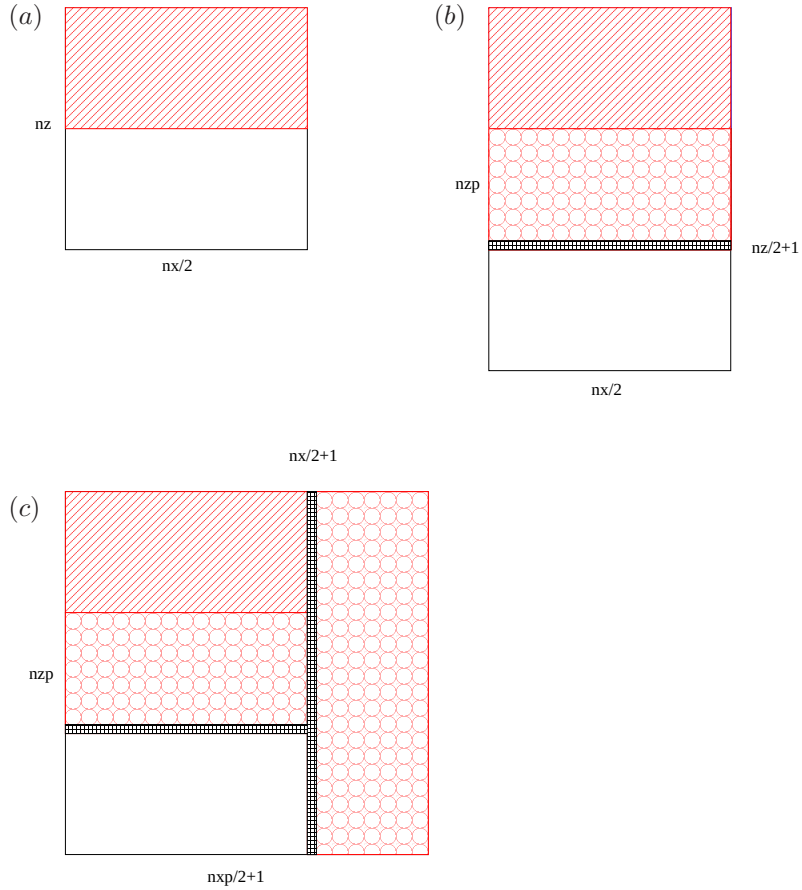

FIGURE 11. The dealiasing grid and the oddball location in a xz-plane. (a) Grid before dealiasing, (b) Grid after dealiasing in z, (c) Grid after dealiasing in z and x.

2.3. *Amount of communication*

2.3.1. *1D parallelisation*

The main communication between the processors is in the nonlinear part, i.e. subroutine `nonlinbl`. Consider in the following only the velocity field, i.e. without pressure nor scalar fields. Then for each call to `nonlinbl`, five variables (three velocity components and two components of the vorticity) are collected from the main memory by calling subroutine `getpxz` and three variables (three vorticity components) are put back to the main memory via the subroutine `putpxz` for the 1D parallelisation. Thus a total of eight variables have to be communicated which is independent of the implementation of the global communication. Here only the version of collective communication using standard

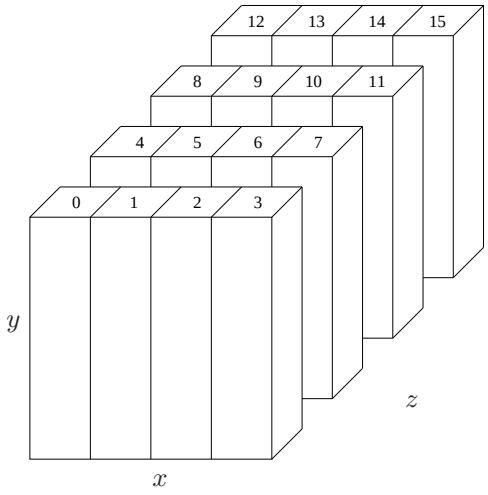

FIGURE 12. The data distribution in `linearbl`.

command **MPI_ALLTOALL** is discussed. For the hand-written version based on explicit point-to-point communication, more details can be found in Alvelius & Skote (2000). However, the amount of data to be communicated is roughly the same.

Each processor performs calculation on approximately $(\mathrm{int}(\frac{nyp}{nproc})+1)$ xz-planes. The data types of the message are the user-defined data types, i.e. $realg1$ and $realg2$. Both of them have a size of $memnx \times memnz$ or $\frac{nx}{2} \times \frac{nz}{nproc}$. The number of messages that one processor collects is

$$2 \times (nproc-1) \times (\mathrm{int}(\frac{nyp}{nproc})+1) \; . \tag{1}$$

Note that each processor collects data from all the other processors and both the real and imaginary part gives a factor of 2 for the total number of messages which has to be communicated. This gives that for one flow variable each processor needs to collect

$$(nproc-1) \times (\mathrm{int}(\frac{nyp}{nproc})+1) \times nx \times \frac{nz}{nproc} \tag{2}$$

real numbers from all the processors at each Runge-Kutta substep. Since each number has double precision, i.e. 8 bytes for each real number, the total amount of data that needs to be communicated for a single processor for all 8 variables and one iteration (Runge-Kutta substep) is

$$8 \times 8 \times (nproc-1) \times (\mathrm{int}(\frac{nyp}{nproc})+1) \times nx \times \frac{nz}{nproc} \tag{3}$$

bytes. The amount of data that each processor has to send at the same time is as large as the amount that has to be received.

2.3.2. *2D parallelisation*

For the 2D parallelisation, the situation is slightly different than that for the 1D case. As explained earlier, the data has to be transposed twice in order to perform the FFTs. For each call to `nonlinbl`, five variables (three velocity components and two vorticity components) are collected from the main memory with `getpxz_z` and later three variables (the evaluated non-linear terms) are put back to the main memory with `putpxz_z` within `nonlinbl`. Six variables (three velocity and three right-hand side components) are collected from the temporary storage via `getpxz_x` and only three variables (three vorticity components) are put back with `putpxz_x` to the temporary storage. In the 2D case, each processor performs calculations on approximately $(\mathrm{int}(\frac{nyp}{nprocz}) + 1)$ xz-planes. The data types used for the message are $realg1$ and $realg2$ in `getpxz_z` and `putpxz_z` while $realg3$ and $realg4$ in `getpxz_x` and `putpxz_x`. Both $realg1$ and $realg2$ have a size of $\frac{nx}{2nprocx} \times \frac{nz}{nprocz}$ and the size of $realg3$ and $realg4$ is $\frac{nx}{2nprocx} \times \frac{nzp}{nprocz}$. Following the same steps as for the 1D parallelisation, the number of messages needs to be communicated for the first and the second transpose are

$$2 \times (nprocz - 1) \times (\mathrm{int}(\frac{nyp}{nprocz}) + 1) \tag{4}$$

and

$$2 \times (nprocx - 1) \times (\mathrm{int}(\frac{nyp}{nprocz}) + 1) \tag{5}$$

respectively. The total amount of data which has to be collected for one processor for each Runge-Kutta substep and all 17 variables is

$$\begin{aligned} &8 \times (nprocz - 1) \times (\mathrm{int}(\frac{nyp}{nprocz}) + 1) \times (8 \times \frac{nx}{nprocx} \times \frac{nz}{nprocz}) + \\ &8 \times (nprocx - 1) \times (\mathrm{int}(\frac{nyp}{nprocz}) + 1) \times (9 \times \frac{nx}{nprocx} \times \frac{nzp}{nprocz}) \end{aligned} \tag{6}$$

bytes. Again the same amount of data has to be sent by each processor at the same time.

2.3.3. *Communication comparison*

In this section, the total amount of messages sent by each processor (including the messages it sends to itself) at each Runge-Kutta substep are compared for both 1D and 2D parallelisations with a fixed size for nx, nyp and nz. The results are plotted in Figure 13. For a fixed resolution, it is clear that the 2D parallelisation does involve more communication than the 1D parallelisation. Nevertheless, the overall performance of the 2D parallelisation is better. The main reason is that the processors are divided into groups and each processor only communicates within its own group and not globally. All the groups run in parallel and the influences due to the congestions from the one group to the other are small. Therefore, the total performance is better for the 2D parallelisation. The ratio between the messages sent by the 1D and 2D parallelisation is

also plotted in Figure 13. As the number of processors increases, the ratio decreases slowly for small number of processors. However, for a typical simulation case, this ratio is always larger than unity.

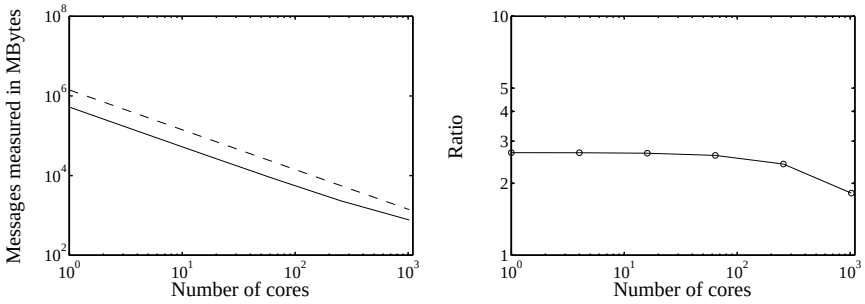

FIGURE 13. A comparison of the total amount of communication for the 1D and 2D parallelisation for a size of $2048 \times 2049 \times 2048$. *Left*: Messages that being sent for the two parallelisations, ——1D parallelisation, - - -2D parallelisation, *Right*: The ratio of the messages being sent for the two parallelisations.

3. Performance analysis

For the parallel computing, the maximum speed-up of a code can be obtained is

$$\text{speed-up} = \frac{1}{F + (1-F)/N} \tag{7}$$

where F is the fraction of a calculation that is sequential, i.e. the part that cannot benefit from parallelisation, and thus $(1-F)$ is the fraction that can be parallelised where N is the number of processors used for the calculation. This is usually referred as the Amdahl's law (Amdahl 1967). Ideally, if the whole code can run in parallel, a maximum of speed-up of N can be obtained, i.e. the so-called linear speed-up. However, a real application code always has some part which cannot be parallelised in practice. This will lead to a maximum speed-up by $\frac{1}{F}$ for large N. Therefore, a lot of effort is devoted to reducing F to a value as small as possible. Additionally, even the parallelisible parts of a code will usually not scale linearly, but rather at a reduced rate.

A benchmark for the parallelisation of **SIMSON** has been performed on a BlueGene/L machine manufactured by IBM. The building block of the BlueGene/L system is the compute card consisting of 1 node. On each node there are two processors (cores) with up to 1024 Mbytes of memory. Each processor is an embedded 32-bit PowerPC 440 with a clock frequency of 700 MHz. The system-on-chip design contains three interconnections: Gbit Ethernet, global tree (collective communication) and 3D Torus. Two execution modes are available for each node. One is the co-processor mode (CO), i.e. only one MPI

process per node with maximum 1024 Mbytes of memory per process. In this mode, one processor is dedicated to communication and the other to general processing. The other mode is the virtual-node mode (VN), i.e. two MPI processes per node with maximum 512 Mbytes of memory per process. In this case, each processors uses half of the resources and works as an independent processor. A detailed description about the BlueGene/L machine can be found in the online manual (Mullen-Schultz & Sosa 2007).

3.1. *Performance of the* ***MPI_ALLTOALL***

As the main communication pattern for the communication in the present code and also one of the most important collective communication used in scientific computing, it is necessary and crucial to understand how the **MPI_ALLTOALL** collective operation performs. Therefore, a performance test has been carried out and a performance model for **MPI_ALLTOALL** is developed.

During an **MPI_ALLTOALL** operation, each process holds $m \times n$ data, where n is the number of processes involved in the communication and m is the message size (measured in bytes) sent to or received from one other process. Following the linear point-to-point model, the communication time spent on one process is

$$T = (n-1) \times (\alpha + m \times \beta^{-1}) \tag{8}$$

where α is the start-up time, i.e. the latency between two processes, and β is the bandwidth of the link. Unfortunately, this model does not work so well when intensive communication happens as pointed out by Steffenel *et al.* (2007). Thus, network contention-aware communication models are suggested. However, due to the non-deterministic behaviour of the network contention, some authors suggested a few techniques to adapt the existing models, e.g. Clement *et al.* (1996) introduced the contention factor to correct the performance model. Bruck *et al.* (1997) came up with the similar ideas to use the slowdown factor. Recently, Steffenel *et al.* (2007) proposed a new model consisting of determining a contention ratio. For simplicity, the contention ratio is considered to be a constant and only depends on the network characteristics. Following the model by Steffenel *et al.* (2007), the performance model which is an extension of the linear point-to-point model reads

$$T = (n-1) \times (\alpha + \gamma \times m \times \beta^{-1}) \tag{9}$$

where γ is the contention ratio. If N is chosen to represent the total message that has to be sent by all the processes, m would be $\frac{N}{n^2}$. Then the equation (9) will read

$$T = (n-1) \times (\alpha + \gamma \times \frac{N}{n^2} \times \beta^{-1}) \ . \tag{10}$$

Using this performance model of **MPI_ALLTOALL**, a series of tests has been run on a BlueGene/L machine using both VN and CO mode. The total amount of the message to be sent is fixed, i.e. $N = 3072 \times 3072$, with the number of cores involved in the communication varying from 2 to 1024.

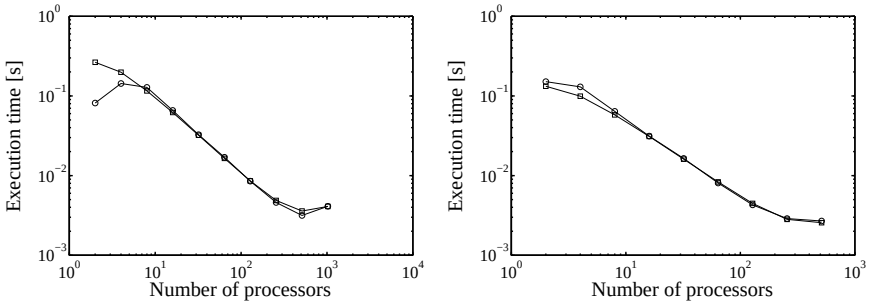

FIGURE 14. Performance of the **MPI_ALLTOALL** for VN and CO mode. ∘ Measurements, □ Model prediction. *Left*: VN mode with $\alpha = 3$ [μs], $\beta = 300$ [Mbytes/s] and $\gamma = 4.29$, *Right*: CO mode with $\alpha = 3$ [μs], $\beta = 300$ [Mbytes/s] and $\gamma = 2.14$.

The results of the execution time spent on one core are shown in Figure 14. As seen from the figure, the model predictions compare well with the measurements for number of cores larger than 4. The discrepancies for the measurements at low number of cores are partially due to the not fully contentioned network and also due to the non-linear affects when the messages sent by each process is sufficiently large. The latency α for both cases are on the order of 1 μs which is consistent with the theoretical value from the BlueGene/L manual. On the other hand, the bandwidth used for both cases are obtained from measurement of a point-to-point communication. The contention ratio for the CO mode is about twice as for the VN mode. The reason is due to the fact that for the VN mode case, both processors (cores) share one link (bus, port) within each node which leads to twice the contention ratio for each core.

3.2. *Code performance*

Two cases of different sizes are tested for both 1D and 2D parallelisations. The smaller case has the resolution of $1024 \times 129 \times 128$ (run1) while the resolution of the larger one is $512 \times 513 \times 512$ (run2). Only the velocity field, i.e. without pressure and scalar fields, is simulated for periodic channel flow, and the code has been run in virtual-node mode (VN). As mentioned before, most of the execution time is spent in the linear and nonlinear parts, i.e. in the subroutines `linearbl` and `nonlinbl`, and the main computational effort is the FFTs in `nonlinbl`. The speed-up plots shown later are thus only based on the execution times from these two subroutines. The execution time per time step, i.e. four Runge-Kutta substeps, is chosen to calculate the speed-up.

In Figure 15 the two parallelisations are compared for the smaller case (run1). Due to the requirement of the 2D parallelisation, i.e. that the processors need to be equally distributed along both wall-parallel directions, the first data point corresponds to 2 nodes or 4 processors. Clearly seen from the figure, the

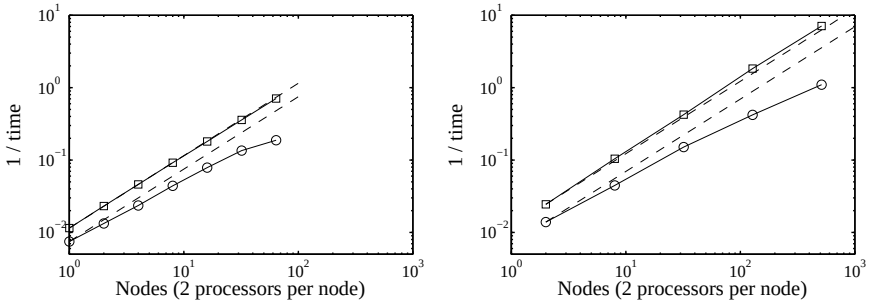

FIGURE 15. Performance of the two parallelisations for the Run1 (run1). - - -Linear speed-up, □ `linearbl`, ○ `nonlinbl`. *Left*: 1D parallelisation, *Right*: 2D parallelisation.

linear part has a linear behaviour, even a slightly super-linear behaviour for the 2D parallelisation. However, the speed-up curves of the nonlinear part for both parallelisations deviate from the linear speed-up curve further and further as more and more processors are used.

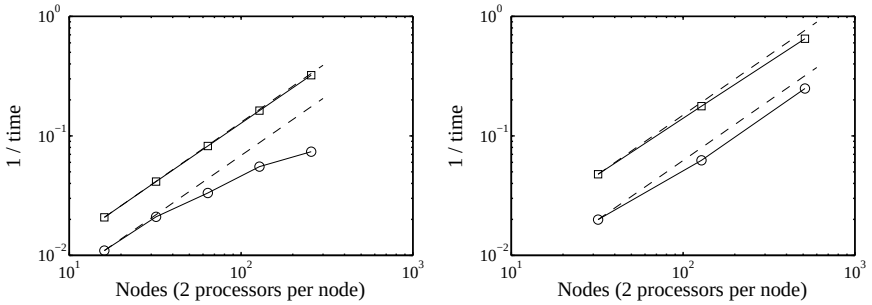

FIGURE 16. Performance of the two parallelisations for the Run2 (run2). - - -Linear speed-up, □ `linearbl`, ○ `nonlinbl`. *Left*: 1D parallelisation, *Right*: 2D parallelisation.

In Figure 16 the larger test case (run2) is shown for the two parallelisations. Note that due to the larger memory requirements, a minimum number of nodes of 16 has to be used for the 1D parallelisation and 32 for the 2D parallelisation. Similarly to the smaller case, the linear parts of both parallelisations still have linear performance. But for the nonlinear parts, a clear difference can be observed for the two parallelisations. As seen from the plots, the 1D parallelisation shows a similar behaviour as for the smaller case reaching a saturation of the performance at 256 node, and the 2D parallelisation has almost linear performance up to 512 nodes.

As known from the previous section, in the nonlinear part, i.e. subroutine `nonlinbl`, the speed-up curve will inherently not scale linearly with the

number of processors used since a global data transpose has to be performed. However, there is another important fact which leads to this suboptimal behaviour, i.e. the particular number of discretization points in the wall-normal direction. Since a Chebyshev representation in the wall-normal direction is used, the number of grid points in the y-direction is not divisible by the number of processors, i.e. $\frac{nyp}{nproc}$ for the 1D parallelisation or $\frac{nyp}{nprocz}$ for the 2D parallelisation is not an integer number. Therefore, for the last y-loop outside the subroutine `nonlinbl`, not all the processors are active. The last instance of the loop is not completely parallelised. If *nproc* or *nprocz* is of the same order of magnitude as *nyp*, this will have very large effect on the performance. This is what are observed from the 1D parallelisation. If *nproc* or *nprocz* is relatively small compared to *nyp*, the effect form this last y-loop is much smaller. This is clearly demonstrated by the 2D parallelisation. In general, for the 2D parallelisation, since *nprocz* is only the square root of *nproc*, the effect of the last y-loop should be smaller than the 1D parallelisation. However, if increasing the number of processors for the 2D parallelisation even more, the same problem will appear eventually.

To investigate the behaviour of subroutine `nonlinbl` in more detail, the total execution time of `nonlinbl` is split into two parts: one part only involves communication (t_{com}), the other part is the computation (t_{ser}), e.g. the FFTs. Hence the relation $t_{nonlinbl} = t_{com} + t_{ser}$ is obtained. Note that these times correspond to the wall-clock time on one processor, and that all processors are synchronised using appropriate barriers.

In Figure 17, the time for communication and computation in subroutine `nonlinbl` are compared for both parallelisations. As expected, for both parallelisations the speed-up curves for the communication part do have suboptimal behaviours, i.e. not scaling linearly. It is clear by comparing the computational part for the two parallelisations that the effect of the last y-loop has a smaller effect for the 2D parallelisation. Remember that the main computational effort is the FFTs which indicates that the time spent by the computation should be larger than that by the communication and this is also observable from the plots for the 1D parallelisation. Note that since $\frac{1}{time}$ is plotted, the lower the data point the large the execution time is. As the number of processors is increased, more and more communication will happen which means that t_{com} will take a larger and larger portion of the total time spent in `nonlinbl`. For the 2D parallelisation, there is even more communication happening, so the growth of t_{com} is even faster. As seen from the plots, t_{com} can become larger than t_{ser} even at small number of processors, e.g. 32 nodes (64 cores).

A summary of the execution time (measured in wall-clock time [s]) of one time step on one processor for both the small and the large runs is shown in Tables 3.2–3.2. Note that the numbers in the bracket are the corresponding percentage of the total execution time (t_{sum}).

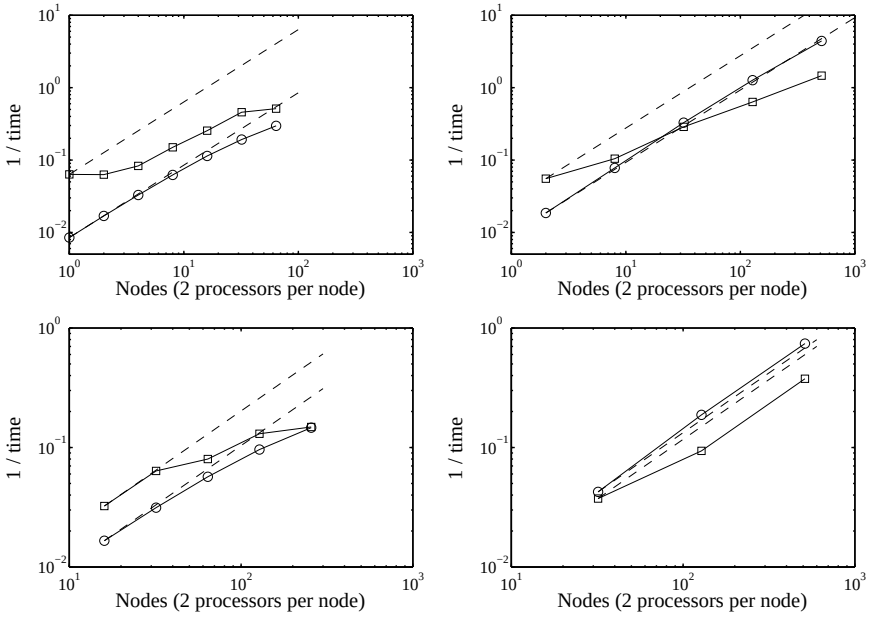

FIGURE 17. Performance of t_{com} and t_{ser} in `nonlinbl`. - - -Linear speed-up, □ t_{com}, ∘ t_{ser}. *Top*: Run1, *Bottom*: Run2. $Left$: 1D parallelisation, *Right*: 2D parallelisation.

	`linearbl`	`nonlinbl`			
nproc	$t_{linearbl}$	t_{ser}	t_{com}	$t_{nonlinbl}$	t_{sum}
1	147.5 (42.3%)	186.0 (53.4%)	15.0 (4.3%)	201.1 (57.7%)	348.6
2	87.0 (39.5%)	117.6 (53.4%)	15.8 (7.2%)	133.3 (60.5%)	220.4
4	43.2 (36.5%)	59.2 (50.0%)	15.9 (13.5%)	75.1 (63.5%)	118.3
8	21.7 (33.8%)	30.4 (47.4%)	12.0 (18.7%)	42.5 (66.1%)	64.2
16	10.9 (32.3%)	16.0 (47.7%)	6.7 (19.8%)	22.7 (67.5%)	33.7
32	5.5 (30.4%)	8.8 (48.1%)	3.9 (21.5%)	12.7 (69.6%)	18.3
64	2.8 (27.4%)	5.2 (51.1%)	2.2 (21.4%)	7.4 (72.5%)	10.2
128	1.4 (20.9%)	3.4 (50.0%)	2.0 (28.9%)	5.3 (78.9%)	6.8

TABLE 2. Execution time of the Run1 using the 1D parallelisation.

3.3. *Modelling*

To eliminate the effect of last y-loop on the performance, a factor k is multiplied with each sampled data from `nonlinbl`. This correction is just to help to develop the model of the whole performance of the code. Since the effect for the 2D parallelisation is much smaller than that for the 1D parallelisation, this correction is only done for the 1D parallelisation. The correction factor k is a

	`linearbl`	`nonlinbl`			
nproc	$t_{linearbl}$	t_{ser}	t_{com}	$t_{nonlinbl}$	t_{sum}
4	40.9 (36.2%)	53.8 (47.7%)	18.1 (16.0%)	71.9 (63.7%)	112.8
16	9.6 (29.9%)	12.8 (40.0%)	9.6 (29.8%)	22.4 (69.8%)	32.1
64	2.4 (26.3%)	3.0 (33.9%)	3.5 (38.5%)	6.6 (73.6%)	9.0
256	0.5 (18.6%)	0.8 (26.9%)	1.6 (53.7%)	2.4 (80.9%)	2.9
1024	0.1 (12.5%)	0.2 (20.0%)	0.7 (60.4%)	0.9 (80.5%)	1.1

TABLE 3. Execution time of the Run1 using the 2D parallelisation.

	`linearbl`	`nonlinbl`			
nproc	$t_{linearbl}$	t_{ser}	t_{com}	$t_{nonlinbl}$	t_{sum}
32	48.1 (34.5%)	60.3 (43.2%)	30.1 (22.2%)	91.2 (65.5%)	139.4
64	24.1 (33.6%)	31.8 (44.4%)	15.7 (21.9%)	47.6 (66.3%)	71.8
128	12.2 (28.8%)	17.6 (41.5%)	12.5 (29.5%)	30.1 (71.1%)	42.3
256	6.1 (25.3%)	10.4 (42.8%)	7.7 (31.5%)	18.1 (74.3%)	24.3
1024	3.1 (18.6%)	6.8 (40.8%)	6.7 (40.3%)	13.6 (81.1%)	16.7

TABLE 4. Execution time of the Run2 using the 1D parallelisation.

	`linearbl`	`nonlinbl`			
nproc	$t_{linearbl}$	t_{ser}	t_{com}	$t_{nonlinbl}$	t_{sum}
64	20.9 (29.4%)	23.5 (33.0%)	26.7 (37.5%)	50.2 (70.5%)	71.3
256	5.6 (26.0%)	5.3 (24.6%)	10.6 (49.2%)	16.0 (73.9%)	21.7
1024	1.5 (27.1%)	1.4 (23.8%)	2.7 (46.9%)	4.0 (70.7%)	5.7

TABLE 5. Execution time of the Run2 using the 2D parallelisation.

function of the number of processors and is defined as

$$k = \frac{nyp}{(\mathrm{int}(\frac{nyp}{nproc}) + 1) \times nproc} \ . \tag{11}$$

After the correction, the total time spent in subroutines `linearbl` and `nonlinbl` are shown in Figure 18 and the communication and computation parts within `nonlinbl` are shown in Figure 19, respectively. Except the communication part, all the other parts, i.e. `linearbl` and the computation part within `nonlinbl`, have linear speed-up performance. And this is also true for the 2D parallelisation, however without requiring a correction for the last y-loop.

In order to roughly estimate the performance on BlueGene/L without running a simulation, a performance model has been developed for the code of both 1D and 2D parallelisations. Known from the previous section that after eliminating the effects from the last y-loop, only the communication part does not have a linear speed-up behaviour. Therefore this part needs to be modelled. In the model, only the latency, bandwidth and contention ratio are considered to be the most important factors and all the other influences are neglected,

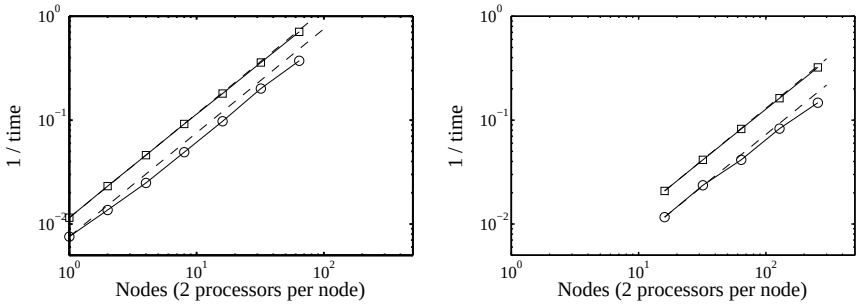

FIGURE 18. Performance of the 1D parallelisation after correction for the 1D parallelisation. - - -Linear speed-up, □ `linearbl`, ∘ `nonlinbl`. *Left*: Run1, *Right*: Run2.

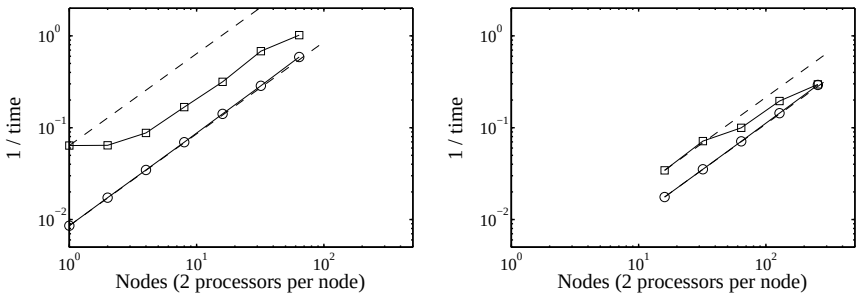

FIGURE 19. Performance of t_{com} and t_{ser} in `nonlinbl` after correction for the 1D parallelisation. - - -Linear speed-up, □ t_{com}, ∘ t_{ser}. *Left*: Run1, *Right*: Run2.

e.g. the topology of the system, the distance between the two communicating processors, etc.

For the **MPI_ALLTOALL** version of the 1D parallelisation, the model of the execution time of communication t_{com} for one Runge-Kutta substep and one variable can be built up as the following steps: First, each processor performs calculation on approximately $(\mathrm{int}(\frac{nyp}{nproc}) + 1)$ xz-planes. Second, for each xz-plane each processor needs to collect

$$2 \times (nproc - 1) \times \frac{nx}{2} \times \frac{nz}{nproc}$$

messages (real numbers) from all the other processors for one variable and Runge-Kutta substep. The associated count for latency of one processor for collecting all these data is

$$2 \times (nproc - 1)$$

times. Note that the factor of 2 is from the real and imaginary part of the data needs to be collected. The execution time of communication t_{com} of one

processor for one time step, i.e. 4 Runge-Kutta substeps, and all the 8 variables is approximately given by

$$t_{com} = 4\times 8\times 2\times(\mathrm{int}(\frac{nyp}{nproc})+1)\cdot(nproc-1)\cdot(\alpha+8\cdot\gamma\cdot\frac{nx}{2}\cdot\frac{nz}{nproc}\cdot\beta^{-1}) \quad (12)$$

where α is the latency $[s]$, β is the bandwidth $[bytes/s]$ and γ is the contention ratio. The number of messages has been multiplied by a factor of 8 to convert to bytes, since double precision is used, i.e. 8 bytes for each real number. The corresponding model for the hand-written version of the 1D parallelisation is also given here as,

$$t_{com} = 4\times 8\times 2\times\frac{nyp}{nproc}\cdot(nproc-1)\cdot(\alpha+8\cdot\gamma\cdot\frac{nx}{2}\cdot\frac{nz}{nproc}\cdot\beta^{-1})\ . \quad (13)$$

There is only very little difference when comparing these two models given by equations (12) and (13). Following the same steps, a model of the execution time of the communication t_{com} for the 2D parallelisation can be developed. For one time step and all variables, the execution time of communication t_{com} is approximately given by

$$t_{com} = 4\times 17\times 2\times(\mathrm{int}(\frac{nyp}{nprocz})+1)\cdot(nprocz-1)\cdot(\alpha+8\cdot\gamma$$
$$\cdot(\frac{8}{17}\cdot\frac{nx}{2\cdot nprocx}\cdot\frac{nz}{nprocz}+\frac{9}{17}\cdot\frac{nx}{2\cdot nprocx}\cdot\frac{nzp}{nprocz})\cdot\beta^{-1})\ . \quad (14)$$

Once having the model for the communication part, the model for the total execution time can easily be developed since all the other parts have a linear behaviour after some correction. As already mentioned before, the sum of the execution time from subroutines `linearbl` and `nonlinbl` is used to represent the total time for the code. Hence the total execution time (t^{1D}_{total}) for the 1D parallelisation can be expressed as

$$t^{1D}_{total} = t_{linearbl} + t_{nonlinbl} = t_{linearbl} + t_{com} + t_{ser}$$

and $t_{linearbl}$, t_{ser}, t_{com} are calculated as

$$\begin{aligned} t_{linearbl} &= t^1_{linearbl}\cdot\frac{nproc^1}{nproc} \\ t_{ser} &= \frac{t^1_{ser}}{k}\cdot\frac{nproc^1}{nproc} \\ t_{com} &= \frac{t^*_{com}}{k} \end{aligned}$$

where all the terms with a superscript 1 are the first available measurement data from a simulation, because it is not always possible to get the data from a serial version of the code, e.g. due to memory requirements. k is the correction factor defined in equation (11) and t^*_{com} is the value calculated from equation (12) or (13) depending on which version of the global communication is used. The total execution time (t^{2D}_{total}) for the 2D parallelisation can be expressed in a similar way as

$$t^{2D}_{total} = t_{linearbl} + t_{nonlinbl} = t_{linearbl} + t_{com} + t_{ser}$$

and $t_{linearbl}$, t_{ser}, t_{com} are given as

$$\begin{aligned} t_{linearbl} &= t^1_{linearbl} \cdot \frac{nproc^1}{nproc} \\ t_{ser} &= t^1_{ser} \cdot \frac{nproc^1}{nproc} \\ t_{com} &= t^*_{com} \end{aligned}$$

where again all the terms with a superscript 1 are the first available measurement data from a simulation. t^*_{com} is the value calculated from equation (14). Remember that the correction for the last y-loop in case of the 2D parallelisation is not applied, so there is no correction factor in the model.

3.4. *Comparison to the measurements*

The predicted total execution time as well as the one from the simulation measurements for one time step of both parallelisations are shown in Figures 20 and 21. In general, both models predict the behaviours of the code for all the cases very well.

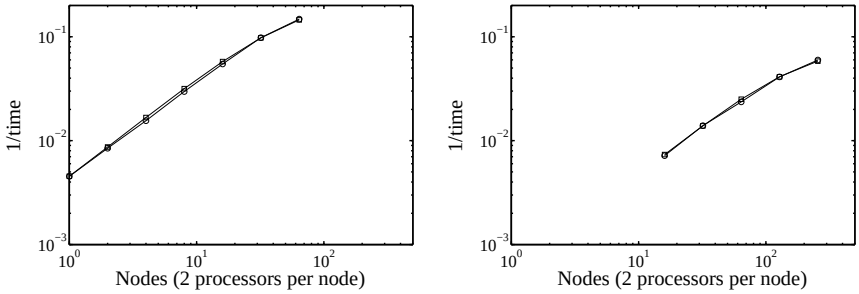

FIGURE 20. Model prediction versus the measurements for the 1D parallelisation. □ Model prediction, ∘ Measurements. *Left*: Run1 with $\alpha = 40$ [μs], $\beta = 300$ [Mbytes/s] and $\gamma = 4.29$, *Right*: Run2 with $\alpha = 80$ [μs], $\beta = 300$ [Mbytes/s] and $\gamma = 4.29$.

Note that the values of the bandwidth used in the model is obtained from a point-to-point communication test and is 300 [Mbytes/s]. The theoretical value given by the specification of the BlueGene/L machine for global tree interconnection (used for the collective communication) is about 350 [Mbytes/s]. The latency used in the model is much larger than the theoretical value which is usually less than 10 μs, this might be due to the models themselves which do not capture some non-linear effects. However, as long as large messages are sent, the influence of the latency is always small enough to be neglected.

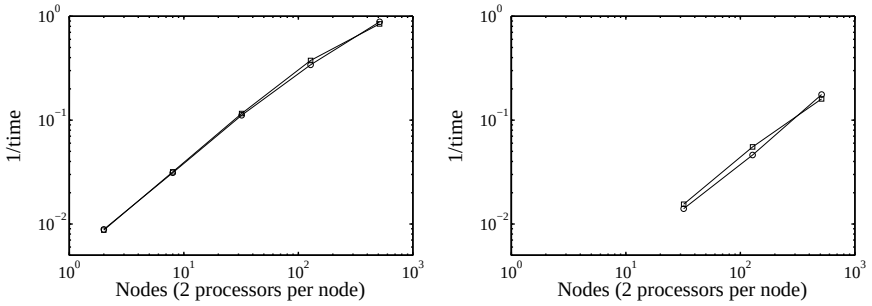

FIGURE 21. Model prediction versus the measurements for the 2D parallelisation. □ Model prediction, ∘ Measurements. *Left*: Run1 with $\alpha = 30$ [μs], $\beta = 300$ [Mbytes/s] and $\gamma = 4.29$, *Right*: Run2 with $\alpha = 30$ [μs], $\beta = 300$ [Mbytes/s] and $\gamma = 4.29$.

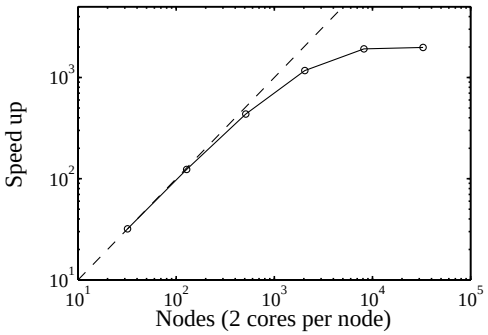

FIGURE 22. Model prediction of the Run2 (run2) for the 2D parallelisation. - - - Linear speed-up, ∘ Model prediction with $\alpha = 5$ [μs], $\beta = 300$ [Mbytes/s] and $\gamma = 4.29$.

3.5. *Limiting behaviour*

The model for the 2D parallelisation is used to predict the limiting performance for large processor counts and the plot is shown in Figure 22. If a large number of processors is used, the message size becomes comparably small. The influence of the latency is then much more important. Therefore, in the model, the value for the latency is chosen from the machine specifications. As mentioned before, the effect from the last y-loop will become significant once the number of processors is large enough. This is clearly seen in the figure. The predicted maximum speed-up is about 1000 (on 2048 nodes), 2000 (on 8192 nodes) and 2000 (on 32768 nodes). In practice, 8192 nodes might be the upper limit.

4. Conclusions

An efficient pseudo-spectral code (**SIMSON**) for solving the incompressible Navier–Stokes equations in channel and boundary-layer geometry has been developed during the last years at KTH Mechanics with the parallelisation only in the spanwise direction. Due to the limitation of this parallelisation approach, the total number of processors that can be used is at most the number of spanwise grid points, i.e. on the order of 256. This is definitely not suitable for the massively parallel super-computers which are getting more and more common at computer centres. Therefore, a 2D parallelisation has been implemented. This gives us the possibility to run simulations with more than 1000 cores (processors).

By looking into the details of the performance pertaining to different parts of the code, the suboptimal performance is due to the fact that for the last y-loop the code is not fully parallelised, i.e. some processors are idling. This problem cannot be eliminated completely due to the algorithm used now, but the effect of the problem can be reduced to some extent. Nevertheless, the code scales efficiently with the number of processors and therefore a high performance can be achieved. For the 2D parallelisation, the total amount of communication is larger than that in the 1D case, but due to parallel disjunct groups among processors, the overall performance is even better. For a large test case, a speed-up of about 130 (on 256 nodes) and 400 (on 512 nodes) for the 1D and 2D parallelisation respectively can be obtained.

Associated performance models for both parallelisations are developed and they predict the behaviours of the code reasonably well. The only part which needs modelling is the communication part, all the other parts have inherent linear behaviour after some simple modification. Benchmarks have been performed on a BlueGene/L machine with up to 1024 nodes.

Acknowledgements

The computer time was provided by the Centre for Parallel Computers (PDC) at the Royal Institute of Technology (KTH) and the National Supercomputer Centre in Sweden (NSC) at Linköping University. Discussions with Nils Smeds (IBM), Ulf Andersson (PDC) and Torgny Faxén (NSC) are gratefully acknowledged.

References

Alvelius, K. & Skote, M. 2000 The performance of a spectral simulation code for turbulence on parallel computers with distributed memory. *Tech. Rep* TRITA-MEK 2000:17. KTH Mechanics, Stockholm, Sweden.

Amdahl, G. 1967 Validity of the single processor approach to achieving large-scale computing capabilities. In *AFIPS spring joint computer conference, Atlantic City, N.J., U.S.A.*, pp. 483–485. AFIPS Press, Reston, V.A., U.S.A.

Bruck, J., Ho, C.-T., Upfal, E., Kipnis, S. & Weathersby, D. 1997 Efficient algorithms for All_to_All communications in multiport message–passing systems. *IEEE Trans. Parallel Distrib. Syst.* **8** (11), 1143–1156.

Canuto, C., Hussaini, M. Y., Quarteroni, A. & Zang, T. A. 1988 *Spectral Methods in Fluid Dynamics*. Springer, Berlin, Germany.

Chevalier, M., Schlatter, P., Lundbladh, A. & Henningson, D. S. 2007*a* A pseudo-spectral solver for incompressible boundary layer flows. *Tech. Rep* TRITA-MEK 2007:07. KTH Mechanics, Stockholm, Sweden.

Chevalier, M., Schlatter, P., Lundbladh, A. & Henningson, D. S. 2007*b* A pseudo-spectral solver for incompressible boundary layer flows. *Tech. Rep* TRITA-MEK 2007:07. Royal Institute of Technology, Stockholm.

Clement, M. J., Steed, M. R. & Crandall, P. E. 1996 Network performance modelling for PVM clusters. In *Proceedings of the 1996 ACM/IEEE conference on supercomputing*. IEEE Computer Society, Washington, D.C., U.S.A.

Lundbladh, A., Berlin, S., Skote, M., Hildings, C., Choi, J., Kim, J. & Henningson, D. S. 1999 An efficient spectral method for simulation of incompressible flow over a flat plate. *Tech. Rep* TRITA-MEK 1999:11. KTH Mechanics, Stockholm, Sweden.

Lundbladh, A., Henningson, D. S. & Johansson, A. V. 1992 An efficient spectral integration method for the solution of the navier–stokes equations. *Tech. Rep* FFA-TN 1992-28. Aeronautical Research Institute of Sweden, Bromma, Sweden.

Moin, P. & Mahesh, K. 1998 Direct numerical simulation: A tool in turbulence research. *Ann. Rev. Fluid Mech.* **30**, 539–578.

Mullen-Schultz, G. L. & Sosa, C. 2007 *IBM System Blue Gene Solution: Application Development*. `http://www.redbooks.ibm.com`.

Nordström, J., Nordin, N. & Henningson, D. S. 1999 The fringe region technique and the Fourier method used in the Direct Numerical Simulation of spatially evolving viscous flows. *SIAM J. Sci. Comp.* **20** (4), 1365–1393.

Sagaut, P. 2005 *Large Eddy Simulation for Incompressible Flows, An Introduction*, 3rd edn. Springer, Berlin, Germany.

Steffenel, L. A., Martinasso, M. & Trystram, D. 2007 Assessing contention effects on mpi_alltoall communications. In *Advances in Grid and Pervasive Computing* (ed. C. Cérin & K.-C. Li), *Lecture Notes in Computer Science*, vol. 4459, pp. 424–435. Springer-Verlag, Berlin, Germany.

Paper 2

2

Turbulent Boundary Layers up to $Re_\theta = 2500$ studied through simulation and experiment

By Philipp Schlatter, Ramis Örlü, Qiang Li, Geert Brethouwer, Jens H. M. Fransson, Arne V. Johansson, P. Henrik Alfredsson & Dan S. Henningson

Linné Flow Centre, KTH Mechanics
SE-100 44 Stockholm, Sweden

Phys. Fluids **21** 051702

Direct numerical simulations (DNS) and experiments of a spatially developing zero-pressure-gradient turbulent boundary layer are presented up to Reynolds number $Re_\theta = 2500$, based on momentum thickness θ and free-stream velocity. For the first time direct comparisons of DNS and experiments of turbulent boundary layers at the same (computationally high and experimentally low) Re_θ are given, showing excellent agreement in skin friction, mean velocity and turbulent fluctuations. These results allow for a substantial reduction of the uncertainty of boundary-layer data, and cross-validate the numerical setup and experimental technique. The additional insight into the flow provided by DNS clearly shows large-scale turbulent structures, which scale in outer units growing with Re_θ, spanning the whole boundary-layer height.

The study and understanding of the turbulent flow close to solid walls is a major topic in today's research in fluid dynamics. Although in nature or technical applications the surfaces are usually curved, possibly rough and the mean flow is seldomly exactly two-dimensional, the spatially developing, zero-pressure gradient turbulent boundary layer on a smooth, flat plate is an important canonical flow case for theoretical, numerical as well as experimental studies. In recent years, particularly careful experiments have been conducted. For instance, Österlund *et al.* Österlund *et al.* (2000) performed extensive measurements of mean quantities in the MTL (minimum turbulence level) wind tunnel at KTH Stockholm using hot-wire anemometry and oil-film interferometry for Reynolds numbers Re_θ (based on momentum thickness θ and free-stream velocity U_∞) ranging from 2530 to 27300, with five measurement positions below $Re_\theta = 6000$. Recall that Re_θ provides a measure of the streamwise position under consideration.

Direct numerical simulation (DNS) of turbulent flows relies on numerically resolving all relevant scales of motion. As the Reynolds number is getting larger the scale separation between the large and smallest scales is increasing considerably, limiting the Reynolds number attainable in DNS to low values compared

to experiments. As opposed to turbulent channel Hoyas & Jiménez (2006) and pipe flow Wu & Moin (2008), only few numerical results from direct numerical simulations (DNS) of turbulent boundary layers have been performed for medium or high (computational) Reynolds numbers. The main reason is the extreme cost of spatial DNS due to the long and consequently wide and high domains required, and the loss of one homogeneous direction. Spalart's simulations Spalart (1988) using an innovative spatio-temporal approach provided valuable data at $Re_\theta = 300, 670, 1410$, which have become a standard reference for numerical boundary-layer data. Komminaho and Skote Komminaho and Skote (2002) performed a spatial DNS up to $Re_\theta = 700$. The highest Reynolds number reached in DNS to date is the data reported by Ferrante and Elghobashi Ferrante & Elghobashi (2005) at $Re_\theta = 2900$, however obtained in a comparably short computational domain in which the turbulence, in particular the large-scale structures, may not be fully developed. Either the computational approaches were too different to the experiments or the Reynolds numbers were too low to make possible a robust comparison between all those simulations and experiments.

For turbulent boundary layers, the Reynolds number $Re_\theta \approx 2500$ has to be considered at present high from a DNS point of view. On the other hand, a high-quality boundary layer can be hard to establish and accurately measure at such Re_θ, since low Reynolds-number boundary-layer experiments need to be carried out at low velocities and for small distances from the leading edge. In the case of hot-wire measurements the need for accurate calibration at low velocities is needed especially for the near-wall measurements, whereas the choice of tripping may affect the onset of transition to turbulence. The latter will affect the structure of the turbulence mainly in the outer part, leading to influences in the turbulent statistics. Near the leading edge a pressure gradient is unavoidable, but can be reduced to nearly zero by adjusting the geometry of the set-up. Turbulent boundary-layer data available in the literature have usually been taken in a range of Re_θ by varying the free-stream velocity. The pressure gradient has often been tuned for one specific case, since readjustment of the pressure gradient is usually time-consuming and therefore not realized in many experiments. This means that some of the data available in the literature are not taken in the optimal configuration for the Re_θ in question.

Due to the difficulty of both DNS and experiments at Reynolds numbers Re_θ on the order of a few thousand, there is a comparably large spread of the existing data in the literature, both for integral, mean and fluctuating turbulent quantities, see *e.g.* Ref. Honkan & Andreopoulos (1997). There is thus a need for accurate and reliable DNS data of spatially developing turbulent boundary layers with Re_θ to be compared to high-quality experimental results. To this end, the inflow in the numerical simulation should be positioned far enough upstream, *i.e.* comparable to where natural transition occurs, to ensure that the flow reaches a fully developed, undisturbed equilibrium state further downstream.

The present paper reports a combined experimental and numerical study of zero-pressure-gradient turbulent boundary layers, aiming to provide a well-validated data set pertaining to the dynamics of the mean and fluctuating turbulent quantities as a function of the downstream distance. Both the experiments and simulations are performed with well-established and reliable methods. In addition, by considering the same generic flow case both experimentally and numerically, the sensitivity of the results to the respective method limitations, *e.g.* surface roughness, tripping technique, pressure gradients and boundary conditions *etc.*, can be examined.

The simulations are performed using a fully spectral method to solve the three-dimensional, time-dependent, incompressible Navier-Stokes equations Chevalier *et al.* (2007). In the wall-parallel directions, Fourier series with dealiasing are used whereas the wall-normal direction is discretized with Chebyshev polynomials. Time is advanced with a standard mixed Crank-Nicolson/Runge-Kutta scheme. Periodic boundary conditions in the streamwise direction are combined with a spatially developing boundary layer by adding a "fringe region" at the end of the domain. In this region, the outflowing fluid is forced via a volume force to the laminar inflowing Blasius boundary-layer profile, located at $Re_{\delta_0^*} = 450$ based on the inflow displacement thickness δ_0^*. A low-amplitude trip force acting in the wall-normal direction is used to cause rapid laminar-turbulent transition shortly downstream of the inlet. The chosen spectral method provides excellent accuracy and dispersion properties as compared to low-order discretizations.

The computational domain is $x_L \times y_L \times z_L = 3000\delta_0^* \times 100\delta_0^* \times 120\delta_0^*$ with $3072 \times 301 \times 256$ spectral collocation points in the streamwise, wall-normal and spanwise directions, respectively. The height and width of the computational domain are chosen to be at least twice the largest boundary-layer thickness, which reaches $\delta_{99} \approx 45\delta_0^*$ at $Re_\theta = 2500$. The grid points are non-equidistantly distributed in the wall-normal direction, with at least 15 collocation points within the region $y^+ < 10$. The grid resolution in viscous units is then $\Delta x^+ \times \Delta y^+_{\max} \times \Delta z^+ = 17.9 \times 8.6 \times 9.6$. The streamwise and spanwise resolution is about a factor 1.5 lower than in the channel-flow study by Hoyas and Jiménez Hoyas & Jiménez (2006), however, to ensure adequacy of the chosen grid, we also performed a resolution study based on the same box dimensions, but an increased number of grid points as $4096 \times 385 \times 480$ showing only insignificant differences regarding the results. The statistics are sampled over $\Delta t^+ \approx 24,000$ viscous time units, or 30 in units of δ_{99}/U_τ at $Re_\theta = 2500$. Owing to the high computational cost of the simulations, the numerical code is fully parallelized running on $\mathcal{O}(1000)$ processors.

The turbulent boundary-layer measurements were performed in the MTL wind tunnel on a 7 m long flat plate at x=1.6 m from the leading edge, where the ceiling of the tunnel was adjusted for each measurement run to obtain zero-pressure-gradient conditions. The set-up is similar to that of Österlund Österlund (1999). The free-stream velocity was 12.0 m/s and the streamwise

velocity component was measured by means of hot-wire anemometry using a single wire probe. The sensor length was 0.50 mm, corresponding to about 15 viscous length units. According to Ref. Johansson & Alfredsson (1983) this is sufficiently small in order not to observe effects of spatial averaging on the measured fluctuation levels in the near-wall region of wall-bounded flows. A three-dimensional deterministic surface roughness in combination with sandpaper was used to trip the boundary layer in order to obtain a fixed transition point. The skin friction was measured directly and independent from the hot-wire measurements using oil-film interferometry Rüedi *et al.* (2003).

The focus of the results presented here is on demonstrating averaged quantities, *i.e.* mean velocities and pressure and the fluctuations around that mean value. The considered case consists of a statistically two-dimensional boundary layer evolving in x and y, statistically homogeneous in the spanwise direction z and stationary in time t. The Reynolds decomposition

$$u = \langle u \rangle + u' = U + u' \tag{1}$$

is used, the brackets indicating the average in z and t. Based on the mean velocity profile $U(x, y)$ the shear stress at the wall is obtained as $\tau_w(x) = \mu(\mathrm{d}U/\mathrm{d}y)|_{y=0}$. Following the classical theory of turbulent boundary layers (see *e.g.* Ref. Schlichting (1987)), the friction velocity $U_\tau \equiv \sqrt{\tau_w/\rho}$ provides the relevant velocity scale throughout the boundary layer, whereas the viscous length scale $\ell_\star \equiv \nu/U_\tau$ is the characteristic length at least close to the wall. The scaled quantities in wall scaling are thus written as, *e.g.*, $U^+ = U/U_\tau$ and $y^+ = y/\ell_\star$.

In both the simulation and the experiment, the initially laminar boundary layer is tripped at approximately the same distance from the leading edge in terms of Re_θ. Further downstream of the tripping location, fully developed turbulence is established in which the boundary layer reaches an equilibrium state with the local production and dissipation of turbulent kinetic energy balancing each other. In the simulations, the extent of the self-similar region downstream of the tripping can be estimated by considering the von Kármán integral equation relating the local skin friction to the growth of the momentum thickness θ. Based on this argument, the useful region in the simulation may be defined as ranging from $Re_\theta = 550$ to 2500, corresponding to 75% of the total computational domain. The peak skin-friction Reynolds number $Re_\tau = U_\tau \delta/\nu$ with δ being the 99%-boundary-layer thickness is approximately 900 at $Re_\theta = 2500$.

Characteristic mean quantities of the turbulent boundary layer up to $Re_\theta = 2500$ are shown in Fig. 1. The skin friction is shown as the friction velocity scaled by the free-stream velocity, *i.e.* $U_\tau/U_\infty = \sqrt{c_f/2}$. Surprisingly, the simple correlation $c_f = 0.024 Re_\theta^{(-1/4)}$ Kays and Crawford (1993) provides an accurate fit to the DNS data for the range of Reynolds numbers considered. The agreement with the new experimental measurement point at $Re_\theta = 2500$ is very good. Recall that, experimentally the skin friction is obtained using

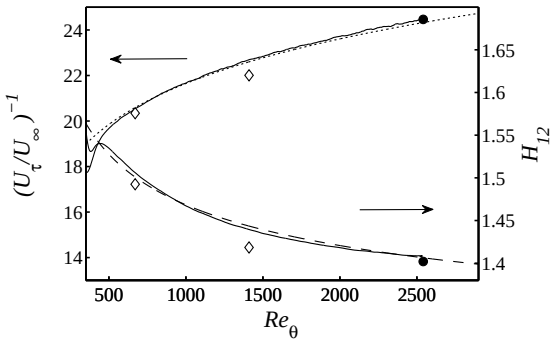

FIGURE 1. Skin friction $U_\tau/U_\infty = \sqrt{c_f/2}$ and shape factor H_{12} as a function of Re_θ. ——present DNS, • present experimental measurements. ◇ DNS by Spalart Spalart (1988). ····· $c_f = 0.024 Re_\theta^{(-1/4)}$ Kays and Crawford (1993), – – –correlation for H_{12} based on the composite profile suggested by Monkewitz *et al.* Monkewitz *et al.* (2007).

the oil-film technique Rüedi *et al.* (2003) independently of the velocity measurements. The shape factor $H_{12} = \delta^*/\theta$, *i.e.* the ratio of displacement to momentum thickness, is also shown; this quantity provides a useful way of characterizing the development state of the boundary layer. It turns out that H_{12} is a sensitive indicator which might be used as a scalar estimate of the quality of the boundary-layer data at a given Re_θ. The agreement with both the new measurements and the shape factor based on the composite velocity profile developed by Monkewitz *et al.* Monkewitz *et al.* (2007) is again satisfactory. Note that the coefficients in the composite profile have been calibrated for experimental boundary layers at higher Re_θ than the present one.

For comparison, the data points of the DNS by Spalart Spalart (1988) are also shown in Fig. 1. The skin friction is overpredicted by approximately 5% at the highest $Re_\theta = 1410$, whereas the shape factor is lower than the data obtained from both the composite profile and the present DNS. This might be a residual effect of the spatio-temporal approach employed for the simulation.

Profiles of the mean velocity scaled by viscous units $U^+(y^+)$ obtained from both the present DNS and experiments are shown in Fig. 2. The similarity at the highest Reynolds number shown, $Re_\theta = 2500$, is excellent. However, there is a discrepancy between the present simulation data and that of Spalart at $Re_\theta = 1410$, probably due to a suspected lower actual Re_θ in the latter simulation. In the wake region and the free stream, Spalart's results agree better with the present data at $Re_\theta = 1000$. In the near-wall region, all data collapse nicely on the linear relation $U^+ = y^+$ according to the asymptotic expansion for the viscous sublayer. The von Kármán coefficient κ used to indicate the logarithmic region $(1/\kappa)\log y^+ + B$ is chosen as $\kappa = 0.41$ which seems to best fit the data at this Re_θ. Inspection of the log-law indicator

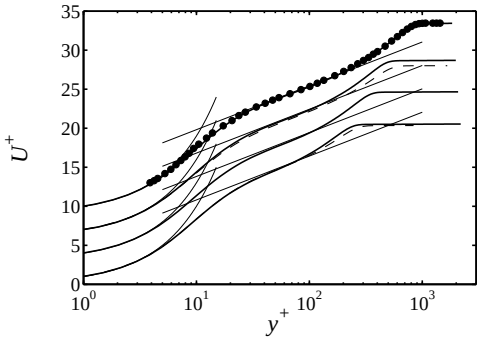

FIGURE 2. Mean velocity profile U^+ in viscous units for ——present DNS at $Re_\theta = 671, 1000, 1412, 2512$, • present measurements at $Re_\theta = 2541$. – – –DNS by Spalart Spalart (1988) at $Re_\theta = 670, 1410$. The profiles are shifted by $U^+ = 3$ along the ordinate for increasing Re_θ. The linear and logarithmic regions are indicated by a thin line, using $1/\kappa \log y^+ + B$ with $\kappa = 0.41$ and $B = 5.2$.

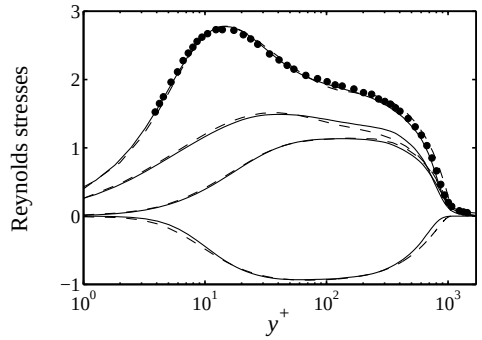

FIGURE 3. Turbulent fluctuations $u^+_{\rm rms}$, $w^+_{\rm rms}$, $v^+_{\rm rms}$ and shear stress $\langle u'v' \rangle^+$ (from top). ——present DNS at $Re_\theta = 2512$, • experiments at $Re_\theta = 2541$. – – –Correlations based on the attached-eddy hypothesis Marusic & Kunkel (2003); Kunkel & Marusic (2006); Perry *et al.* (2002).

function $\Xi = y^+(\mathrm{d}U^+/\mathrm{d}y^+)$ shows that the current DNS velocity profile closely follows the composite profile proposed in Ref. Monkewitz *et al.* (2007) up to $y^+ = 100$. For a boundary layer at $Re_\theta = 2500$, this wall-normal position can approximately be considered as the beginning of the wake region, in which the mean-flow gradient quickly rises to $\Xi \approx 5.2$ at $y^+ \approx 600$. The minimum of Ξ is reached at $y^+ \approx 70$ with a value of $1/\Xi \approx 0.428$ in good agreement with Ref. Monkewitz *et al.* (2007).

The velocity fluctuations, *e.g.* $u_{\rm rms} = \sqrt{\langle u'u' \rangle}$, and the Reynolds shear stress are depicted in Fig. 3 in wall scaling, and compared to the formulations

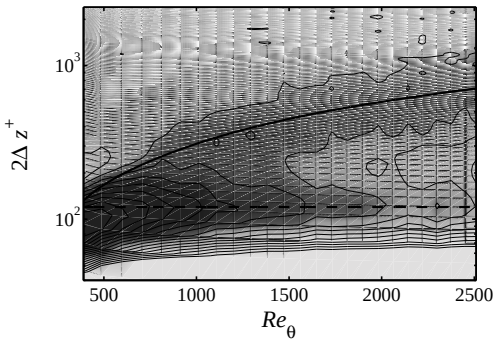

FIGURE 4. Spanwise two-point correlation $R_{\tau\tau}$ of the wall-shear stress τ_w computed from the present DNS. The spanwise axis is scaled by the displacement $2\Delta z^+$ in order to directly show the spanwise pattern spacing. ——— corresponds to $0.85\delta_{99}$, - - - corresponds to $120\ell_\star$. Shades range from dark ($R_{\tau\tau} \leq -0.06$) to light ($R_{\tau\tau} \geq 0.06$) ; contour lines go from -0.15 to 0.15 with spacing 0.02.

derived from the attached-eddy hypothesis by Marusic and Kunkel Marusic & Kunkel (2003); Kunkel & Marusic (2006); Perry *et al.* (2002). The agreement between DNS and the experimental data for the streamwise component is very good throughout the boundary layer. Higher-order statistics (skewness and flatness, not shown) of the streamwise fluctuations u' also show good agreement at all positions. Concerning the other velocity fluctuations and the shear stresses, the predictions from the attached-eddy hypothesis describe the present DNS data accurately.

As a side note, the pressure fluctuations close to the wall obtained from DNS (not shown) seem to scale best with a mixed scaling, yielding $p_{w,\mathrm{rms}}/(U_\tau \cdot U_\infty) \approx 0.112$. In pure inner scaling, a constant increase with Re_θ is observed, reaching $p^+_{w,\mathrm{rms}} \approx 2.74$ at $Re_\theta = 2500$, which is approximately 10% higher than for channel flow at a corresponding $Re_\tau = U_\tau\delta/\nu$ with δ being the 99%-boundary-layer thickness or the channel-half width, respectively.

Averaged results give only a limited insight into the complex dynamics of the turbulent flow close to a wall. In particular, flow structures of different scales and energies are populating the near-wall and logarithmic region and contribute to the turbulent stresses. Close to the wall, the well-known turbulent streaks are the characteristic structures, essentially scaling in wall units with a length and spacing of approximately 1000×120 wall units Kline *et al.* (1967). In this region, the present DNS results agree well with channel-flow data at high Re_τ Hoyas & Jiménez (2006). However, recent evidence from both experiments in pipes and boundary layers (see *e.g.* Ref. Kim & Adrian (1999); Hutchins & Marusic (2007) and the references therein), and DNS in channel flows del Álamo and Jiménez (2003) clearly shows that large structures, scaling in outer units, are also present. These structures reach their maximum

amplitude in the overlap region, but they penetrate into the buffer layer and might even contribute to a modulation of the near-wall streaks Hutchins & Marusic (2007*b*). Evidence from experiments and channel DNS suggests that the scaling of the large structures might be different for the various canonical flow cases, *e.g.* channel and boundary-layer flows. As the scale separation between inner and outer scaling is given by the Reynolds number Re_τ, such larger structures are more easily detected at higher Re_θ. For a quantification of the large-scale influence on the wall dynamics, we consider the fluctuating streamwise wall-shear stress τ_w. The fluctuation amplitude τ'_w/τ_w is approximately 0.42 at $Re_\theta = 2500$, in good agreement with DNS and experimental data from channel and boundary-layer flows at similar Re_τ Alfredsson *et al.* (1988). The normalized spanwise two-point correlation $R_{\tau\tau}$ is shown in Fig. 4. This correlation indicates the spanwise spacing of the dominant (streamwise) structures at the wall. The inner peak, corresponding to the near-wall streaks Kline *et al.* (1967), can clearly be seen with a spacing of about 120 (local) wall units, as the first minimum of $R_{\tau\tau}$ at $2\Delta z^+ \approx 120$ (dashed line in Fig. 4). However, a second peak (solid line) scaling as $2\Delta z \approx 0.85\delta_{99}$ is clearly visible in the two-point correlation for higher Re_θ, indicating the footprint of the large-scale structures onto the fluctuating wall-shear stress. Similar observations have also been made in channel-flow simulations by Abe *et al.* Abe *et al.* (2004). For $Re_\theta < 1000$, the two peaks merge into one and no clear separation is present. However, for $Re_\theta > 1500$ two distinct peaks can be observed. Note that for these Re_θ the outer peak is more dominant in terms of the correlation $R_{\tau\tau}$. These results show for the first time numerical evidence of these structures at the wall for a continuously increasing Reynolds number. It further highlights the fact that at least $Re_\theta \approx 1500$ is needed for a sufficient separation of the inner and outer spanwise peaks. Additionally, in agreement with boundary-layer measurements Hutchins & Marusic (2007), strong maxima of the streamwise velocity spectra related to the outer peak are reached at a wall-normal distance of approximately $0.15\delta_{99}$ and $0.4\delta_{99}$ when scaled with either U_τ^2 or the local u_{rms}^2, respectively. The inner peak is consistently found at a wall-normal distance of $y^+ \approx 15$ (see *e.g.* Ref. del Álamo and Jiménez (2003)).

In the present Letter, new simulations and experiments pertaining to the important canonical flow case of a spatially developing turbulent boundary layer under zero pressure gradient are presented up to $Re_\theta = 2500$. The laminar Blasius inflow in the simulations is located at $Re_\theta = 174$, and a localized trip forcing shortly after the inflow is causing rapid transition to turbulence, in a similar way as in the experiments. Thus, the spatial evolution of the boundary layer can be tracked over a large streamwise extent. Excellent agreement of both mean and fluctuating quantities is achieved, greatly reducing the uncertainty of boundary-layer statistics at the low to medium Reynolds numbers considered. The close agreement further validates that the results are insensitive to, *e.g.*, the details of surface roughness, tripping device, streamwise pressure gradients, boundary conditions. Thus, a generic zero-pressure-gradient

turbulent boundary layer is recovered in both cases, which allows for a careful comparison.

A first quantification of the turbulent flow structures close to the wall is presented in terms of two-point correlations of the wall-shear stress. It is seen that the boundary layer is dominated by large structures with sizes on the order of the boundary layer thickness that extend from the free stream down to the wall. At the wall, these structures are even more clearly visible in the fluctuating wall-shear stress than the well-known near-wall turbulent streaks, indicating that these large-scale structures might play a significant role for *e.g.* the skin friction.

Computer time was provided by the Swedish National Infrastructure for Computing (SNIC) and the Centre for Parallel Computers (PDC) at KTH, Stockholm. Financial support by the Swedish Research Council (VR) is thankfully acknowledged.

References

Abe, H., Kawamura, H. & Choi, H. 2004 Very large-scale structures and their effects on the wall shear-stress fluctuations in a turbulent channel flow up to Re[sub tau] = 640. *ASME J. Fluids Engng.* **126** (5), 835–843.

del Álamo, J. C. & Jiménez, J. 2003 Spectra of the very large anisotropic scales in turbulent channels. *Phys. Fluids* **15** (6), L41–L44.

Alfredsson, P. H., Johansson, A. V., Haritonidis, J. H. & Eckelmann, H. 1988 The fluctuating wall-shear stress and the velocity field in the viscous sublayer. *Phys. Fluids* **31** (5), 1026–1033.

Chevalier, M., Schlatter, P., Lundbladh, A. & Henningson, D. S. 2007 A pseudo-spectral solver for incompressible boundary layer flows. *Tech. Rep* TRITA-MEK 2007:07. Royal Institute of Technology, Stockholm.

Ferrante, A. & Elghobashi, S. 2005 Rreynolds number effect on drag reduction in a microbubble-laden spatially developing turbulent boundary layer. *J. Fluid Mech.* **543**, 93–106.

Honkan, A. & Andreopoulos, Y. 1997 Vorticity, strain-rate and dissipation characteristics in the near-wall region of turbulent boundary layers. *J. Fluid Mech.* **350**, 29–96.

Hoyas, S. & Jiménez, J. 2006 Scaling of the velocity fluctuations in turbulent channels up to $re_\tau = 2003$. *Phys. Fluids* **18** (011702), 1–4.

Hutchins, N. & Marusic, I. 2007*a* Evidence of very long meandering features in the logarithmic region of turbulent boundary layers. *J. Fluid Mech.* **579**, 1–28.

Hutchins, N. & Marusic, I. 2007*b* Large-scale influences in near-wall turbulence. *Proc. Roy. Soc. Lond. Ser. A* **365**, 647–664.

Johansson, A. V. & Alfredsson, P. H. 1983 Effects of imperfect spatial resolution on measurements of wall-bounded turbulent shear flows. *J. Fluid Mech.* **137**, 409–421.

Kays, W. M. & Crawford, M. E. 1993 *Convective Heat and Mass Transfer*, 3rd edn. McGraw-Hill, New York, U.S.A.

Kim, K. C. & Adrian, R. J. 1999 Very large-scale motion in the outer layer. *Phys. Fluids* **11** (2), 417–422.

Kline, S. J., Reynolds, W. C., Schraub, F. A. & Runstadler, P. W. 1967 The structure of turbulent boundary layers. *J. Fluid Mech.* **30**, 741–773.

Komminaho, J. & Skote, M. 2002 Reynolds stress budgets in Couette and boundary layer flows. *Flow, Turbulence Combust.* **68** (2), 167–192.

Kunkel, G. J. & Marusic, I. 2006 Study of the near-wall-turbulent region of the high-Reynolds-number boundary layer using an atmospheric flow. *J. Fluid Mech.* **548**, 375–402.

Marusic, I. & Kunkel, G. J. 2003 Streamwise turbulence intensity formulation for flat-plate boundary layers. *Phys. Fluids* **15** (8), 2461–2464.

Monkewitz, P. A., Chauhan, K. A. & Nagib, H. M. 2007 Self-consistent high-Reynolds-number asymptotics for zero-pressure-gradient turbulent boundary layers. *Phys. Fluids* **19** (115101), 1–12.

Österlund, J. M. 1999 Experimental studies of zero pressure-gradient turbulent

boundary layer flow. PhD thesis, Royal Institute of Technology, Stockholm, Sweden.

Österlund, J. M., Johansson, A. V., Nagib, H. M. & Hites, M. H. 2000 A note on the overlap region in turbulent boundary layers. *Phys. Fluids* **12** (1), 1–4.

Perry, A. E., Marusic, I. & Jones, M. B. 2002 On the streamwise evolution of turbulent boundary layers in arbitrary pressure gradients. *J. Fluid Mech.* **461**, 61–91.

Rüedi, J. D., Nagib, H. M., Österlund, J. M. & Monkewitz, P. A. 2003 Evaluation of three techniques for wall-shear stress measurements in three-dimensional flows. *Exp. Fluids* **35**, 389–396.

Schlichting, H. 1987 *Boundary Layer Theory*, 7th edn. McGraw-Hill, New York, U.S.A.

Spalart, P. R. 1988 Direct simulation of a turbulent boundary layer up to $Re_\theta = 1410$. *J. Fluid Mech.* **187**, 61–98.

Wu, X. & Moin, P. 2008 A direct numerical simulation study on the mean velocity characteristics in turbulent pipe flow. *J. Fluid Mech.* **608**, 81–112.

Paper 3

3

Simulations of high-Reynolds number turbulent boundary layers

By Philipp Schlatter, Qiang Li, Geert Brethouwer, Arne V. Johansson & Dan S. Henningson

Linné Flow Centre, KTH Mechanics
SE-100 44 Stockholm, Sweden

Submitted to Int. J. Heat Fluid Flow

Well-resolved large-eddy simulations (LES) of a spatially developing turbulent boundary layer under zero pressure gradient up to comparably high Reynolds numbers ($Re_\theta = 4300$) are performed. The laminar inflow is located at $Re_{\delta^*} = 450$ ($Re_\theta \approx 200$), a position where natural transition to turbulence can be expected. Simulations are validated and compared extensively to both numerical data sets, i.e. a recent spatial direct numerical simulation (DNS) up to $Re_\theta = 2500$ (Schlatter et al. 2009) and available experimental measurements, e.g. the ones obtained by Österlund (1999). The goal is to provide the research community with reliable numerical data for high Reynolds-number wall-bounded turbulence, which can in turn be employed for further model development and validation, but also to contribute to the characterisation and understanding of various aspects of wall turbulence.

The results obtained via LES show that good agreement with DNS data at lower Reynolds numbers and experimental data can be obtained for both mean and fluctuating quantities. In addition, turbulence spectra characterising large-scale organisation in the flow have been computed and compared to literature results with good agreement. In particular, the near-wall streaks scaling in inner units and the outer layer large-scale structures can clearly be identified in both spanwise and temporal spectra.

1. Introduction

Turbulent flow around bodies with solid walls is a very important research topic today for both technical and industrial as well as environmental applications. Whereas these flows are usually occuring in complex geometries with curved surfaces leading to pressure gradients or even bluff shapes promoting separation, the two-dimensional, spatially developing, zero-pressure-gradient turbulent boundary layer on a flat plate has emerged as an important canonical flow case for theoretical, numerical as well as experimental studies. Of large interest is for example the aspect of universality of the wall-normal profile of

the streamwise velocity component in the limit of high Reynolds numbers. Going back to the seminal work conducted by von Kármán in the first half of the 20th century, the so-called "law of the wall" composed of the linear region close to the wall, followed by a logarithmic overlap region up to about 10% of the boundary-layer thickness, has been the centre of intense discussions, see e.g. the section in the book by Pope (2000). In recent years, several careful experiments have been conducted for this canonical flow. For instance, Österlund *et al.* (2000) performed extensive measurements of mean and fluctuating quantities in the MTL wind tunnel at KTH Stockholm using hot-wire and hot-film anemometry for Reynolds numbers Re_θ based on the momentum thickness θ and the freestream velocity U_∞ ranging from 2530 to 27300; this data set includes five measurement positions below $Re_\theta = 6000$, which could are becoming accessible to numerical simulations. Partly based on these experimental data, Monkewitz *et al.* (2007) have recently presented various asymptotic results for high Reynolds numbers, including the mean velocity profile.

Careful analysis (Örlü 2009) of a large amount of literature data for (experimentally) low Reynolds number turbulent boundary-layer measurements yields that some of these data do not necessarily adhere to accurate zero-pressure-gradient equilibrium conditions and independent determination of the skin friction. Therefore, new experimental measurements in the MTL wind-tunnel at KTH Stockholm were performed by Örlü (2009) for a generic, two-dimensional turbulent boundary layer with special focus on equilibrium conditions, for $Re_\theta = 2331$ to 8792. Sample results have been included in Schlatter et al. (2009). This data will certainly be helpful in the future for detailed comparisons with simulation data obtained at high Re.

To get additional insight into the mean-flow properties of turbulent wall-bounded flows, there is increased interest in understanding the dynamics of such flows, both at large and small scales. This is highlighted by the recent article by Marusic (2009). Furthermore, initial studies by Kim & Adrian (1999) who discovered large-scale structures in wall-bounded flows, motivated the subsequent analysis of these channel, pipe and boundary-layer flows by many authors (see e.g. Hutchins & Marusic (2007); Guala *et al.* (2006); del Álamo and Jiménez (2003)).

However, as opposed to turbulent channel and pipe flow, relatively few numerical results of direct or large-eddy simulations (DNS/LES) pertaining to canonical turbulent boundary layers have been published for medium or high Reynolds numbers. In recent years, the advancement of computer technology has made it possible to perform simulations based on $\mathcal{O}(10^9)$ grid points; in channel geometry this allowed for reaching high Reynolds number higher than $Re_\tau = 2000$ (based on friction velocity U_τ and channel half width h) by means of DNS Hoyas & Jiménez (2006). The spatially developing boundary-layer geometry, however, proves more difficult for accurate simulations. In particular, the long streamwise extent of the domain, and the resulting longer averaging times due to the loss of one homogeneous directions require large computational

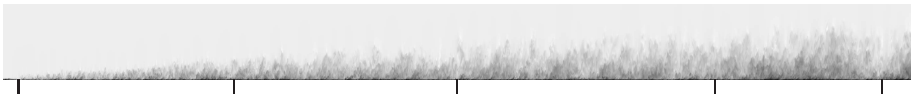

FIGURE 1. Instantaneous side view with grey-scale contours of the streamwise velocity component. The domain shown corresponds to the computational box for the present LES, reaching up to approximately $Re_\theta = 4400$. Note that only half of the domain extent in the wall-normal direction is shown, and the fringe region connecting outflow and inflow is not included. The representation of the box is enlarged by a factor four in the wall-normal direction.

effort even for moderate Re. In addition, the specification of inflow and outflow conditions, and equally important, proper freestream boundary conditions are essential for a successful simulation setup.

DNS relies on resolving all relevant temporal and spatial scales on the underlying numerical grid. In LES, however, the resolution requirements can be relaxed to some extent (Sagaut 2005). The large, energy-carrying scales of the flow are discretised on the grid and accurately simulated in both space and time, whereas the influence of the smaller scales, which are presumably more homogeneous, is modelled. For this purpose, a so-called subgrid-scale (SGS) model is then added to the equations of motion to compensate for the truncated resolution. Depending on flow case, accuracy requirements and employed SGS model, typically a reduction of the number of grid points by a factor of $\mathcal{O}(10)$ can be obtained for wall-resolved simulations compared to a DNS of the same case.

For boundary-layer flows, the DNS by Spalart (1988) using an innovative spatio-temporal approach provided valuable data at $Re_\theta = 300, 670, 1410$; this data set has been extensively used as reference for model development, and validation of experimental techniques for the last decades. As a next step, a simulation taking into account the true growth of the boundary layer in the downstream direction has been performed by Komminaho and Skote (2002) up to $Re_\theta = 700$. This technique to include proper inflow and outflow conditions in a spatially developing setting is usually termed "spatial simulation" as opposed to flow cases with parallel mean flows such as channel or pipe flows. Very recently, Wu & Moin (2009) performed a spatial DNS of a boundary layer undergoing transition due to a periodically passing box of turbulence; the turbulent state just after transition was located $Re_\theta = 900$ close to the outlet. A similar Re_θ was also simulated spatially by Li *et al.* (2009); this simulation also includes the advection of passive scalars with various Prandtl numbers. Focusing on higher Reynolds numbers, using a spectral method but limited to a fairly short domain, $Re_\theta = 2240$ was reached by Khujadze & Oberlack (2004). The highest Reynolds number reached in DNS to date is the data reported by

Ferrante & Elghobashi (2005) at $Re_\theta = 2900$, however obtained in a comparably short computational domain in which the turbulence, in particular the large-scale structures, may not be fully captured.

A DNS using a spectral method similar to the one used by Komminaho and Skote (2002) was presented by Schlatter et al. (2009), reaching $Re_\theta = 2500$ in a fully spatial setup with the (laminar) inlet located at $Re_\theta \approx 200$. A comparison with new experiments performed at the same Reynolds number revealed excellent agreement between DNS and measurements. This dataset will be used in the present work extensively to validate the chosen simulation approach.

For turbulent boundary layers, the Reynolds number $Re_\theta \approx 4300$ has to be considered at present high from a simulation point of view. Due to the difficulty of performing simulations and experiments at Reynolds numbers Re_θ on the order of a few thousand, there is a comparably large spread of the existing data in the literature for integral, mean and fluctuating turbulent quantities, see e.g. Honkan & Andreopoulos (1997). There is thus a need for accurate and reliable simulation data of spatially developing turbulent boundary layers with Re_θ to be compared to high-quality experimental results. To this end, the inflow in the numerical simulation should be positioned far enough upstream, i.e. comparable to where natural transition occurs, to ensure that the flow reaches a fully developed, undisturbed equilibrium state further downstream. However, as pointed out by Österlund *et al.* (2000), a clear overlap region can only be detected above $Re_\theta \approx 6000$, which might be just about to become accessible for adequately resolved transient numerical simulations.

The aim of the present study is to perform and validate well-resolved spatial large-eddy simulations (LES) in an effort to obtain accurate and reliable data at higher Reynolds numbers exceeding $Re_\theta = 2000$. A snapshot of such a simulation is presented in Fig. 1, with several relevant downstream positions indicated. The inflow is positioned at a low streamwise Reynolds number, $Re_{\delta^*} = 450$ based on the displacement thickness δ^* at the inlet. An exhaustive amount of statistics, e.g. one and two-point statistics, Reynolds-stress budgets and time series pertaining to turbulent quantities, are collected and evaluated.

The paper is organised as follows. In Section 2 the numerical method and the simulation parameters are introduced. Then, Section 3 discusses statistical quantities such as mean profiles, fluctuations and budgets. Spectral information about turbulent structures are introduced in Section 4. Finally, conclusions are given in Section 5.

2. Numerical methodology

The simulations are performed using a fully spectral method to solve the three-dimensional, time-dependent, incompressible Navier-Stokes equations (Chevalier *et al.* 2007). In the wall-parallel directions, Fourier series with dealiasing are used, whereas the wall-normal direction is discretised with Chebyshev polynomials. The discretisation is based on a velocity-vorticity formulation to exactly enfore continuity. Time is advanced with a standard mixed Crank-Nicolson/Runge-Kutta scheme. The periodic boundary conditions in the streamwise direction are combined with a spatially developing boundary layer by adding a "fringe region" at the end of the domain (Chevalier *et al.* 2007; Nordström et al. 1999). In this region, the outflowing fluid is forced via a volume force to the laminar inflowing Blasius boundary-layer profile, located at $Re_{\delta_0^*} = 450$ based on the displacement thickness δ_0^* at the inlet. A low-amplitude trip force acting in the wall-normal direction is used to cause rapid laminar-turbulent transition close to the inlet (see Fig. 1). Compared to the reference DNS (Schlatter et al. 2009) the forcing amplitude is marginally reduced which leads to slightly later transition. The boundary conditions in the freestream are of Neumann type, i.e. the wall-normal variation of the velocity components is forced to zero at the upper boundary. This requirement together with incompressibility leads to a constant streamwise velocity at the upper boundary, whereas the normal velocity component might be non-zero to account for the boundary-layer growth. The spectral method provides excellent accuracy and dispersion properties as compared to low-order discretisations.

The computational domain is $x_L \times y_L \times z_L = 6000\delta_0^* \times 200\delta_0^* \times 240\delta_0^*$ with $4096 \times 385 \times 384$ spectral collocation points in the streamwise, wall-normal and spanwise directions, respectively. The height of the computational domain is chosen to be at least three times the largest 99%-boundary-layer thickness δ_{99}; in the spanwise direction an even larger domain has been chosen to ensure the correct development of large-scale structures scaling in outer units. The grid points are non-equidistantly distributed in the wall-normal direction, with at least 10 collocation points within the region $y^+ < 10$. The maximum grid spacing in viscous units is then $\Delta x^+ \times \Delta y^+_{\max} \times \Delta z^+ = 25.3 \times 14.2 \times 10.8$. The statistics are sampled on-the-fly over $\Delta t^+ \approx 50,000$ viscous time units, or 36 in terms of δ_{99}/U_τ at $Re_\theta = 4300$. Owing to the high computational cost of the simulations, the numerical code is fully parallelised running on $\mathcal{O}(1000)$ processors (Li *et al.* 2008). In total, the present simulation required $2 \cdot 10^6$ core hours on a PC cluster.

Since the chosen resolution is not adequate for a direct numerical simulation, the unresolved quantities have to be treated via a subgrid-scale model. In the present case, the ADM-RT model (Schlatter *et al.* 2004) has been employed, supplementing the governing equations with a dissipative term. The equations of motion for the resolved velocity $\overline{u}_i$ and pressure $\overline{p}$ thus read

$$\frac{\partial \overline{u}_i}{\partial t} + \overline{u}_j \frac{\partial \overline{u}_i}{\partial x_j} = -\frac{\partial \overline{p}}{\partial x_i} + \frac{1}{Re} \frac{\partial^2 \overline{u}_i}{\partial x_j \partial x_j} - \chi H_N * \overline{u}_i \ , \qquad (1)$$

together with the incompressibility contraint $\partial\overline{u}_i/\partial x_i = 0$. The relaxation term $\chi H_N * \overline{u}_i$ is based on a high-order three-dimensional filter operation H_N convoluted with $\overline{u}_i$. The model coefficient χ was chosen to be a constant throughout the whole flow domain (Schlatter *et al.* 2006). The effect of this addition is to cause fluctuations close to the numerical cutoff to be damped. This additional dissipation regularises the flow solution, and allows to perform accurate simulations of both transitional and turbulent flows at reduced resolution, in particular for simulation methods based on spectral discretisation, see e.g. Schlatter *et al.* (2006). Note that the ADM-RT model converges by construction towards a DNS with increasing resolution. For the present simulation case the grid resolution has been chosen to be very fine for an LES. It is not the aim here to validate the modelling per se, but rather to obtain accurate simulation data at high Reynolds numbers for turbulent boundary layers.

3. Averaged results

As mentioned above, the laminar inflow for the present simulation is located at $Re_{\delta^*} = 450$, roughly corresponding to $Re_\theta = 200$, which is low enough to ensure a physical flow development further downstream, see also Fig. 1. Once a statistically stationary state has been reached, statististics are averaged over the spanwise direction z and time t. Thus the Reynolds decomposition

$$u = \langle u \rangle + u' = U + u' \tag{2}$$

is used, the brackets $\langle\cdot\rangle$ indicating the average in z and t. Based on the mean velocity profile $U(x, y)$ the shear stress at the wall is obtained as $\tau_w(x) = \mu(\mathrm{d}U/\mathrm{d}y)|_{y=0}$. Following the classical theory of turbulent boundary layers (see e.g. Pope 2000), the friction velocity U_τ provides the relevant velocity scale throughout the boundary layer, whereas the viscous length scale $\ell_\star$ is the characteristic length at least close to the wall. The scaled quantities in wall scaling are thus written as, e.g., $U^+ = U/U_\tau$ and $y^+ = y/\ell_\star$.

First, integral quantities of the boundary layer such as the friction coefficient are presented. Then, the mean velocity profile and profiles and budgets of turbulent fluctuating quantities are discussed. Section 4 is devoted to an analysis of the turbulent structures.

The skin-friction coefficient c_f is shown in Fig. 2. The transitional region at the beginning of the domain is clearly visible. According to the computed value of c_f the LES is seen to reach a fully-developed state around $Re_\theta \approx 700$. The comparison of the LES data with two data sets obtained from DNS (Schlatter et al. 2009; Li *et al.* 2009) is very good. Note that both DNS data were obtained based on a similar numerical setup as the present LES; however in the LES the forcing amplitude was slightly reduced in order to have a smoother laminar-turbulent transition close to the inlet. This is clearly visible in Fig. 2 and subsequent figures as a tendency of the LES to approach the fully developed turbulent state later than the reference DNS. Somewhat surprisingly, the comparably simple empirical correlation $c_f = 0.024 Re_\theta^{(-1/4)}$ (Kays and Crawford

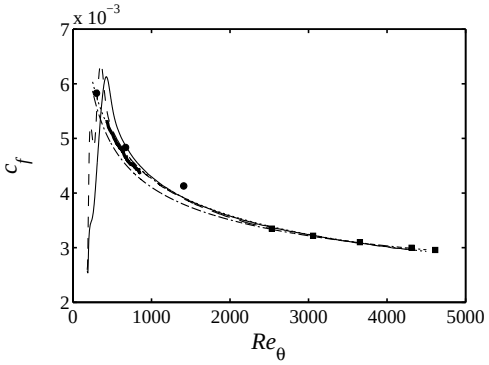

FIGURE 2. Skin-friction coefficient c_f as a function of Re_θ. ——present LES, – – –DNS (Schlatter et al. 2009), ····· $c_f = 0.024 Re_\theta^{(-1/4)}$ (Kays and Crawford 1993), –·–$c_f = 2[(1/0.38)\log Re_\theta + 4.08]^{-2}$ (Österlund 1999). • DNS by Spalart (1988), ■ experimental results by Österlund (1999), ——DNS by Li *et al.* (2009).

1993) provides an accurate fit to the present LES data for the range of Reynolds numbers considered; this has already been observed for the DNS data. On the other hand, the correlation $c_f = 2[(1/0.38)\log Re_\theta + 4.08]^{-2}$ based on the logarithmic region (Österlund 1999) is marginally underpredicting the friction for lower Re. Moreover, the agreement with the experimental measurement points (Österlund 1999) in the range $Re_\theta = 2500$ to 4300 is very good. Recall that experimentally the skin friction is obtained using an oil-film technique which is independent of the hot-wire velocity measurements. For comparison, the data points of the DNS by Spalart (1988) are also shown in Fig. 2. In this case, the skin friction is overpredicted by approximately 5% at his highest $Re_\theta = 1410$. This might be a residual effect of the spatio-temporal approach employed for the simulation, which does not extend to higher Reynolds numbers.

The shape factor $H_{12} = \delta^*/\theta$, defined as the ratio of displacement δ^* to momentum thickness θ, is shown in Fig. 3; H_{12} is often used as an easy way of characterising the state of development of a boundary layer. Moreover, it has been shown that H_{12} is a sensitive indicator of the quality of the boundary-layer data (Chauhan *et al.* 2009). In Fig. 3 it can again be seen that the LES is undergoing transition later than the DNS as mentioned above, and consequently approaches a fully developed state later; it is interesting to note that this state can be estimated to be reached at about $Re_\theta \approx 900$. This number appears to be slightly higher than what has been estimated for c_f; this further indicates that the the region close to the wall is reaching a fully turbulent state earlier than the region further away from the wall. Therefore, for the present simulation the boundary layer can be assumed to be in equilibrium for an extended range of Reynolds numbers of about $Re_\theta = 900 - 4300$, which

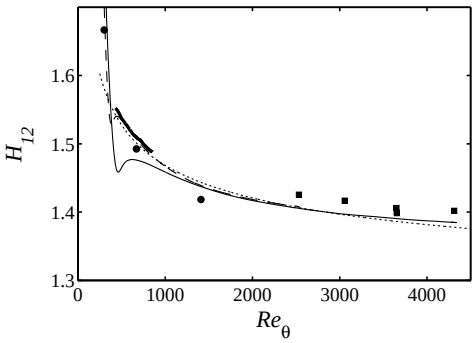

FIGURE 3. Shape factor H_{12} as a function of Re_θ. ——present LES, - - -DNS (Schlatter et al. 2009), ····· correlation by Monkewitz *et al.* (2007), • DNS by Spalart (1988), ■ experimental results by Österlund (1999), ——DNS by Li *et al.* (2009).

corresponds to $Re_\tau = 350 - 1350$ with Re_τ being based on the boundary-layer thickness δ_{99}.

Profiles of the mean velocity scaled in viscous units $U^+(y^+)$ obtained from the present LES are shown in Figure 4. For comparison, both DNS data from Spalart (1988) and Schlatter et al. (2009) and experimental results by Österlund (1999) are shown as well. The similarity at the higher Reynolds numbers, i.e. $Re_\theta = 2500 - 4300$, is very satisfactory. In particular, the scaled U^+_∞ in the freestream is accurately predicted by the simulation, and the onset and general shape of the wake region matches the one from the experiment. However, there is a discrepancy between the present simulation data and that of Spalart highest Reynolds number, $Re_\theta = 1410$. This difference might again be attributed to the spatio-temporal simulation approach in the latter. In addition, at $Re_\theta = 2500$ there is virtually no difference between the DNS and the present LES, which indicates that the mean flow is well captured even by the lower resolution LES. In the near-wall region, all data collapse nicely on the linear relation $U^+ = y^+$ as expected according to the expansions in the viscous sublayer. In the figure, the von Kármán coefficient κ used to indicate the logarithmic region $(1/\kappa)\log y^+ + B$ is chosen as $\kappa = 0.41$ which seems to be a good compromise for the present Re_θ.

The log-law indicator function $\Xi = y^+(\mathrm{d}U^+/\mathrm{d}y^+)$ is presented in Fig. 5. The general shape of the composite profile proposed by Monkewitz *et al.* (2007) is followed up to $y/\delta_{99} \approx \mathcal{O}(0.1)$, the position where the wake region is expected to begin (indicated by the symbol • in the Figure). In the overlap region Ξ essentially measures the (inverse) von Kármán constant κ. From the present data, the minimum of Ξ is reached at $y^+ \approx 70$ with a value of $1/\Xi \approx 0.428$ in good agreement with the prediction by Monkewitz *et al.* (2007), but also

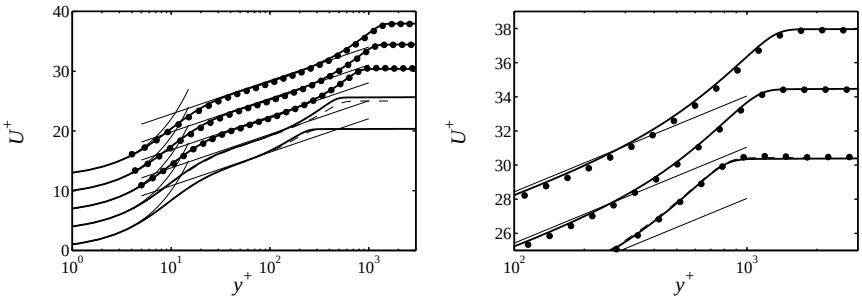

FIGURE 4. Mean velocity profile U^+ in viscous units for ——present LES at $Re_\theta = 685, 1433, 2560, 3660, 4307$, • measurements by Österlund (1999) at $Re_\theta = 2532, 3651, 4312$. - - -DNS by Spalart (1988) at $Re_\theta = 670, 1410$, and DNS by Schlatter et al. (2009) at $Re_\theta = 2511$ (practically invisible). The profiles are shifted by $U^+ = 3$ along the ordinate for increasing Re_θ. The linear and logarithmic regions are indicated by a thin line, using $1/\kappa \log y^+ + B$ with $\kappa = 0.41$ and $B = 5.2$.

DNS results in both channel and boundary layers. The higher the Reynolds number, the longer the present LES data follows the composite profile, including the decreasing κ (increasing Ξ) after the minimum at $y^+ \approx 70$. However, even $Re_\theta = 4300$ is too low to reach an asymptotical logarithmic region (Österlund *et al.* 2000) with the proposed $\kappa \approx 0.38$. Ξ in the wake region shows a clear trend towards higher maxima for increasing Re. In addition, it is interesting to note that in the inner region ($y^+ \approx 10$) the channel data by Hoyas & Jiménez (2006) features a slightly larger Ξ than the boundary-layer data. This behaviour is similar to a boundary layer under (weak) favourable pressure gradient (Schlatter & Brandt 2008), which demonstrates the sensitivity of the near-wall region to possible pressure gradients as present in e.g. channel flow.

The velocity fluctuations, e.g. $u_{\mathrm{rms}} = \sqrt{\langle u'u' \rangle}$, and the Reynolds shear stress $\langle u'v' \rangle$ are depicted in Figure 6 in wall scaling. The agreement between the LES and DNS at $Re_\theta = 2500$ is good; slight differences can be observed for the high fluctuation regions close to the wall, in which the LES tends to underpredict the maxima by 1-2 percent. A similar issue related to the spanwise resolution is further discussed in connection with Fig. 16 further down.

As mentioned in many studies, there is only incomplete collapse in inner scaling (see e.g. Hoyas & Jiménez 2006), most dominantly for the streamwise and spanwise fluctuations. In particular, the maximum wall-normal value of u_{rms} is constantly increasing with Re as shown in e.g. Metzger & Klewicki (2001), as well as in channel-flow simulation results. On the other hand, the total shear stress, $-\langle u'v' \rangle + (1/Re)\mathrm{d}\langle U \rangle/\mathrm{d}y$, scales very well in outer length units for the considered range of Re_θ, and is therefore not shown.

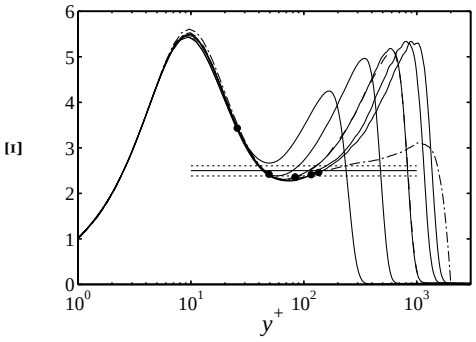

FIGURE 5. Indicator function $\Xi = y^+(\mathrm{d}U^+/\mathrm{d}y^+)$ for increasing $Re_\theta = 685, 1433, 2560, 3660, 4307$. ——present LES, – – –DNS (Schlatter et al. 2009). –·–DNS of channel flow (Hoyas & Jiménez 2006). The horizontal lines correspond to a von Kármán contant of $1/\kappa = 1/0.38$, $1/0.4$ and $1/0.42$, respectively. The symbol • corresponds to $0.1\delta_{99}$ for each respective Re.

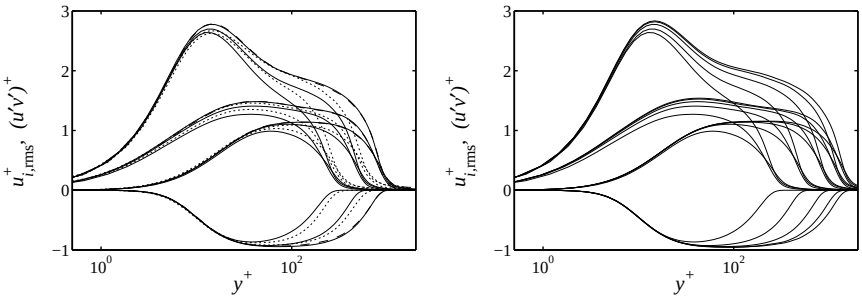

FIGURE 6. *Left:* Reynolds stresses for the ——present LES at $Re_\theta = 685, 1433, 2560$, ·····Spalart (1988) at $Re_\theta = 670, 1410$ and – – –Schlatter et al. (2009). *Right:* Reynolds stresses for $Re_\theta = 685, 1433, 2560, 3660, 4307$.

The fluctuation of the wall-normal gradient of the velocity, i.e. the fluctuating streamwise wall-shear stress τ_w is considered in Fig. 7. As shown by Alfredsson *et al.* (1988) in good agreement with data obtained by various experimental techniques and simulation approaches, $\tau^+_{\mathrm{rms}} \approx 0.4$ in wall-bounded flow. For the present LES, a Re-dependence is clearly found. A fit $\tau_{w,\mathrm{rms}} = 0.0155 \log Re_\tau + 0.317$ describes the present data. Here, Re_τ is based on the friction velocity U_τ and the boundary-layer thickness δ_{99} or the channel half-width h. The correlation provides a reasonable description for Spalart's

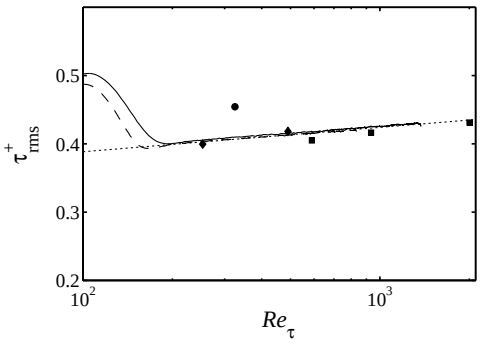

FIGURE 7. Fluctuations of the wall shear stress $\tau_{\rm rms}$ for ——— present LES, – – – DNS Schlatter et al. (2009), ◇ DNS by Spalart (1988), • DNS by Wu & Moin (2009), ■ DNS of channel flow (Moser *et al.* 1999; del Álamo *et al.* 2004). ····· Fit to present data: $0.0155 \log Re_\tau + 0.317$.

DNS and various channel-flow simulations (see also e.g. Abe *et al.* 2004). However, the data point obtained from the DNS by Wu & Moin (2009) clearly shows a higher value. This suggests that these data are in fact not fully-developed turbulence, but rather transitional in nature; also for the present boundary-layer data, a higher $\tau^+_{\rm rms}$ is obtained shortly after transition.

Based on the simulation results, the individual terms in the von Kármán integral equation, here written for a zero-pressure-gradient boundary layer,

$$u_\tau^2 = U_\infty^2 \frac{\mathrm{d}\theta}{\mathrm{d}x} + \frac{\mathrm{d}}{\mathrm{d}x} \int_0^\infty \left(\langle u'^2 \rangle - \langle v'^2 \rangle \right) \mathrm{d}y \ , \tag{3}$$

relating the local skin friction to the growth of the momentum thickness θ may be considered, see Fig. 8. It turns out that the term $U_\infty^2 \mathrm{d}\theta/\mathrm{d}x$ is $\mathcal{O}(50)$ times larger than the second relevant term, the integrated normal-stress difference. On the other hand, the expressions on both sides of the equation sign balance each other to within less than 0.5%. In addition, Fig. 8 also provides a practical measure for the useful region of the simulation, i.e. the region in which an equilibrium turbulent boundary layer adhering to the boundary-layer equations is recovered. For the present case, $Re_\theta = 900 - 4300$ can be estimated (see also comments to Figs. 2 and 3 above).

Particularly in the modelling community, there is considerable interest in data pertaining to the behaviour of the pressure and its fluctuations throughout the boundary layer. Experimentally, it is very difficult to accurately measure the pressure (Tsuji *et al.* 2007). In Fig. 9 the wall-pressure fluctuations are shown, and Fig. 10 provides wall-normal profiles of $p_{\rm rms}$ with different scalings. Although the pressure in an incompressible LES is strictly not a well-defined quantity as it might contain subgrid-scale contributions, the agreement between DNS and LES at $Re_\theta = 2500$ is statisfactory. It can further be seen that a

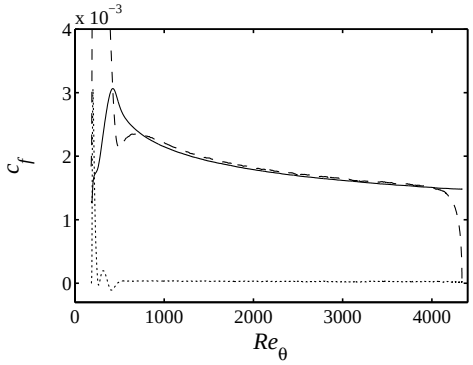

FIGURE 8. ——Skin friction coefficient c_f compared to the individual terms of the von Kármán equation: ····· integral of the normal-stress difference, – – –$U_\infty^2 \mathrm{d}\theta/\mathrm{d}x$.

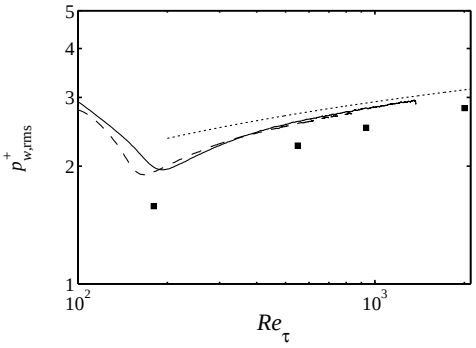

FIGURE 9. ——Pressure fluctuations at the wall $p^+_{w,\mathrm{rms}}$ as a function of the friction Reynolds number Re_τ, ——present LES, – – –DNS Schlatter et al. (2009), ····· $(p^+_{w,\mathrm{rms}})^2 = 6.5 + 1.86\log(Re_\tau/333)$ (Farabee & Casarella 1991). ■ DNS of channel flow (Moser *et al.* 1999; del Álamo *et al.* 2004; Hoyas & Jiménez 2006).

mixed scaling $p_{w,\mathrm{rms}}/(U_\tau \cdot U_\infty)$ is most appropriate close to the wall, reaching a value of approximately $p_{w,\mathrm{rms}} \approx 0.11 U_\tau U_\infty$ at the wall $y = 0$. In pure inner scaling, a collapse of the data at various $Re_\theta > 1000$ can be seen for $y^+ > 200$. At the wall, p_{rms} is approximately 10% higher than the pressure fluctuations in channel flow at a corresponding Re_τ.

In addition to the various mean and fluctuating quantities, of which a selection has already been presented, the budgets of the full Reynolds-stress tensor were computed. A sample result in Fig. 11 shows the budget of the turbulent

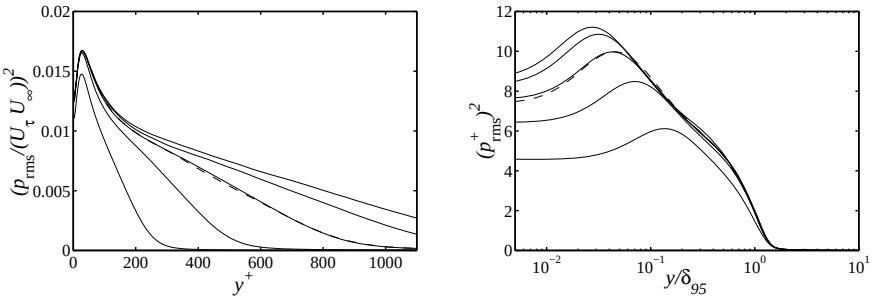

FIGURE 10. ——Wall-normal profiles of the pressure fluctuations for the present LES at $Re_\theta = 685, 1433, 2560, 3660, 4307$. - - -DNS Schlatter et al. (2009) at $Re_\theta = 2511$.

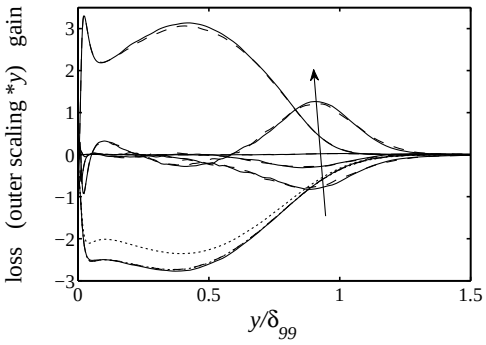

FIGURE 11. Budget of the turbulent kinetic energy for ——present LES and - - -DNS (Schlatter et al. 2009) at $Re_\theta = 2114$. Budget terms are multiplied with y/δ_{99} and scaled in outer units u_τ^3/δ_{99}. Quantities in the direction of the arrow: Convection, dissipation (····· resolved dissipation for LES), velocity-pressure correlation, viscous diffusion, production, turbulent diffusion.

kinetic energy $k = (1/2)\langle u_i' u_i' \rangle$. The activity of the SGS model during the simulation is clearly highlighted by the difference between the resolved dissipation and the total dissipation which includes the dissipation due to the SGS transfer. In the near-wall region this additional dissipation contributes as much as 20% to the total dissipation of the turbulent energy k. Furthermore, the comparison of the budget terms obtained from DNS and LES compare favourably at $Re_\theta = 2100$. Close to the wall, the classical visous scaling does show the well-known behaviour of wall-bounded flows (see e.g. Pope 2000), and a very good collapse of the individual terms with increasing Re is observed. The outer part of the boundary layer however is more interesting, as it highlights some

of the major differences between internal (channel, pipe) and external wall-bounded flows. In the highly intermittent region close to the boundary-layer edge $y \sim \delta_{99}$, a new balance between turbulent diffusion as a source, and turbulent convection and velocity-pressure correlation on the loss side is established; convection is virtually absent from the near-wall region, and identically zero in parallel flows.

4. Turbulent structures

Turbulent flow is characterised by the interaction of fluctuations and eddies of various sizes, shapes and energies. It is the ensemble of these eddies that eventually lead to, e.g., the characteristic law of the wall, or the well-known profiles of the rms values. Close to the wall, the kinematic restrictions lead to the appearance of distinct flow structures which evolve with their own dynamics. The most apparent turbulent structures close to solid walls are the turbulent streaks, described and characterised by many researchers, see e.g. Kline *et al.* (1967); Kim et al. (1987), and more recently Lin *et al.* (2008). Streaks are regions of elevated or decreased velocity as compared to the local mean velocity; their size is essentially scaling in wall units, and their medium length and spacing is usually given as approximately 1000×100 wall units.

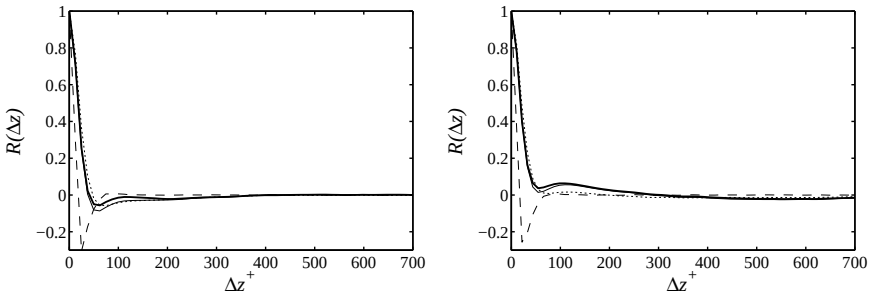

FIGURE 12. Spanwise two-point correlation $R_{\alpha\alpha}(\Delta z)$ for ——streamwise velocity u, – – –wall-normal velocity v, ····· spanwise velocity w (at $y^+ \approx 8$) and ——the wall shear stress τ_w. *Left:* $Re_\theta = 1430$, *Right:* $Re_\theta = 4006$.

The spanwise organisation of the structures in near-wall turbulence may be considered by calculating spanwise two-point correlations $R_{\alpha\alpha}$ of a given turbulent quantity α. In Fig. 12, the spanwise two-point correlations of the velocity components at $y^+ \approx 8$, and of the wall shear stress τ_w are shown. It can be observed that the behaviour of $R_{\tau\tau}$ and R_{uu} is very similar, featuring a first minimum at $\Delta z^+ \approx 60$. The two-point correlation of the wall-normal velocity component R_{vv} exhibits a strong minimum at $\Delta z \approx 25$ (Kim et al. 1987), about at half the separation as for u. However, with increasing Re_θ the first minimum of R_{uu} weakens and moves to higher values, and a second flat

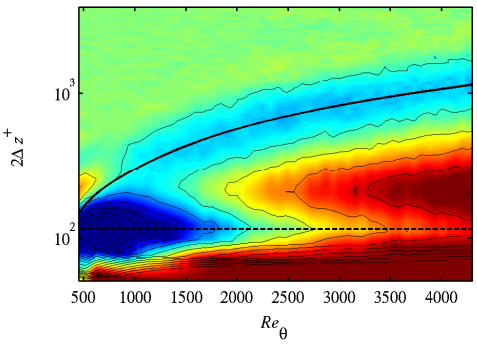

FIGURE 13. Spanwise two-point correlation $R_{\tau\tau}$ of the wall-shear stress τ_w computed from the present LES. The spanwise axis is scaled by the displacement $2\Delta z$ in order to directly show the spanwise pattern spacing. ——corresponds to $0.85\delta_{99}$, - - -corresponds to 120 plus units. The colors range from blue ($R_{\tau\tau} \leq -0.06$) to red ($R_{\tau\tau} \geq 0.06$); contour lines go from -0.15 to 0.15 with spacing 0.02.

minimum appears at large separation $\Delta z = \mathcal{O}(\delta_{99})$ (Österlund 1999). This indicates that superimposed onto the smaller-scale streaky structures a wider modulation must exist. Such large-scale turbulent structures have received considerable interest over the last years, both experimentally (e.g. Kim & Adrian 1999; Guala *et al.* 2006; Hutchins & Marusic 2007) and numerically (del Álamo and Jiménez 2003); open questions relate to the dynamic importance of these structures and possible explanations of their origin and regeneration. To further characterise the spanwise scaling, Fig. 13 shows a map of the two-point correlation of the wall-shear stress $R_{\tau\tau}$ as a function of the Reynolds number Re_θ. At any sufficiently high Re_θ two minima can be discerned: The inner peak, corresponding to the near-wall streaks, can clearly be seen with a spacing of about 120 (local) wall units, as the first minimum of $R_{\tau\tau}$ at $2\Delta z^+ \approx 120$ (dashed line in Figure 13). However, a second peak (solid line) scaling as $2\Delta z \approx 0.85\delta_{99}$ is clearly visible in the two-point correlation for higher Re_θ, indicating the footprint of the large-scale structures onto the fluctuating wall-shear stress. For $Re_\theta < 1000$, the two peaks merge into one and no clear separation is present. However, for $Re_\theta > 1500$ two distinct peaks can be observed. A similar plot is also shown in Schlatter et al. (2009), however being restricted to $Re_\theta < 2500$. The scales measured at the wall are essentially the same in the DNS and LES.

4.1. *Spanwise spectra*

The influence of the Reynolds number on the scale separation between the small scale (inner) peak and the larger scale (outer) peak is demonstrated in Fig. 14 with the help of premultiplied spanwise spectra $k_z\Phi_{uu}(\lambda_z)/u^2_{\mathrm{rms}}$ of the streamwise velocity u. The small-scale peak corresponding to the streaks is centred

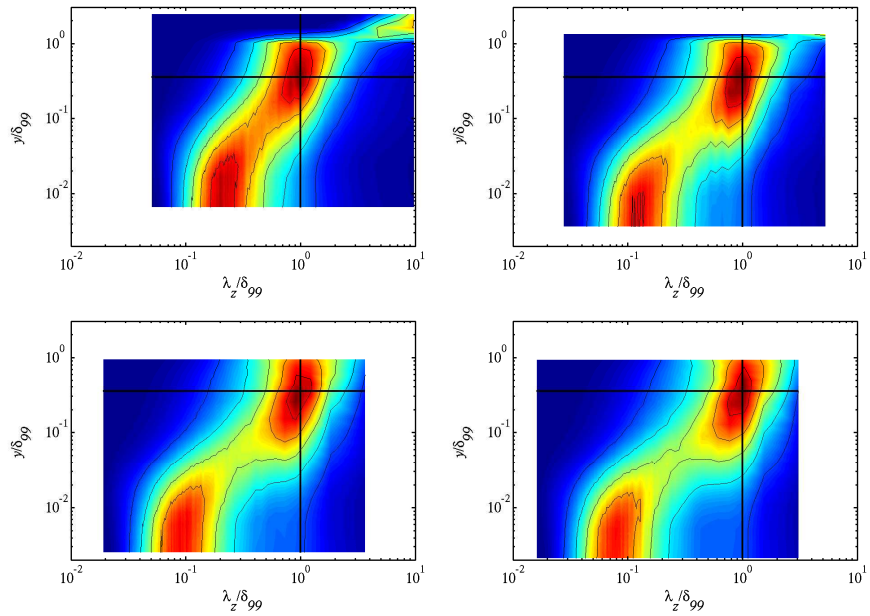

FIGURE 14. Premultiplied spanwise spectra $k_z\Phi_{uu}(\lambda_z)/u^2_{\rm rms}$ of the streamwise velocity fluctuation u. The vertical lines indicate $\lambda_z = \delta_{99}$, the horizontal lines $y = 0.35\delta_{99}$; contour lines have a spacing of 0.1. From *left* to *right* and *top* to *bottom*: $Re_\theta = 1433, 2560, 3660, 4307$.

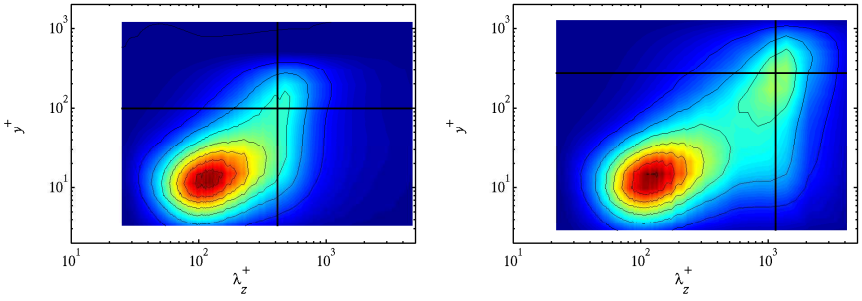

FIGURE 15. Premultiplied spanwise spectra $k_z\Phi_{uu}(\lambda_z)/U^2_\tau$ of the streamwise velocity fluctuation u. The vertical lines indicate $\lambda_z = 0.85\delta_{99}$, the horizontal lines $y = 0.2\delta_{99}$, contour line spacing 0.5. *Top*: $Re_\theta = 1433$, *bottom*: $Re_\theta = 4307$.

around 120 plus units, whereas the large-scale peak is clearly scaling in outer units, i.e. attaining its maximum at a wall-normal distance of approximately $y = 0.35\delta_{99}$ with a spanwise size $\lambda_z \approx \delta_{99}$. Scaling the energy spectra with

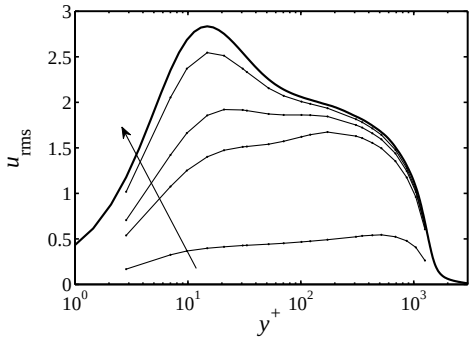

FIGURE 16. Dependence of resolved u_{rms} fluctuations on the range of spanwise scales included at $Re_\theta = 4307$. ——u_{rms} with full LES resolution $\Delta z^+ = 10.8$, ——in direction of arrow: scales $\geq 2000^+$, $\geq 250^+$, $\geq 100^+$, $\geq 40^+$.

U_τ^2 (Fig. 15), the inner peak features a clear maximum at $y^+ = 15$ (see e.g. del Álamo and Jiménez 2003)), and the outer peak reaches its maximum at a wall-normal distance of approximately $0.2\delta_{99}$.

Closely connected to the spectral distribution of fluctuation energy in a signal is the way how such a signal might be measured with reduced resolution. For example, hotwire sensors have a finite length, and thus measure in fact an average signal over this specific length (Hutchins *et al.* 2009). This averaging operation could be simplified (i.e. by not considering any nonlinear transfer function of the wire etc.) as an integral in wavenumber space of the fluctuation energy with a lower limit that corresponds to the cutoff wavenumber (i.e. the inverse sensor length). The result of such a calculation is shown in Fig. 16 for the streamwise velocity fluctuation u_{rms}. It becomes apparent that limiting the integration of the total fluctuations to scales larger than 40 plus units already has a significant impact on the results. In particular, for a lower limit of $\geq 250^+$, the outer peak becomes more dominant than the inner peak (Hutchins *et al.* 2009).

4.2. *Temporal spectra*

As opposed to channel flow computed in a (streamwise) periodic domain, the definition of streamwise spectra and thus the streamwise size of the turbulent structures is not as obvious in boundary-layer flow due to the spatial development. Usually, temporal signals are recorded at a given position, and then the Taylor hypothesis is invoked, assuming a certain convection velocity $U_c(x, y)$ in an effort to transform temporal spectra into spatial ones. This procedure naturally assumes that the convection velocity is only a function of the position, but not of the size of scales; which might not be entirely true. Therefore, in the present contribution only temporal spectra are shown, without conversion

into spatial spectra. Nevertheless, as a side note, the convection velocity for the present LES has been evaluated and similar results as e.g. Quadrio & Luchini (2003) have been obtained: The mean convection velocity closely follows the mean velocity profile, and levels off close to the wall with about $U_c^+ \approx 11$, featuring a small dip at $y^+ \approx 5$.

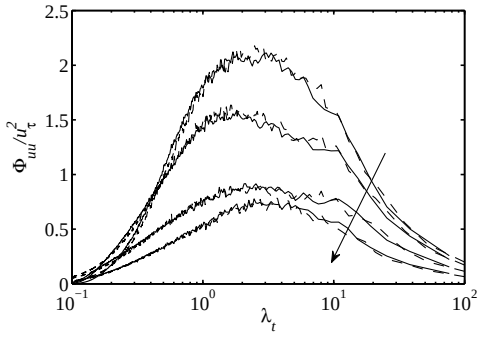

FIGURE 17. One-dimensional premultiplied temporal spectrum $\omega\Phi_{uu}(\lambda_t)/U_\tau^2$ of the streamwise velocity fluctuation u at $Re_\theta = 2500$ for ——present LES, – – –DNS Schlatter et al. (2009). In direction of the arrow: $y^+ = 15, 30, 100, 300$.

The temporal spectra were recorded at various positions in the flow and subsequently transformed using Hanning windows based on the Welch method with up to 64 overlapping windows. In Fig. 17 premultiplied temporal spectra obtained from the present LES and the reference DNS are compared at $Re_\theta = 2500$ at various wall-normal positions. Both simulation approaches show spectra which are very similar; the main peak at $\lambda_t \approx 3\delta_{99}/U_\infty$ (corresponding to about 1000 plus units when converted in spatial spectrum) and the flanks are accurately reproduced by the LES.

Contour plots of premultiplied temporal spectra are presented in Fig. 18 for two Reynolds numbers $Re_\theta = 1433$ and 4307. Note the good agreement of the present higher-Re data to the results reported in the experimental study by Hutchins & Marusic (2007). A fairly broad range of temporal frequencies is seen to be excited in the near-wall region ($y \approx 15$), and with higher Re a tendency towards larger (i.e. longer lasting) structures is seen in the outer region $y > 0.1\delta_{99}$. The longest relavant scales can be estimated to be $\mathcal{O}(40)$ in units of δ_{99}/U_∞, however longer events $> 100\delta_{99}/U_\infty$ are also observed. The most dominant structure in the outer region is observed at a constant (temporal) period of approximately $\lambda_t = 10\delta_{99}/U_\infty$. Via the consideration of two-dimensional spectra (not shown) this structure could be identified with having a spanwise scale $\lambda_z = 0.85\delta_{99}$. Assuming a convection speed of about $0.6U_\infty$, a length scale $\lambda_x = 6\delta_{99}$ is obtained, which compares well to the experimental finding presented by Hutchins & Marusic (2007) for boundary-layer flow.

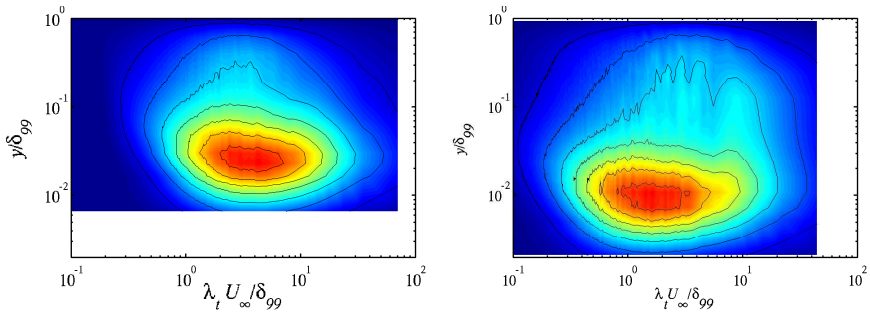

FIGURE 18. Premultiplied temporal spectrum $\omega\Phi_{uu}(\lambda_t)/U_\tau^2$ of the streamwise velocity fluctuation u. Contour spacing 0.3. *Left*: $Re_\theta = 1433$, *right*: $Re_\theta = 4307$.

5. Conclusions

Well-resolved large-eddy simulations (LES) of a spatially developing turbulent boundary layer under zero pressure gradient up to relatively high Reynolds numbers ($Re_\theta = 4300$) are presented. The employed subgrid-scale model is the ADM-RT model (Schlatter *et al.* 2004), which is an efficient and simple regularisation method based on high-order filters. The (laminar) inflow is located at $Re_{\delta^*} = 450$ ($Re_\theta \approx 200$), a position far enough upstream to ensure a proper flow development further downstream. Results are validated and compared extensively to both numerical data sets (Schlatter et al. 2009) and available experimental measurements, e.g. the ones obtained by Österlund *et al.* (2000).

The LES results are in good agreement with these existing data for both mean and fluctuating quantities, e.g. mean velocity, skin friction and shear stress, budget terms and pressure fluctuations. In addition, spanwise and temporal spectra characterising large-scale flow organisation have been analysed. In particular, the near-wall streaks scaling in inner units and the outer layer large-scale structures can clearly be identified in both spanwise and temporal spectra. The spacing of the near-wall streaks is estimated as 120 plus units in width and about 1000 in length, whereas the dominant large-scale structure is about $0.85\delta_{99}$ wide and persists for about $10\delta_{99}/U_\infty$ time units.

The goal of the present study is to provide reliable numerical data for high Reynolds-number wall-bounded turbulence, which can in turn be employed for further model development and validation, but also to contribute to the further characterisation and understanding of wall turbulence, in particular boundary-layer flows.

The data of the present LES will be made available at `www.mech.kth.se`.

Acknowledgements

Computer time was provided by SNIC (Swedish National Infrastructure for Computing) with a generous grant by the Knut and Alice Wallenberg (KAW)

Foundation. The simulations were run at the Centre for Parallel Computers (PDC) at the Royal Institute of Technology (KTH) and the National Supercomputer Centre (NSC) at Linköping University in Sweden.

References

Abe, H., Kawamura, H. & Choi, H. 2004 Very large-scale structures and their effects on the wall shear-stress fluctuations in a turbulent channel flow up to Re[sub tau] = 640. *ASME J. Fluids Engng.* **126** (5), 835–843.

del Álamo, J. C. & Jiménez, J. 2003 Spectra of the very large anisotropic scales in turbulent channels. *Phys. Fluids* **15** (6), L41–L44.

del Álamo, J. C., Jiménez, J., Zandonade, P. & Moser, R. D. 2004 Scaling of the energy spectra of turbulent channels. *J. Fluid Mech.* **500**, 135–144.

Alfredsson, P. H., Johansson, A. V., Haritonidis, J. H. & Eckelmann, H. 1988 The fluctuating wall-shear stress and the velocity field in the viscous sublayer. *Phys. Fluids* **31** (5), 1026–1033.

Chauhan, K. A., Monkewitz, P. A. & Nagib, H. M. 2009 Criteria for assessing experiments in zero pressure gradient boundary layers. *Fluid Dyn. Res.* **41** (2), 021404.

Chevalier, M., Schlatter, P., Lundbladh, A. & Henningson, D. S. 2007 A pseudo-spectral solver for incompressible boundary layer flows. *Tech. Rep* TRITA-MEK 2007:07. Royal Institute of Technology, Stockholm.

Farabee, T. M. & Casarella, M. J. 1991 Spectral features of wall pressure fluctuations beneath turbulent boundary layers. *Phys. Fluids* **3**, 2410–2420.

Ferrante, A. & Elghobashi, S. 2005 Rreynolds number effect on drag reduction in a microbubble-laden spatially developing turbulent boundary layer. *J. Fluid Mech.* **543**, 93–106.

Guala, M., Hommema, S. E. & Adrian, R. J. 2006 Large-scale and very-large-scale motions in turbulent pipe flow. *J. Fluid Mech.* **554**, 521–542.

Honkan, A. & Andreopoulos, Y. 1997 Vorticity, strain-rate and dissipation characteristics in the near-wall region of turbulent boundary layers. *J. Fluid Mech.* **350**, 29–96.

Hoyas, S. & Jiménez, J. 2006 Scaling of the velocity fluctuations in turbulent channels up to $re_\tau = 2003$. *Phys. Fluids* **18** (011702), 1–4.

Hutchins, N. & Marusic, I. 2007 Evidence of very long meandering features in the logarithmic region of turbulent boundary layers. *J. Fluid Mech.* **579**, 1–28.

Hutchins, N., Nickels, T. B., Marusic, I. & Chong, M. S. 2009 Hot-wire spatial resolution issues in wall-bounded turbulence. *J. Fluid Mech.* In press.

Kays, W. M. & Crawford, M. E. 1993 *Convective Heat and Mass Transfer*, 3rd edn. McGraw-Hill, New York, U.S.A.

Khujadze, G. & Oberlack, M. 2004 DNS and scaling laws from new symmetry groups of ZPG turbulent boundary layer flow. *Theoret. Comput. Fluid Dynamics* **18**, 391–411.

Kim, J., Moin, P. & Moser, R. 1987 Turbulence statistics in fully developed channel flow at low Reynolds number. *J. Fluid Mech.* **177**, 133–166.

Kim, K. C. & Adrian, R. J. 1999 Very large-scale motion in the outer layer. *Phys. Fluids* **11** (2), 417–422.

Kline, S. J., Reynolds, W. C., Schraub, F. A. & Runstadler, P. W. 1967 The structure of turbulent boundary layers. *J. Fluid Mech.* **30**, 741–773.

Komminaho, J. & Skote, M. 2002 Reynolds stress budgets in Couette and boundary layer flows. *Flow, Turbulence Combust.* **68** (2), 167–192.

Li, Q., Schlatter, P., Brandt, L. & Henningson, D. S. 2009 DNS of a spatially developing turbulent boundary layer with passive scalar transport. *Int. J. Heat Fluid Flow* In press.

Li, Q., Schlatter, P. & Henningson, D. S. 2008 Spectral simulations of wall-bounded flows on massively parallel computers. *Tech. Rep*. KTH Mechanics, Stockholm, Sweden.

Lin, J., Laval, J. P., Foucaut, J. M. & Stanislas, M. 2008 Quantitative characterization of coherent structures in the buffer layer of near-wall turbulence. Part 1: streaks. *Exp. Fluids* **45**, 999–1013.

Marusic, I. 2009 Unravelling turbulence near walls. *J. Fluid Mech.* **630**, 1–4.

Metzger, M. M. & Klewicki, J. C. 2001 A comparative study of near-wall turbulence in high and low reynolds number boundary layers. *Phys. Fluids* .

Monkewitz, P. A., Chauhan, K. A. & Nagib, H. M. 2007 Self-consistent high-Reynolds-number asymptotics for zero-pressure-gradient turbulent boundary layers. *Phys. Fluids* **19** (115101), 1–12.

Moser, R. D., Kim, J. & Mansour, N. N. 1999 Direct numerical simulation of turbulent channel flow up to $Re_\tau = 590$. *Phys. Fluids* **11** (4), 943–945.

Nordström, J., Nordin, N. & Henningson, D. S. 1999 The fringe region technique and the Fourier method used in the Direct Numerical Simulation of spatially evolving viscous flows. *SIAM J. Sci. Comp.* **20** (4), 1365–1393.

Örlü, R. 2009 Experimental studies in jet flows and zero pressure-gradient turbulent boundary layers. PhD thesis, Department of Mechanics, KTH, Stockholm, Sweden.

Österlund, J. M. 1999 Experimental studies of zero pressure-gradient turbulent boundary layer flow. PhD thesis, Department of Mechanics, KTH, Stockholm, Sweden.

Österlund, J. M., Johansson, A. V., Nagib, H. M. & Hites, M. H. 2000 A note on the overlap region in turbulent boundary layers. *Phys. Fluids* **12** (1), 1–4.

Pope, S. B. 2000 *Turbulent Flows*. Cambridge University Press, Cambridge, U.K.

Quadrio, M. & Luchini, P. 2003 Integral space–time scales in turbulent wall flows. *Phys. Fluids* **15** (8), 2219–2227.

Sagaut, P. 2005 *Large Eddy Simulation for Incompressible Flows, An Introduction*, 3rd edn. Springer, Berlin, Germany.

Schlatter, P. & Brandt, L. 2008 DNS of three-dimensional turbulent boundary layers. In *Direct and Large-Eddy Simulation VII*. To appear.

Schlatter, P., Örlü, R., Li, Q., Brethouwer, G., Fransson, J. H. M., Johansson, A. V., Alfredsson, P. H. & Henningson, D. S. 2009 Turbulent boundary layers up to $Re_\theta = 2500$ studied through numerical simulation and experiments. *Phys. Fluids* **21** (5), 051702.

Schlatter, P., Stolz, S. & Kleiser, L. 2004 LES of transitional flows using the approximate deconvolution model. *Int. J. Heat Fluid Flow* **25** (3), 549–558.

Schlatter, P., Stolz, S. & Kleiser, L. 2006 LES of spatial transition in plane channel flow. *J. Turbulence* **7** (33), 1–24.

Spalart, P. R. 1988 Direct simulation of a turbulent boundary layer up to $Re_\theta = 1410$. *J. Fluid Mech.* **187**, 61–98.

Tsuji, Y., Fransson, J. H. M., Alfredsson, P. H. & Johansson, A. V. 2007 Pressure statistics and their scaling in high-Reynolds-number turbulent boundary layer. *J. Fluid Mech.* **585**, 1–40.

Wu, X. & Moin, P. 2009 Direct numerical simulation of turbulence in a nominally zero-pressure-gradient flat-plate boundary layer. *J. Fluid Mech.* **630**, 5–41.

Paper 4

4

Direct numerical simulation of a spatially developing turbulent boundary layer with passive scalar transport

By Qiang Li, Philipp Schlatter, Luca Brandt, & Dan S. Henningson

Linné Flow Centre, KTH Mechanics
SE-100 44 Stockholm, Sweden

Int. J. Heat Fluid Flows in Press

A direct numerical simulation (DNS) of a spatially developing turbulent boundary layer over a flat plate under zero pressure gradient (ZPG) has been carried out. The evolution of several passive scalars with both isoscalar and isoflux wall boundary condition are computed during the simulation. The Navier-Stokes equations as well as the scalar transport equation are solved using a fully spectral method. The highest Reynolds number based on the free-stream velocity U_∞ and momentum thickness θ is $Re_\theta = 830$, and the molecular Prandtl numbers are 0.2, 0.71 and 2. To the authors' knowledge, this Reynolds number is to date the highest with such a variety of scalars. A large number of turbulence statistics for both flow and scalar fields are obtained and compared when possible to existing experimental and numerical simulations at comparable Reynolds number. The main focus of the present paper is on the statistical behaviour of the scalars in the outer region of the boundary layer, distinctly different from the channel-flow simulations. Agreements as well as discrepancies are discussed while the influence of the molecular Prandtl number and wall boundary conditions is also highlighted. A Pr scaling for various quantities is proposed in outer scalings. In addition, spanwise two-point correlation and instantaneous fields are employed to investigate the near-wall streak spacing and the coherence between the velocity and the scalar fields. Probability density functions (PDF) and joint probability density functions (JPDF) are shown to identify the intermittency both near the wall and in the outer region of the boundary layer. The present simulation data will be available online for the research community.

Nomenclature

c_p specific scalar capacity
h channel half width
H_{12} shape factor

k scalar conductivity
p pressure
Pe Péclet number $= RePr$
Pr molecular Prandtl number or Schmidt number $= \frac{\nu}{\alpha}$
Pr_t turbulent Prandtl number
q_w rate of the scalar transfer from the wall to the flow $= -k\frac{\partial\theta}{\partial y}\big|_{y=0}$
Re Reynolds number
$Re_{\delta_0^*}$ Reynolds number based on the inlet displacement thickness δ_0^*
Re_θ Reynolds number based on the momentum thickness θ
Re_τ Reynolds number based on the friction velocity u_τ
St Stanton number $= \frac{q_w}{\rho U_\infty c_p(\theta_w-\theta_\infty)}$
t time
u_i, u, v, w instantaneous velocity components in the streamwise, wall-normal and spanwise direction (in direction i)
u_τ friction velocity $= \sqrt{\frac{\tau_w}{\rho}}$
U_∞ free-stream mean velocity
x_i, x, y, z Cartesian coordinates in the streamwise, wall-normal and spanwise direction (in direction i)
y_L height of the domain
$\mathcal{O}$ Landau symbol (order of)
$\mathcal{P}$ production of turbulent energy
$\mathcal{U}_i$ Blasius laminar base flow

subscript
f properties of the fluid
w properties at the wall
∞ properties in the free stream
rms root-mean-square value of the quantity

superscript
$\hat{}$ dimensional term for the variable quantity
$'$ fluctuating part
$+$ scaling in viscous (wall) units
out scaling in outer units
$\langle\rangle$ average over time and the homogeneous direction

Greek symbols
α scalar diffusivity $= \frac{k}{\rho c_p}$
α_t eddy diffusivity $= -\frac{\langle v'\theta'\rangle}{\frac{\partial\langle\theta\rangle}{\partial y}}$
β pressure gradient coefficient $= \frac{\delta^*}{\tau_w}\frac{\mathrm{d}p}{\mathrm{d}x}\big|_{free-stream}$
δ^* displacement thickness
δ_0^* inlet displacement thickness
δ_θ^{99} 99% local scalar boundary-layer thickness

ε dissipation of turbulent energy
Ξ log-law diagnostic function
Ξ_θ log-law diagnostic function for scalar
θ momentum thickness
θ scalar
θ_i scalar i
θ_τ friction scalar $= \frac{q_w}{\rho c_p u_\tau}$
θ_w scalar concentration at the wall
θ_∞ scalar concentration in the free stream
κ von Kármán constant
κ_θ von Kármán constant for the scalar
λ fringe function
λ streak spacing
ν kinematic viscosity $= \frac{\mu}{\rho}$
ν_t turbulent eddy viscosity $= -\frac{\langle u'v' \rangle}{\frac{\partial \langle u \rangle}{\partial y}}$
ρ density
τ_w shear stress at the wall

1. Introduction

The understanding of the spreading of a passive scalar in turbulent flows was initially gained solely through wind tunnel experiments. The early studies of heat transfer were performed by e.g. Corrsin (1952), Warhaft and Lumley (1978) in grid-generated turbulence and homogeneous turbulence. Hishida and Nagano (1979) and Nagano and Tagawa (1988) measured various types of moments of velocity and scalar fluctuations in fully developed pipe flow to investigate the transport mechanism in turbulence and to correlate the transfer processes of momentum and scalar with coherent motions. In particular, the importance of the coherent motions in the turbulent diffusion process of Reynolds-stress components and scalar-fluxes was demonstrated for the first time. Later, Mosyak et al. (2001) and Hetsroni et al. (2001) carried out experiments to study the wall-temperature fluctuations under different wall-boundary conditions and the thermal coherent structure in a fully developed channel flow. For turbulent boundary-layer flows, Perry and Hoffmann (1976) examined the similarity between the Reynolds shear stress $\langle u'v' \rangle$ and scalar flux $\langle v'\theta' \rangle$ using quadrant analysis. However, the Reynolds stress $\langle u'v' \rangle$ was analysed in the (u, v) plane and the turbulent scalar flux $\langle v'\theta' \rangle$ in the (v, θ) plane. Therefore the correspondence between fluids motions and scalar transport was not strictly specified. Subramanian and Antonia (1981) measured several quantities in a slightly heated boundary layer to address the effect of Reynolds number. Krishnamoorthy and Antonia (1987) and Antonia et al. (1988) investigated the temperature dissipation and the correlation between the longitudinal velocity fluctuation and temperature fluctuation in the near-wall region.

Due to the rapid progress in high-performance computers, direct numerical simulation (DNS) of turbulent flows involving passive scalars, especially in channel geometry, has matured to an important research tool during the past few decades. The first direct numerical simulations of passive scalar transport were performed by Rogers et al. (1986) in a homogeneous shear flow. Numerical simulations in channel geometry were pioneered by Kim and Moin (1989) with $Pr = 0.1$, 0.71 and 2.0 at $Re_\tau = 180$ where Re_τ is the Reynolds number based on the friction velocity u_τ and the channel half width h and Pr is the molecular Prandtl number. Heat is introduced by an internal source created and removed from both walls. A high correlation between the streamwise velocity and temperature was found in the wall region. Later, Kasagi et al. (1992) and Kasagi and Ohtsubo (1993) performed DNS at $Re_\tau = 150$ with $Pr = 0.71$ and 0.025. The scalar-fluxes budgets were shown and the low Pr number effects were discussed. However, the Reynolds number of these simulations still remains at a low value. Wikström (1998) performed a DNS at a higher Reynolds number of $Re_\tau = 265$ with $Pr = 0.71$. Abe et al. (2004) reached up to $Re_\tau = 1020$ and $Pr = 0.025$ and 0.71. All these simulations are done, however, with a Prandtl number lower than two. This is due to the fact that the smallest scales in the scalar fluctuation decrease with the increase of Pr. Therefore the DNS becomes an even more difficult task when the Prandtl number is high. With the help of larger parallel computers, Kawamura et al. (1998) performed the DNS in periodic channel flow at $Re_\tau = 180$ but for a wider range of Pr from 0.025 to 5.0. Later, Tiselj et al. (2001) performed a channel DNS at $Re_\tau = 150$ with Pr from 0.71 to 7. In his work, the ideal isoflux boundary condition was compared to the previous results and underestimated values for the wall-temperature fluctuations of the previous simulations were reported. Recently, Redjem-Saad et al. (2007) performed a DNS in a fully turbulent pipe flow to explore the impact of the wall curvature on the turbulent heat transfer. The Reynolds number based on the pipe radius is 5500 ($Re_\tau = 186$) and the Pr varies from 0.026 to 1. For pipe flows, slightly more intense temperature fluctuations than in channel flow were found.

However, for flat-plate boundary layers with zero pressure gradient (ZPG), which is a relevant canonical flow case for theoretical, numerical as well as experimental studies, relatively few numerical results have been published for medium or high Reynolds numbers. The direct numerical simulation by Spalart (1988) using an innovative spatio-temporal approach provided valuable data at $Re_\theta = 300, 670, 1410$. Later, Komminaho and Skote (2002) performed a true spatial DNS up to $Re_\theta = 700$. Concerning boundary-layer simulations with passive scalars, to our knowledge the first DNS was performed by Bell and Ferziger (1993) up to a medium Reynolds number of $Re_\theta = 700$ with Pr being $0.1, 0.71$ and 2.0. Later, a DNS was performed by Kong et al. (2000) up to a lower Reynolds number of $Re_\theta = 420$ and $Pr = 0.71$ with isothermal and isoflux boundary conditions. Recently, Hattori et al. (2007) performed a DNS to study the buoyancy effects on the boundary layer starting from Reynolds number of $Re_\theta = 1000$ to $Re_\theta = 1200$ and $Pr = 0.71$. A new DNS was

performed by Tohdoh et al. (2008) up to a low Reynolds number of $Re_\theta = 420$, with $Pr = 0.71$ and 2.0.

This paper is a study of passive scalar transport in a turbulent boundary layer spatially developing over a flat plate with zero pressure gradient (ZPG). The investigation is performed using direct numerical simulation (DNS). A spatial formulation (inflow/outflow setting) was adopted since it is the best model for a boundary layer which grows in the downstream direction rather than in time. Moreover, all the scalars were simulated simultaneously, i.e. one velocity field accommodates all the scalars. The Reynolds number $Re_{\delta_0^*}$ based on the free-stream velocity U_∞ and the inlet displacement thickness δ_0^* is 450 and Prandtl number Pr are chosen to be 0.2, 0.71 and 2.0. Isoscalar and isoflux wall boundary conditions are employed for comparison. Since similarities exist between the boundary layer and channel flow in the near-wall region, this study mainly focuses on the outer region of the boundary layer, i.e. the wake region. Based on the present data, the scalings based on the Prandtl number are also proposed for various scalar quantities and also for the budgets of the scalar fluxes in both inner and outer units. The goal of this paper is to extend our knowledge about the scalar transport in turbulent boundary-layer flows to a wider range of both Reynolds number and Prandtl numbers. In addition, a data base for the research community is generated, which can be useful in particular for modelling purposes.

2. Numerical methodology

2.1. *Governing equations & numerical method*

The three-dimensional, time-dependent Navier-Stokes equations for incompressible flow as well as the transport equation for the passive scalar in non-dimensional form using the summation convention are given by

$$\frac{\partial u_i}{\partial x_i} = 0 \ , \tag{1}$$

$$\frac{\partial u_i}{\partial t} + u_j \frac{\partial u_i}{\partial x_j} = -\frac{\partial p}{\partial x_i} + \frac{1}{Re_{\delta_0^*}} \frac{\partial^2 u_i}{\partial x_j \partial x_j} \ , \tag{2}$$

$$\frac{\partial \theta}{\partial t} + u_i \frac{\partial \theta}{\partial x_i} = \frac{1}{Re_{\delta_0^*} Pr} \frac{\partial^2 \theta}{\partial x_i \partial x_i} = \frac{1}{Pe} \frac{\partial^2 \theta}{\partial x_i \partial x_i} \ , \tag{3}$$

where $(x_1, x_2, x_3) = (x, y, z)$ are the Cartesian coordinates in the streamwise, wall-normal and spanwise direction, respectively. $(u_1, u_2, u_3) = (u, v, w)$ are the corresponding instantaneous velocity components, t represents the time, p is the pressure and θ the scalar quantity. The Reynolds number $Re_{\delta_0^*}$ is based on the free-stream velocity U_∞ and the inlet displacement thickness δ_0^* while Pr denotes the molecular Prandtl (or Schmidt) number and $Pe = Re_{\delta_0^*} Pr$ for the Péclet number.

In the present paper, the dimensional variables are non-dimensionalised as in Kong et al. (2000), i.e.

$$u_i = \frac{\hat{u}_i}{U_\infty}, \qquad x_i = \frac{\hat{x}_i}{\delta_0^*},\ p = \frac{\hat{p}}{\rho U_\infty^2},\ t = \frac{U_\infty \hat{t}}{\delta_0^*}, \tag{4}$$

$$\theta = \frac{\theta_w - \hat{\theta}}{\theta_w - \theta_\infty}\ , \qquad \text{for the isoscalar boundary condition,} \tag{5}$$

$$\theta = 1 - \frac{k(\hat{\theta} - \theta_\infty)}{q_w \delta_0^*}\ , \qquad \text{for the isoflux boundary condition.} \tag{6}$$

The dimensional reference quantities are defined as follows. U_∞ is the free-stream velocity, δ_0^* the inlet displacement thickness, ρ the density, k the scalar conductivity, q_w the scalar flux at the wall, θ_w the scalar concentration on the wall and θ_∞ the scalar concentration in the free stream. The hat $\hat{}$ denotes the dimensional term for the variable quantities, i.e. u_i, x_i, p, t and θ.

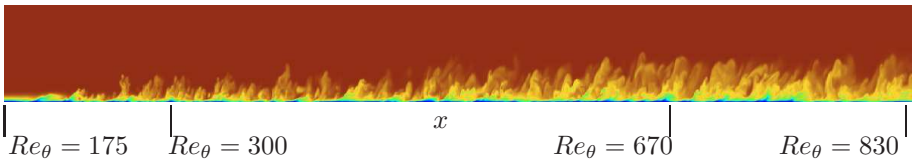

FIGURE 1. Instantaneous contour plot of the fluctuating scalar field in a $x - y$ plane, starting from $Re_\theta = 175$ to $Re_\theta = 850$. Note that the fringe region is not shown in the figure. The box height is enlarged by a factor of 2.

The simulation code (Chevalier et al. 2007) used in the present study employs a pseudo-spectral method comparable to that used by Kim et al. (1987). Fourier series expansion is used in streamwise and spanwise directions (wall-parallel directions) assuming periodic boundary conditions. In the wall-normal direction, Chebyshev expansions employing the Chebyshev-tau method are used. The time advancement uses a four-step third-order Runge-Kutta scheme for the nonlinear terms and a second-order Crank-Nicolson scheme for the linear terms. The nonlinear terms are calculated in physical space to avoid convolution sums. Aliasing errors are removed by using the 3/2-rule in the wall-parallel directions. Figure 1 shows the computational box together with a contour plot of an instantaneous scalar fluctuation. To fulfil the periodic boundary conditions in the streamwise direction, a "fringe region" (Bertolotti et al. 1992) is added at the downstream end of the domain. It is implemented by adding a volume force F_i to the Navier–Stokes equations. The force is of the form

$$F_i = \lambda(x)(\mathcal{U}_i - u_i) \tag{7}$$

with $\mathcal{U}_i$ being the desired inflow condition. Note that the fringe forcing is also applied for the scalar field in a similar fashion. The fringe function $\lambda(x)$ which

has continuous derivatives of all orders has a prescribed shape to minimise the upstream influence (Nordström et al. 1999) and is non-zero only in the fringe region. In the fringe region, the outflow is forced by the volume force to the laminar inflow condition which is a Blasius boundary-layer profile. In addition, to trigger rapid (natural) laminar-turbulent transition, a random volume forcing located at a short distance downstream of the inlet ($x = 10, Re_x = 72950$) is used. The trip forcing can be used to generate noise at low amplitude or turbulence. The volume force is directed normal to the wall with a steady amplitude and a time dependent amplitude. The generated noise has a uniform distribution covering all the frequencies lower than the cutoff frequency corresponding to $\frac{\pi}{2}$ in the present DNS. The turbulent field generated by the trip force leads to very good quality at the expense of a slightly enlarged transitional inflow region. In particular, there are no streamwise correlations in the fluctuations as opposed to e.g. the rescaling and recycling method employed by Kong et al. (2000).

2.2. *Boundary condition*

The velocity and scalar fields are periodic in the horizontal directions while boundary conditions at the wall and in the free-stream are needed to solve the governing equations.

At the solid wall, the no-slip boundary conditions for the velocities

$$u|_{y=0} = 0,\ v|_{y=0} = 0,\ w|_{y=0} = 0,\ \frac{\partial v}{\partial y}\Big|_{y=0} = 0\ , \tag{8}$$

are applied. For the boundary conditions in the free-stream, a Neumann condition, i.e.

$$\frac{\partial u_i}{\partial y}\Big|_{y=y_L} = \frac{\partial \mathcal{U}_i}{\partial y}\Big|_{y=y_L} \tag{9}$$

is imposed with y_L being the height of the domain and $\mathcal{U}_i(x, y)$ the Blasius laminar base flow.

In the present implementation for the scalar field, two types of wall-boundary conditions are available. Similar to those used by Kong et al. (2000), one is an isoscalar wall and the other an isoflux wall. These two kinds of wall boundary conditions are given by

$$\theta|_{y=0} = 0\ , \qquad \text{for the isoscalar boundary condition,} \tag{10}$$

$$\frac{\partial \theta}{\partial y}\Big|_{y=0} = 1\ , \qquad \text{for the isoflux boundary condition.} \tag{11}$$

They corresponds to two limiting cases of the physical configuration (Tiselj et al. 2001), i.e. the scalar activity ratio being 0 for an isoscalar wall and ∞ for an isoflux wall where the scalar activity ratio is defined as $\sqrt{\rho_f c_{pf} k_f / \rho_w c_{pw} k_w}$ with ρ, c_p and k being density, scalar capacity and conductivity, respectively. The subscript f corresponds to the properties of the fluid where subscript w corresponds to the ones of the wall. For the boundary condition in the free-stream, a Dirichlet condition is imposed. A Neumann condition was also tested

and the results turned out to be indistinguishable to those obtained with the Dirichlet condition. The boundary condition in the free-stream thus reads

$$\theta\big|_{y=y_L} = 1 \ . \tag{12}$$

2.3. *Simulation parameters*

The computational box has a dimension of $750\delta_0^* \times 40\delta_0^* \times 34\delta_0^*$ in the streamwise, wall-normal and spanwise directions, respectively. The corresponding resolution is $1024 \times 289 \times 128$ which gives a grid spacing of 17, 0.025–4.6 and 6.3 (in viscous units and based on the friction velocity at the $x = 150$ or $Re_\theta = 400$) in the three directions. The Reynolds number based on the free-stream velocity U_∞ and momentum thickness θ at the inlet is $Re_\theta = 175$ and $Re_\theta = 830$ at the outlet. A comparison of the wall-normal resolution with the corresponding Kolmogorov and Batchelor scales for $Pr = 2.0$ is shown in Figure 2. It can be concluded that a sufficient amount of grid points is used in the wall-normal direction.

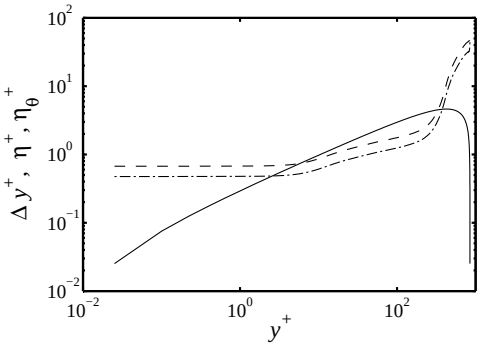

FIGURE 2. Resolution check. ——Wall-normal resolution Δy^+, – – –Kolmogorov scale η^+, –·–Batchelor scale ${\eta_\theta}^+$ for $Pr = 2.0$.

A summary of the molecular Prandtl number together with the wall boundary condition and the boundary-layer thickness, based on the 99% thickness, for all the scalars is listed in Table 1.

All results presented unless specified are averaged results. The average, denoted by the angular brackets, was performed over both time and the homogeneous spanwise direction. The corresponding fluctuating part is denoted by a prime. The averaging time after the initial transient is about 12000 time units ($\frac{\delta_0^*}{U_\infty}$) corresponding to $t^+ = 13500$ in viscous units to make sure that all the statistics are sufficiently converged.

scalar no.	θ_1	θ_2	θ_3	θ_4	θ_5
wall boundary condition	isoscalar	isoscalar	isoflux	isoscalar	isoflux
Prandtl number Pr	0.2	0.71	0.71	2.0	2.0
boundary-layer thickness δ_{99}^+	365	340	340	320	320

TABLE 1. Parameters for the scalars. Note that the boundary-layer thicknesses δ_{99}^+ are in viscous units and measured at $Re_\theta = 830$. The corresponding velocity boundary-layer thickness is about $\delta_{99}^+ = 315$ at $Re_\theta = 830$.

3. Results

The present paper is focused on the results pertaining to the scalar transport. In the interest of space, only one representative result of the mean velocity profile compared with other DNS data is shown, other hydrodynamic results (stresses, budgets etc.) are not shown here. However, these hydrodynamic results were carefully validated and compared with other available numerical and experimental results and the agreements are very good in general, see Li *et al.* (2008).

3.1. *Spatial evolution & flow quality*

The shape factor H_{12}, defined as the ratio between the displacement thickness δ^* and the momentum thickness θ, provides a direct assessment of the flow field. As seen in Figure 3 (a), a slow decrease of H_{12} with the increase of the Reynolds number in the turbulent region is observed and the agreement with the experimental data is good in the fully turbulent region close to the outlet, $Re_\theta = 830, H_{12} = 1.49$. The variation of the ratio of the integrated turbulent kinetic energy production $\mathcal{P}$ and dissipation ε along the streamwise direction is shown in Figure 3 (b). Based on this figure, the range of Reynolds number in which the boundary layer can be assumed to be in equilibrium is for the present DNS from about $Re_\theta = 350$ to 830.

The non-dimensional parameter β related to the pressure gradient is defined as

$$\beta = \frac{\delta^*}{\tau_w} \frac{\mathrm{d}p}{\mathrm{d}x}\Big|_{free-stream} , \tag{13}$$

where δ^* is the displacement thickness and τ_w is the shear stress at the wall. The β calculated from the simulation is of $\mathcal{O}(10^{-9})$ indicating that the flow far away from the wall is indeed subjected to zero pressure gradient.

Österlund et al. (1999) suggested a turbulent correlation for the skin-friction coefficient which reads,

$$c_f = 2\left(\frac{1}{0.384}\ln Re_\theta + 3.75\right)^{-2} . \tag{14}$$

The present results of the skin-friction coefficient compare well with this correlation even at comparably low Reynolds numbers.

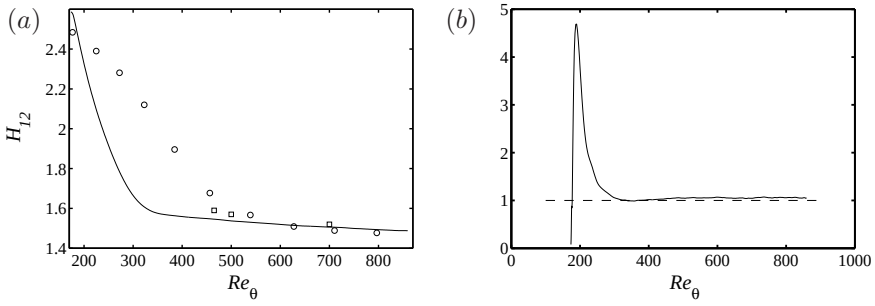

FIGURE 3. Streamwise evolution of the shape factor H_{12} and the ratio of the wall-normal integrated turbulent kinetic energy production $\mathcal{P}$ and dissipation ε. ——Present DNS, ∘ T3A Roach and Brierley (1992), ▫Purtell et al. (1981). (a) Shape factor H_{12}, (b) $\frac{\int_0^\infty \mathcal{P}\mathrm{d}y}{\int_0^\infty \varepsilon \mathrm{d}y}$.

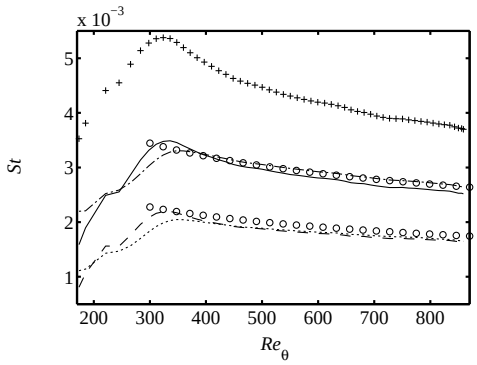

FIGURE 4. Streamwise evolution of the Stanton number St. + θ_1, ——θ_2, –·–θ_3, – – –θ_4, ····· θ_5, ∘ Kays and Crawford (1993).

The Stanton number St for a scalar boundary layer is the counterpart of the skin-friction coefficient for a momentum boundary layer. This non-dimensional scalar-transfer coefficient is defined by

$$St = \frac{q_w}{\rho U_\infty c_p(\theta_w - \theta_\infty)} \ , \tag{15}$$

where q_w is the rate of the scalar transfer from the wall to the flow, ρ is the density of the fluid, U_∞ is the free-stream velocity, c_p is the specific scalar, and θ_w and θ_∞ are the scalar concentrations at the wall and in the free-stream, respectively. The variations of the Stanton number with different downstream positions are shown in Figure 4. The turbulent correlation according to Kays

and Crawford (1993) which reads

$$St = 0.0125 Pr^{-\frac{2}{5}} Re_\theta^{-\frac{1}{4}} , \qquad Pr > 0.5 , \tag{16}$$

is included for comparison. The difference might be related to the fact that the correlations suggested by Kays and Crawford (1993) are for high Reynolds numbers. An overshoot of the peak is observed which also exists in the profile of the skin-friction coefficient, see e.g. Brandt *et al.* (2004). The overshoot is consistent with the general behaviour of spectral methods applied to transitional flows and it is slightly diminished with increased resolution. It is observed that the overshoot vanishes for the scalars with isoflux wall boundary condition.

3.2. *Instantaneous fields*

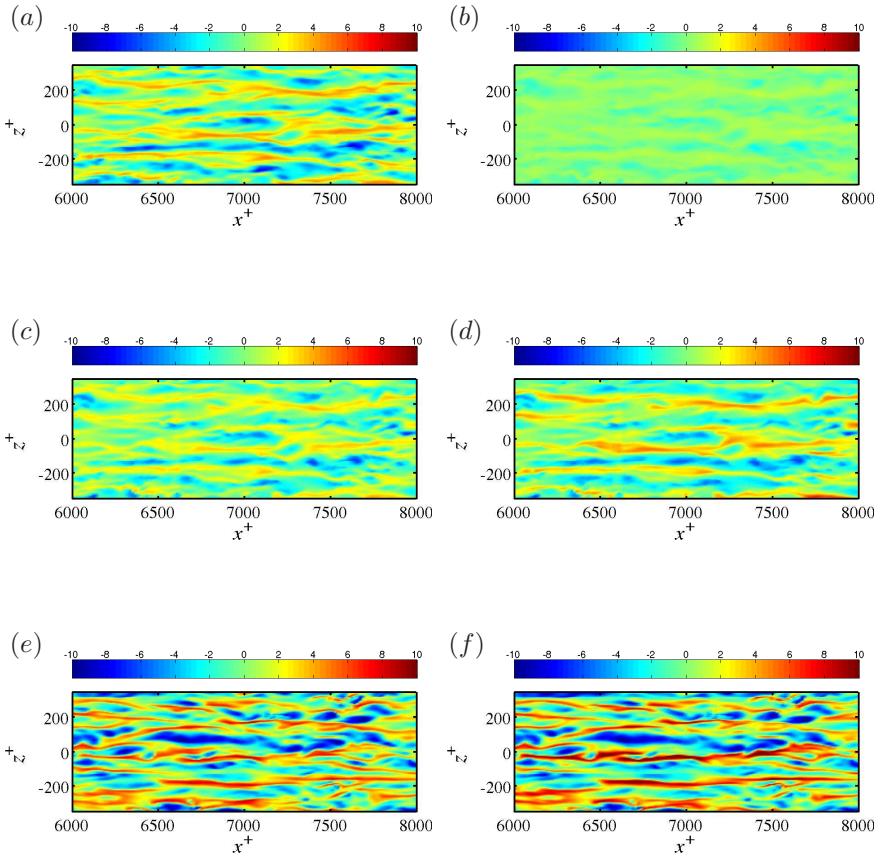

FIGURE 5. Instantaneous flow and scalar fields at $y^+ \approx 7$. (a) u'^+, (b) ${\theta'_1}^+$, (c) ${\theta'_2}^+$, (d) ${\theta'_3}^+$, (e) ${\theta'_4}^+$, (f) ${\theta'_5}^+$.

Figure 5 shows the instantaneous streamwise disturbance velocity at $y^+ \approx 7$ in the (x, z) plane as well as the corresponding scalar fluctuations. All the plots are obtained at the same time instant, and the visualised box is centred around $Re_\theta = 625$ and has a length of $\Delta x^+ = 2000$ and width of $\Delta z^+ = 700$ in viscous units. The viscous unit is defined by the friction velocity u_τ at the centre of the domain, i.e. $x = 350$, $Re_x = 189500$ and $Re_\theta = 625$. Streaky structures are clearly observed and a strong similarity exists between the velocity field and the scalar field, mainly $Pr = 0.71$. The regions of low and high scalar concentrations are elongated in the streamwise direction with a mean spanwise spacing similar to that of the streamwise velocity fluctuation. Finer structures with stronger spanwise and wall-normal gradients are observed with increasing Pr. In the case of the isoflux wall boundary condition, a clear difference can be observed: The scalar fluctuations are enhanced by the isoflux boundary condition in contrast to the ones with isoscalar boundary condition. It is also consistent with previous work by e.g. Kong et al. (2000) that the low-speed fluids are associated with low scalar concentration region and high-speed fluids with high scalar concentration region.

3.3. *Mean results & turbulence intensities*

For the mean profile and fluctuations of the velocity field, good agreements are observed with the DNS data from Spalart (1988) and the DNS data from Komminaho and Skote (2002) as seen in Figure 6. A small deviation can be observed for the mean streamwise velocity profile when comparing to Spalart (1988). This is probably due to the temporal approach used for the latter simulation and is also seen in other boundary-layer simulations, e.g. Schlatter et al. (2009). The von Kármán constant κ used in the log-law is 0.41 and it gives good agreement for this comparably low Reynolds number. The log-law

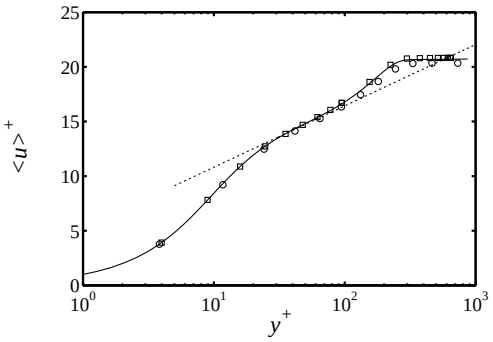

FIGURE 6. Comparison of the mean streamwise velocity $\langle u \rangle^+$ with other numerical simulations. ——— Present DNS at $Re_\theta = 670$, ∘ Spalart (1988) at $Re_\theta = 670$, □ Komminaho and Skote (2002) at $Re_\theta = 670$, ····· $\langle u \rangle^+ = \frac{1}{\kappa} \ln y^+ + 5.2$ with $\kappa = 0.41$.

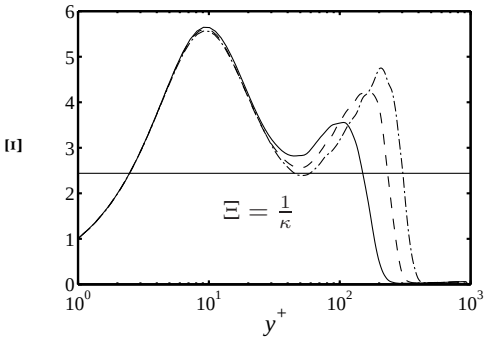

FIGURE 7. Profile of the mean velocity and the diagnostic function Ξ at different Reynolds numbers. ——— at $Re_\theta = 390$, - - - at $Re_\theta = 620$, -·-· at $Re_\theta = 830$, $\kappa = 0.41$.

diagnostic function $\Xi = y^+ \frac{\mathrm{d}<u>^+}{\mathrm{d}y^+}$ is plotted in Figure 7. This sensitive function Ξ is supposed to approach a constant value of the inverse von Kármán constant $\frac{1}{\kappa}$ in the overlap region according to the log-law (Nagib et al. 2007). As seen from the plot, the present DNS does not yet have a well developed logarithmic overlap region due to the comparably low Reynolds number.

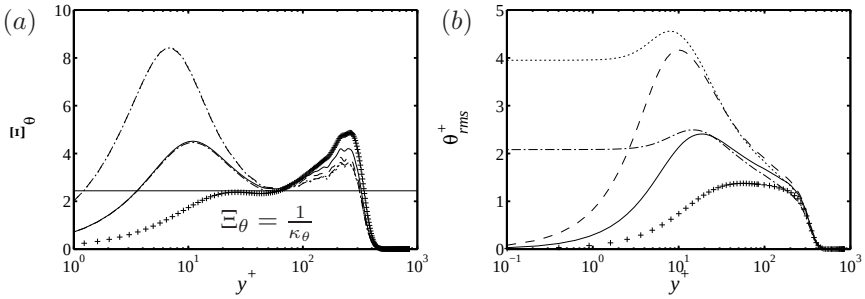

FIGURE 8. Profiles of the diagnostic function Ξ_θ with $\kappa_\theta = 0.41$ and scalar variance θ^+_{rms} at $Re_\theta = 830$. + θ_1, ——— θ_2, -·-· θ_3, - - - θ_4, ····· θ_5. Isoscalar wall: θ_1, θ_2 and θ_4. Isoflux wall: θ_3 and θ_5. (*a*) Ξ_θ, (*b*) θ^+_{rms}.

The von Kármán constant for the mean scalar distributions κ_θ, is assumed to be independent of the Prandtl number and the Reynolds number in the logarithmic region. Similar to the diagnostic function for the velocity field, a constant log-law diagnostic function for scalar fields Ξ_θ, defined as $y^+ \frac{\mathrm{d}<\theta>^+}{\mathrm{d}y^+}$, is plotted in Figure 8 (*a*). The present κ_θ is chosen to be 0.41 which is close to the channel-flow results by Kawamura et al. (1999) of about 0.4 but smaller than 0.47 suggested by Kader (1981).

The root-mean-square (RMS) of the fluctuations for different scalars are shown in Figure 8 (b) which clearly demonstrates the effects of the different boundary conditions. The data with isoscalar boundary condition go to zero as the wall is approached whereas the cases with isoflux boundary condition remain finite. Far away from the wall, the profiles of the RMS of the scalar fluctuations with different wall boundary conditions collapse with each other indicating that the influence from the boundary conditions is only confined to the near-wall region. The limiting value of the scalar variance for θ_3 ($Pr = 0.71$) with isoflux boundary condition was reported to be 2.0 and independent of the Reynolds number by Kong et al. (2000). However, having a higher Reynolds number range for the present DNS, a slight increase of the limiting wall value for increasing Reynolds number was observed for both θ_3 and θ_5, roughly following $Re_\theta^{0.1}$. For example, a value of 2.12 at $Re_\theta = 850$ was found for θ_3 ($Pr = 0.71$). However, to what extent this growth continues for high Reynolds number is still unclear due to the limited maximum Re_θ in the present study. Comparing the wall RMS values for θ_3 ($Pr = 0.71$) and θ_5 ($Pr = 2.0$), one can find that they roughly scale as $Pr^{0.6}$ over the present Reynolds number range. It is also noticeable that the maximum RMS values of the scalar fluctuation increase as Pr is increasing. The peak values of the RMS of the scalar fluctuations at $Pr = 2.0$ are about twice as those at $Pr = 0.71$. It is also observed that the peak position moves away from the wall as Pr is decreased. The present DNS results agree well with various results from Kader (1981), Kasagi et al. (1992) and Kawamura et al. (1998) for both the mean profile and the RMS of the scalar fluctuation in the near-wall region.

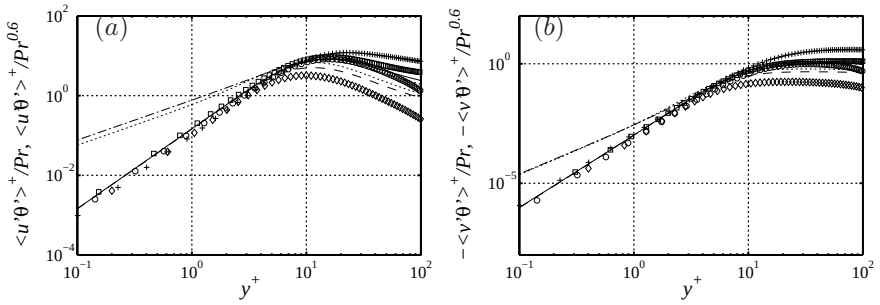

FIGURE 9. Profiles of the scalar fluxes $\langle u'\theta'\rangle$ and $-\langle v'\theta'\rangle$ at $Re_\theta = 830$. + θ_1, ——θ_2, –·–θ_3, – – –θ_4, ·····θ_5. Isoscalar wall: $\theta_1, Pr = 0.2$, $\theta_2, Pr = 0.71$ and $\theta_4, Pr = 2.0$. Isoflux wall: $\theta_3, Pr = 0.71$ and $\theta_5, Pr = 2.0$. ∘ Kasagi et al. (1992) at $Re_\tau = 150, Pr = 0.71$, □ Abe et al. (2004) at $Re_\tau = 1020, Pr = 0.71$, ◇ Kawamura et al. (1998) at $Re_\tau = 180, Pr = 5.0$. (a) $\langle u'\theta'\rangle^+$, ($b$) $-\langle v'\theta'\rangle^+$.

The previous study by Kawamura et al. (1998) reported that in the vicinity of the wall for isoscalar boundary condition, $\langle\theta\rangle^+$ and θ^+_{rms} are proportional to Pry^+ while $\langle u'\theta'\rangle^+$ and $-\langle v'\theta'\rangle^+$ vary as Pry^{+2} and Pry^{+3}, respectively, except for low Pr. This is also true for the present DNS (see Figure 9) and for the turbulent pipe-flow simulation by Redjem-Saad et al. (2007). For scalars with isoflux boundary condition, using the above exponent for the wall fluctuations, θ^+_{rms} is found proportional to $Pr^{0.6}y^+$ in the vicinity of the wall while the scaling for the mean scalar profile remains the same as for the isoscalar case. For the streamwise and wall-normal scalar fluxes, Kong et al. (2000) concluded that $\langle u'\theta'\rangle^+$ and $-\langle v'\theta'\rangle^+$ are proportional to y^+ and y^{+2}, respectively, based on near-wall asymptotic expansion of u', v' and θ'. Since only one scalar with isoflux wall was computed in their simulation, the relation with Pr is not clear. Based on the present data, $\langle u'\theta'\rangle^+$ and $-\langle v'\theta'\rangle^+$ with isoflux boundary condition vary as $Pr^{0.6}y^+$ and $Pr^{0.6}y^{+2}$, respectively.

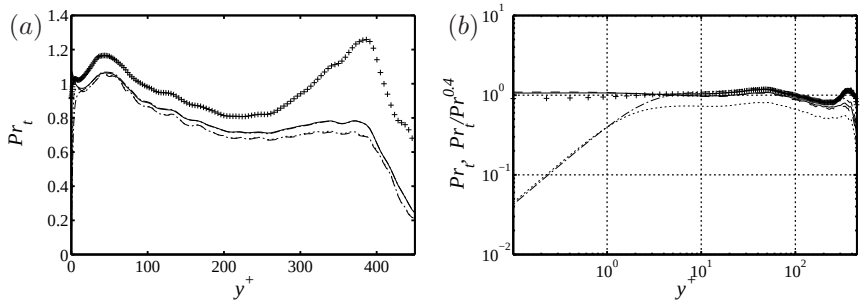

FIGURE 10. The wall-normal distribution of the turbulent Prandtl number Pr_t at $Re_\theta = 830$. + θ_1, ——θ_2, –·–θ_3, – – –θ_4, ····· θ_5. The boundary-layer thickness are ranging from $y^+ = 320$ to $y^+ = 365$ for different scalars.

An important parameter in scalar transfer is the turbulent Prandtl number Pr_t which is defined as the ratio of the turbulent eddy viscosity ν_t to the eddy diffusivity α_t. ν_t and α_t are defined by

$$\nu_t = -\frac{\langle u'v'\rangle}{\frac{\partial\langle u\rangle}{\partial y}} \tag{17}$$

and

$$\alpha_t = -\frac{\langle v'\theta'\rangle}{\frac{\partial\langle\theta\rangle}{\partial y}}\ , \tag{18}$$

respectively. The turbulent Prandtl number (see Figure 10) is often assumed to be a constant value which is independent of the wall-normal distance and the molecular Prandtl number. However, the dependence on the wall-normal position and Pr has long been a subject of many investigations, e.g. Antonia and Kim (1991). For the present DNS, Pr_t for the scalars θ_2 and θ_4 (isoscalar

boundary condition) approach approximately a constant value of about 1.1 at the wall independent of the molecular Prandtl number. Both reach their maxima at around $y^+ \approx 45$. Similar values are also reported by previous studies, e.g. Kong et al. (2000) for turbulent boundary-layer flow and Antonia and Kim (1991) for fully developed turbulent channel flow. However, the profile pertaining to the scalar θ_1 with $Pr = 0.2$ is different from the others throughout the boundary layer. The value of Pr_t at the wall for θ_1 is about 0.9 and increases from the wall to the peak value of 1.2 at $y^+ \approx 45$. Bell and Ferziger (1993) obtained a similar peak value for $Pr = 0.1$, but their peak position occurs slightly closer to the wall. In addition, similar to the observation by Bell and Ferziger (1993), the peak values of Pr_t for all the Prandtl numbers are slightly lower than those reported by Kim and Moin (1989) in channel flow. However, Kawamura et al. (1998) found even lower peak values of $Pr = 0.71$ at $Re_\tau = 180$. In the wake region all the Pr_t start increasing again and reach a second peak near the boundary-layer edge. This second peak is due to the intermittency in the wake region of the boundary layer. Comparing with the data from Bell and Ferziger (1993), they only observed the second peak for $Pr = 0.1$, but not for the other Prandtl numbers. Outside the boundary layer, in all cases, Pr_t decreases again.

To analyse the near-wall asymptotic behaviour of the turbulent Prandtl number, one can expand the velocity and scalar distributions in Taylor series as discussed previously. Then the turbulent Prandtl number for the isoscalar wall is found to be constant near the wall while for the isoflux wall it has a linear behaviour with $Pr^{0.4}y^+$. These limiting behaviours are shown in Figure 10 (b).

3.4. *Budget equations*

From the DNS, the full budgets of the Reynolds-stress and scalar-flux equations are obtained. The transport equations for Reynolds stresses can be written as

$$\frac{\partial \langle u_i' u_j' \rangle}{\partial t} + C_{ij} = \mathcal{P}_{ij} + \Pi_{ij} + G_{ij} + T_{ij} + D_{ij} - \varepsilon_{ij} \ , \tag{19}$$

where the interpretations of the different terms can be found e.g. in Pope (2000).

Similarly, the transport equations for the scalar fluxes are given by

$$\frac{\partial \langle u_i' \theta' \rangle}{\partial t} + C_{\theta i} = \mathcal{P}_{\theta i} + \Pi_{\theta i} + G_{\theta i} + T_{\theta i} + \mathcal{D}_{\theta i} - \varepsilon_{\theta i} \ . \tag{20}$$

The different terms in the equation (20) are commonly expanded as

$$
\begin{aligned}
C_{\theta i} &\equiv \langle u_l \rangle \frac{\partial \langle u_i' \theta' \rangle}{\partial x_l} \ , \\
\mathcal{P}_{\theta i} &\equiv -\langle u_l' \theta' \rangle \frac{\partial \langle u_i \rangle}{\partial x_l} - \langle u_i' u_l' \rangle \frac{\partial \langle \theta \rangle}{\partial x_l} \ , \\
\Pi_{\theta i} &\equiv \langle p' \frac{\partial \theta'}{\partial x_i} \rangle \ , \\
G_{\theta i} &\equiv -\frac{\partial \langle p' \theta' \rangle}{\partial x_i} \ , \\
T_{\theta i} &\equiv -\frac{\partial \langle u_i' u_l' \theta' \rangle}{\partial x_l} \ , \\
\mathcal{D}_{\theta i} &\equiv \frac{\partial}{\partial x_l} \left(\frac{1}{Pe} \langle u_i' \frac{\partial \theta'}{\partial x_l} \rangle + \frac{1}{Re_{\delta_0^*}} \langle \theta' \frac{\partial u_i'}{\partial x_l} \rangle \right) \ , \\
\varepsilon_{\theta i} &\equiv (\frac{1}{Re_{\delta_0^*}} + \frac{1}{Pe}) \langle \frac{\partial u_i'}{\partial x_l} \frac{\partial \theta'}{\partial x_l} \rangle \ ,
\end{aligned}
$$

where $C_{\theta i}$ is denoted as the mean convection, $\mathcal{P}_{\theta i}$ is the production term due to both the mean gradients of velocity and scalar. $\Pi_{\theta i}$ is the pressure scalar-gradient correlation term representing the inter-component redistribution of the turbulent energy between scalar-flux terms. $G_{\theta i}$ is the divergence of the pressure-scalar correlation term which represents spatial redistribution of the energy among different scalar-flux components due to inhomogeneities in the flow field. $\Pi_{\theta i}+G_{\theta i}$ is the scalar pressure-gradient correlation term also denoted as the pressure scrambling term. $T_{\theta i}$ is the turbulent diffusion, which is the divergence of the triple correlation tensor, acting as a spatial redistribution term. $\mathcal{D}_{\theta i}$ is the molecular diffusion term and $\varepsilon_{\theta i}$ the dissipation term.

All the terms in the budget equations are explicitly evaluated including the pressure terms. Two scalings are used: First, a scaling in wall units (inner scaling), i.e. non-dimensionalised by $\frac{u_\tau^4}{\nu}$ for the Reynolds-stress budgets and $\frac{u_\tau^3 \theta_\tau}{\nu}$ for the scalar-flux budgets where θ_τ is the friction scalar and defined by $\frac{q_w}{\rho c_p u_\tau}$. Secondly, an outer scaling is used, i.e. quantities are non-dimensionalised by $\frac{U_\infty^3}{\delta^*}$ for the Reynolds-stress budgets and $\frac{U_\infty^2 (\theta_\infty - \theta_w)}{\delta_\theta^{99}}$ for the scalar-flux budgets where δ^* is the local displacement thickness and δ_θ^{99} the 99% local scalar boundary-layer thickness. The residual for all the budgets is at most $\mathcal{O}(10^{-3})$ in viscous scaling.

All the Reynolds-stress budgets compare very well with previous studies in both inner and outer scalings, e.g. see Spalart (1988) and Komminaho and Skote (2002). Therefore, these budgets are not discussed further in the interest of space.

In Figure 11, the budget for the streamwise scalar flux of θ_4 ($Pr = 2.0$) is shown. All the terms are normalised such that the sum of the square of all terms is unity. One can clearly see that the mean convection term, which is negligible

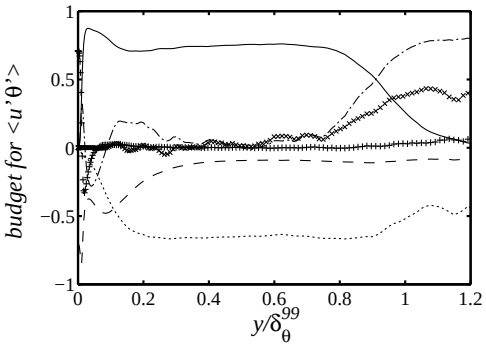

FIGURE 11. Budgets of normalised streamwise scalar flux in outer scaling at $Re_\theta = 830$ pertaining to θ_4 with $Pr = 2.0$. ——Production, – – –Dissipation, –·–Turbulent diffusion, ····· Scalar pressure-diffusion, + Molecular diffusion, × Mean convection.

near the wall, becomes a major balancing term near the boundary-layer edge, together with the pressure-diffusion and the turbulent diffusion terms. The latter is noticeable in the near-wall region and near the boundary-layer edge, similar as for the Reynolds stresses. For the case of θ_2 ($Pr = 0.71$), the budget for the wall-normal scalar flux $\langle v'\theta' \rangle$ at $Re_\theta = 830$ compares well with the data from Hattori et al. (2007) at a higher Reynolds number $Re_\theta = 1000$.

To further investigate the Pr effects, the budgets of the streamwise and wall-normal scalar fluxes are scaled such that all the dominant terms collapse for both inner and outer scalings. For the budgets in inner scaling as shown in Figure 12 (a) and (b), the streamwise budget $\langle u'\theta' \rangle$ normalised by $Pr^{\frac{1}{2}}$ and the wall-normal budget $\langle v'\theta' \rangle$ normalised by $Pr^{\frac{1}{4}}$ are found to scale with $Pr^{\frac{1}{4}} y^+$. The channel data from Kawamura et al. (1999) with $Pr = 0.71$ at $Re_\tau = 395$ is also included, and very good agreement can be seen for both the streamwise and wall-normal scalar fluxes. For the streamwise scalar fluxes of θ_3 and θ_5, due to the different boundary conditions the agreement with the channel data is only good except in the close vicinity of the wall. The production and dissipation terms are dominant and the molecular diffusion term is only noticeable in the near-wall region. The scalar pressure-gradient correlation term always lies on the loss side and becomes comparable with the dissipation term at $y^+ \approx 40$. Further away from the wall, the scalar pressure-gradient correlation term becomes larger than the dissipation term (see Figure 11). For the wall-normal scalar flux (see Figure 12 (b)), a larger but still insignificant difference is observed. The wall boundary condition seems to only influence the dissipation and turbulent diffusion terms and it is less effective in the wall-normal scalar fluxes compared to the streamwise scalar fluxes. The production term is negative for the wall-normal scalar flux. Due to the isotropy in the dissipation scale, the dissipation is negligible for fluids with $Pr \geq 0.7$

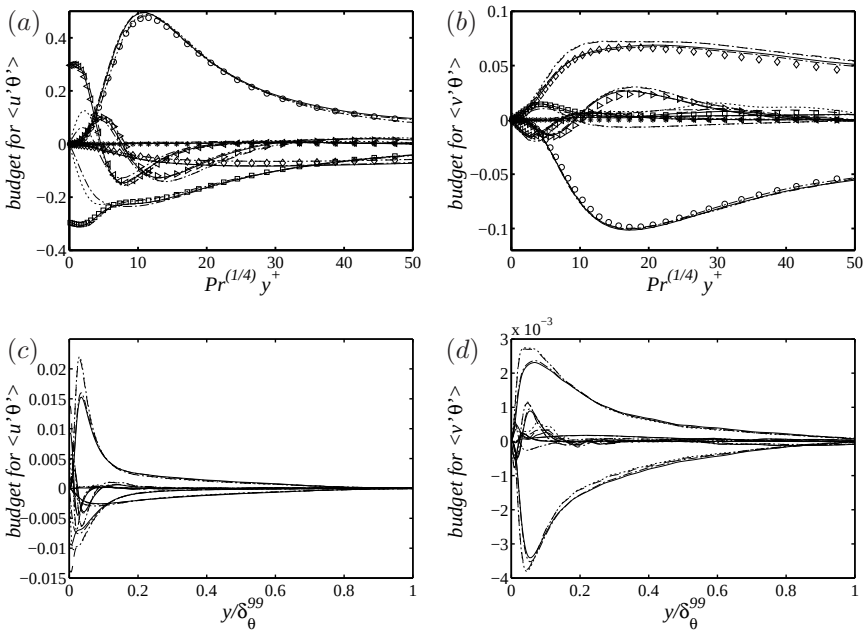

FIGURE 12. Prandtl-number dependent scaled budgets of the streamwise and wall-normal scalar fluxes at $Re_\theta = 830$. ——θ_2, –·–θ_3, – – –θ_4, ·····θ_5, ∘ Production, □ Dissipation, ◊ Scalar pressure-diffusion, ◁ Molecular diffusion, ▷ Turbulent diffusion, ∗ Mean convection. Symbols are from Kawamura et al. (1999) at $Re_\tau = 395$ with $Pr = 0.71$. (*a*) Budget for $\langle u'\theta' \rangle$ in inner scaling, (*b*) Budget for $\langle v'\theta' \rangle$ in inner scaling, (*c*) Budget for $\langle u'\theta' \rangle$ in outer scaling, (*d*) Budget for $\langle v'\theta' \rangle$ in outer scaling.

(Kawamura et al. 1998). This is also true for the present DNS except in the close vicinity of the wall. Thus, the production is balanced mainly by the scalar pressure-gradient correlation term. According to Kawamura et al. (1998), in a low Prandtl-number fluid, the dissipation is dominant because it takes place in eddies of a larger scale. They reported that the scalar pressure-gradient term is dominant for $Pr = 0.4$ and 5.0 while the dissipation term is overwhelming for $Pr = 0.05$. They also reported that the scalar pressure-gradient and the dissipation terms become comparable at $Pr = 0.2$ which is however not true for the present DNS (not shown here).

For the outer scaling as shown in Figure 12 (*c*) and (*d*), the budgets are normalised empirically by $Pr^{-\frac{1}{3}}$ to collapse all the curves. The budgets belonging to the scalar with $Pr = 0.2$ are excluded due to low Pr effects. The present scalings are based on the range of Pr of the simulation, therefore further investigations are needed to confirm the validity of the results. In addition,

except for the low Pr case, all the budgets of the scalar fluxes $\langle u'\theta' \rangle$ and $\langle v'\theta' \rangle$ look very much like those of the Reynolds stresses $\langle u'u' \rangle$ and $\langle u'v' \rangle$, respectively. Further discussions concerning low Pr effects can be found in Kasagi and Ohtsubo (1993).

3.5. *Higher-order statistics*

For a normally distributed random variable, the respective skewness and flatness factors are 0 and 3, respectively. In the near-wall region, the behaviours of the skewness and flatness factors for the velocity and pressure components are similar to those in the channel-flow simulation by Kim et al. (1987). The wall values of the skewness and flatness factors for the pressure fluctuation are -0.04 and 4.9 which are comparable to the results -0.1 and 5.0 obtained by Kim (1989).

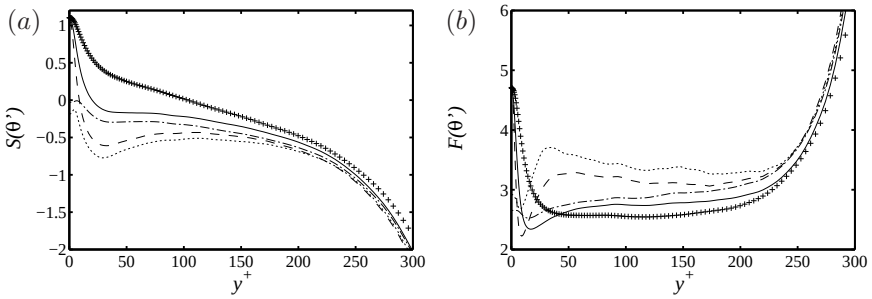

FIGURE 13. Skewness and flatness-factor distributions of the scalars at $Re_\theta = 830$. + θ_1, ——θ_2, –·–θ_3, – – –θ_4, ····· θ_5. (a) Skewness factor $S(\theta')$, (b) Flatness factor $F(\theta')$. The scalar boundary-layer thicknesses at $Re_\theta = 830$ are ranging from $y^+ \approx 320$ to 365.

The skewness and flatness factors for the scalars are shown in Figure 13. The profiles of θ_2 and θ_4 compare well with the data by Tohdoh et al. (2008). The skewness factors for the isoflux wall are closer to zero in the vicinity of the wall which implies more symmetric fluctuations than those of the isoscalar wall (Kong et al. 2000). Within the conductive sub-layer, $S(\theta')$ with isoscalar wall are positive which is consistent with the positive $S(u')$ (Antonia and Danh 1977). Redjem-Saad et al. (2007) reported that in a turbulent pipe simulation $F(\theta') = 7$ at the wall for $Pr = 0.71$ which is higher than the present DNS results, which might be due to the surface curvature in the pipe. In addition, $F(\theta')$ reaches its first minimum at about the wall-normal position where the corresponding RMS of the scalar fluctuations are maximum. A similar behaviour can be observed for the streamwise velocity (Durst et al. 1987). An interesting observation is that the effects of the different boundary conditions seem to influence not only the near-wall region; a clear difference can be observed up to $y^+ \approx 150$. On the other hand, the wall values of the higher-order

terms for isoscalar boundary condition, i.e. about 1.0 for the skewness and 4.5 for the flatness, appear to be Prandtl-number independent. In the outer region, the skewness and flatness factors increase rapidly which indicates the intermittent region similarly as for the velocity and pressure components. The maximum peak values of $S(\theta')$ and $F(\theta')$ are however much higher than $S(u')$ and $F(u')$ which is also observed in experiments by Antonia and Danh (1977).

3.6. *Probability density functions*

A different perspective on the characteristics of the fluctuations of one or more variables is provided by analysing the probability density functions (PDF). The PDF distributions of the velocity and pressure fluctuations at various wall-normal positions, ranging from $y^+ \approx 5$ in the viscous sub-layer to $y^+ \approx 500$ in the free-stream (the boundary-layer thickness is about $y^+ = 315$ at $Re_\theta = 830$), are obtained from the simulation as well as the corresponding distributions of the different scalar fluctuations.

The general shape of $P(u')$ agrees well with the experiment study by Durst et al. (1987). For the PDF of the wall-normal velocity fluctuation, Nagano and Tagawa (1988) reported that the distributions are close to the Gaussian distribution in the near-wall region and depart from the Gaussian distribution far away from the wall. However, the present DNS shows more pointy distributions very close to the wall due to the large $F(v')$ values, a behaviour which has been reported virtually for all simulations of wall-bounded turbulence. The PDF of the pressure fluctuation (not shown here) is negatively skewed throughout the boundary layer until the free-stream and the wall-pressure distribution compares well with the data from Kim (1989).

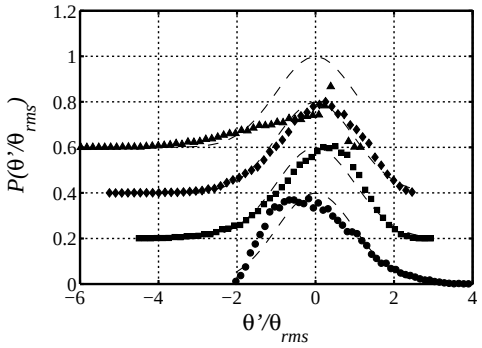

FIGURE 14. PDF of θ_4' with $Pr = 2.0$ and isoscalar wall at $Re_\theta = 830$ with boundary-layer edge at $y^+ = 320$. • $y^+ \approx 5$, ■ $y^+ \approx 50$, ♦ $y^+ \approx 100$, ▲ $y^+ \approx 300$, – – –Gaussian distribution.

The PDF of the scalar fluctuations of the isoscalar boundary condition are similar to the distributions of the streamwise velocity which reflects the overall

similarity between the streamwise velocity u and scalar θ (Antonia et al. 1988). The PDF distribution of θ_4 ($Pr = 2.0$) is shown in Figure 14 at different wall-normal positions. A Gaussian distribution with zero mean and matching variance is also included as a reference. All the fluctuations are normalised by the corresponding RMS values and the probability density functions are normalised to unit area. The PDF for the other scalars with isoscalar boundary condition have a similar shape. In particular, a long positive tail at $y^+ \approx 5$ also exists as for streamwise velocity u. This tail is caused by the sweep-type motion of the low momentum fluids and low concentration of scalars (Nagano and Tagawa 1988). The positive tail shortens with increasing Pr and also with increasing wall-normal distance as shown in Figure 14. As the Pr or the wall-normal distance is increased, the negative tail extends longer. For the scalars with isoflux boundary condition (not shown here), the PDF distributions are closer to the Gaussian distribution in the near-wall region. Far away from the wall ($y^+ > 50$), there is no noticeable difference between the distributions with the different boundary conditions. At $y^+ \approx 300$, all the PDF of the scalar fluctuations are extremely negatively skewed which indicates the existence of the intermittent region. In the free-stream, as expected, the profiles are again close to the Gaussian distribution with extremely small variance.

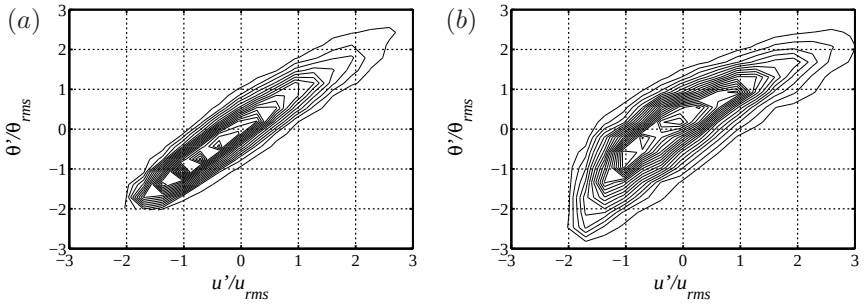

FIGURE 15. JPDF of (u', θ') ($Pr = 2.0$) at $y^+ \approx 5$ with $Re_\theta = 830$. (a) $P(u', \theta'_4)$, (b) $P(u', \theta'_5)$. Contour levels are 0.025:0.025:0.5 for (a) and 0.016:0.016:0.32 for (b).

The high correlation between streamwise velocity and the scalar is also illustrated by the joint probability density function (JPDF). The results of θ'_2 at $y^+ \approx 5$ are consistent with the previous results from a channel DNS simulation by Kim and Moin (1989). JPDF of (u', θ') of $Pr = 2.0$ at $y^+ \approx 5$ and $Re_\theta = 830$ are shown in Figure 15. A less correlated relation between the streamwise velocity and the scalars with isoflux boundary condition is observed, indicating the influence of the different boundary conditions for u and θ for these cases.

The JPDF of (u', θ'_2) and $(u', -v')$ at $y^+ \approx 200$ with $Re_\theta = 830$ are shown in Figure 16. Far away from the wall, all the JPDF distributions show mildly

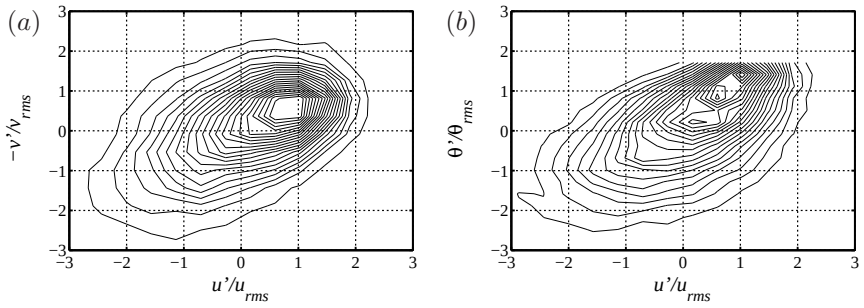

FIGURE 16. JPDF of $(u', -v')$ and (u', θ_2') at $y^+ \approx 200$ with $Re_\theta = 830$. (a) $P(u', -v')$, (b) $P(u', \theta_2')$. Contour levels are 0.012:0.012:0.24 for (a) and from 0.01:0.01:0.2 for (b).

correlated shapes as expected. The scalar boundary condition has almost no effect at this wall-normal position. It is noticeable that not all the contours have their centres located at the origin and the peaks of (u', θ') moves from the third quadrant to the first quadrant as the wall-normal position increases.

Note that in JPDF Figures 15 (a) and 16 (b), one can observe a sharp cut-off for the scalar fluctuation θ'. This is caused by the Dirichlet boundary condition, which bounds the scalar values to be between θ_w and θ_∞. In consequence, the scalar fluctuations have strict lower and upper bounds, depending on the local mean values.

3.7. *Spanwise two-point correlation*

The spanwise two-point correlations of the velocity components and pressure at $Re_\theta = 830$ at several wall-normal positions from $y^+ \approx 5$ to $y^+ \approx 300$ are obtained. In general the results are consistent with the numerical results by Kim et al. (1987). As also observed by Kim (1989), the spanwise two-point correlation coefficient of the pressure does not have the negative excursion.

The spanwise two-point correlations of the scalars near the wall are similar to those observed by Kim and Moin (1989). On the other hand, the scalars of the isoflux boundary condition seem to be much more affected by the Prandtl number. In general, scalars with isoflux wall have larger mean spanwise spacings than those of the isoscalar wall (Kong et al. 2000). Far from the wall, the boundary conditions do not have an influence on the profiles.

For the mean low-speed streak and scalar streak spacings obtained from twice the first minimum of the spanwise two-point correlations, the results for θ_2 and θ_3 compare well with Kong et al. (2000). As also noted by Kong et al. (2000) that the low-speed streak spacing is similar to that of θ_2 and the differences from the boundary conditions are only observable in the near-wall region. One can also observe that the mean scalar streak spacings are larger for smaller

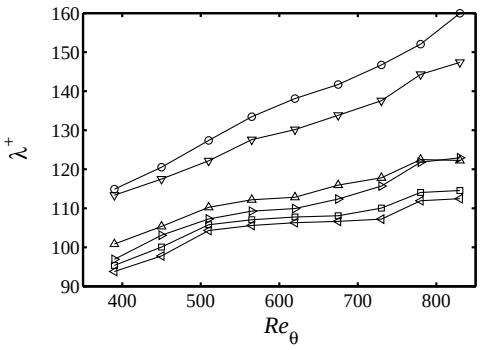

FIGURE 17. Streamwise variation of the mean spanwise streaks spacing λ^+ at $y^+ \approx 7$. $\square$ u, $\circ$ θ_1, $\triangle$ θ_2, ∇ θ_3, $\triangleleft$ θ_4, $\triangleright$ θ_5.

Pr near the wall. Due to the isoflux wall boundary condition, the scalar spacings first decrease and then increase again as being away from the wall (not shown here). The streamwise evolution of the mean streak spacings at $y^+ \approx 7$ from $Re_\theta = 390$ to $Re_\theta = 830$ is shown in Figure 17. In general all the steak spacings grow slightly downstream with increasing Reynolds numbers, however, the growth rate levels off towards larger Reynolds numbers. The large growth rate in the low Reynolds number range may be due to a low Reynolds-number effect (Antonia and Kim 1994). At $Re_\theta = 830$, the streaks have a spacing of about 110 in wall unit which is slightly larger than the usual value of about 100 (Kim et al. 1987). On the other hand, this spacing is in good agreement with recent studies in turbulent boundary layer by Schlatter et al. (2009). These authors also found that the velocity streak spacing continues to grow up to $Re_\theta = 1500$ and then settles at a constant value around 115. The streaks pertaining to scalars with isoflux boundary condition are growing faster than those with isoscalar boundary condition at the same Pr. It is also suggested by the present results that the streak spacing with lower Pr grows faster. It has also been shown by Österlund (1999) and Abe et al. (2001) that the spanwise two-point correlations of the wall-shear stress τ_w and streamwise velocity fluctuation u' have less prominent negative peaks with increasing Reynolds number, which is confirmed by the present DNS. This effect is due to the dominating large-scale structures which scale with outer units, i.e. the boundary-layer thickness or the channel half width, see also Schlatter et al. (2009). Schlatter et al. (2009) also showed that at least $Re_\theta = 1500$ is needed to clearly observe a second peak indicating the footprint of the large-scale structure in a contour plot of the two-point correlation of the wall-shear stress τ_w versus the Reynolds number. Concerning the scalar two-point correlations, Abe et al. (2004) showed that less prominent negative peaks with increasing Reynolds number only exist for the surface heat flux q_w with $Pr = 0.71$, but not for the case with $Pr = 0.025$ due to a low Prandtl-number effect. However, for the Pr-range considered here, all

scalars irrespective of the boundary condition feature a decreasing near-wall (inner) peak.

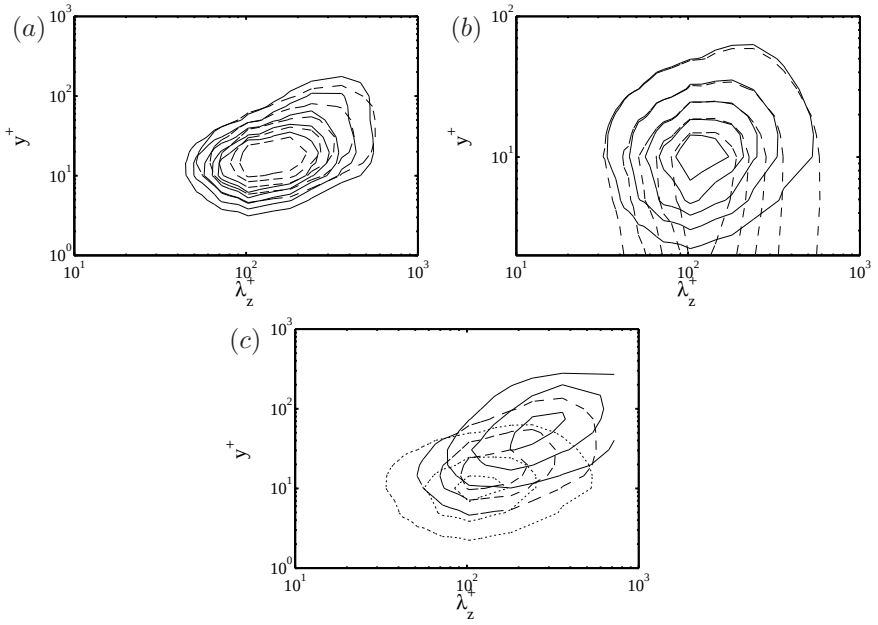

FIGURE 18. Premultiplied energy spectra of the streamwise velocity and scalars at $Re_\theta = 830$. (a) ——$k_z\Phi_{uu}(\lambda_z)/u_\tau^2$, - - -$k_z\Phi_{\theta_2\theta_2}(\lambda_z)/\theta_\tau^2$, (b) $k_z\Phi_{\theta\theta}(\lambda_z)/\theta_\tau^2$ at $Pr = 2.0$, ——isoscalar boundary condition, - - -isoflux boundary condition, (c) $k_z\Phi_{\theta\theta}(\lambda_z)/\theta_\tau^2$ with isoscalar boundary condition, ——$Pr = 0.2$, - - -$Pr = 0.71$, ····· $Pr = 2.0$. Contour levels are 1:0.375:2.5 in (a); 2:1.5:8 in (b); and 0.3:0.3:0.9 for $Pr = 0.2$, 1:0.75:2.5 for $Pr = 0.71$ and 2:3:8 for $Pr = 2.0$ in (c).

The spanwise two-point correlations not only contain the information about the spanwise organisation of the near-wall streaks but also the large-scale motions in the outer region of the boundary layer. By showing the premultiplied spanwise spectra $k_z\Phi_{uu}(\lambda_z)$ of the streamwise velocity u, both experiment (e.g. Hutchins & Marusic (2007)) and simulation (e.g. del Álamo and Jiménez (2003)) showed evidence of the large-scale structures existing in the outer layer. For the scalar field, Abe and Kawamura (2002) reported the existence of the large-scale structure in the outer layer of the channel for $Re_\tau = 640$ with $Pr = 0.025$ and 0.71, but no detailed discussion was provided. Figure 18 (a) shows the one-dimensional spanwise spectra $k_z\Phi_{uu}(\lambda_z)$ and $k_z\Phi_{\theta_2\theta_2}(\lambda_z)$ scaled with u_τ^2 and θ_τ^2, respectively, at $Re_\theta = 830$. In general, both spectra are similar in appearance with the inner peak located at $y^+ \approx 15$ (see also Figure 8 (b))

and $\lambda_z \approx 110$ indicating the near-wall streaks. However, differences can be observed in the outer region ($y^+ > 100$) where the outer peak of θ_2 is weaker than that of u. Figure 18 (b) shows the spanwise spectra for scalars θ_4 and θ_5 with different boundary conditions but same $Pr = 2.0$. The influence of the different boundary conditions is clearly seen. The spectrum of θ_5 with isoflux boundary condition has a constant value down to the wall whereas the spectrum of θ_4 is decreasing to zero to fulfil the boundary condition. Above $y^+ = 10$, there is no clear difference. Compared to Figure 18 (a), it is important to note that the outer peak ($\lambda_z^+ \approx 400$) does not exist for $Pr = 2.0$. Figure 18 (c) shows Pr effects on the spanwise spectra. With increasing Pr, the spectral peaks move towards the wall and towards smaller spanwise wavelengths λ_z (see also Figure 17). Note that the inner peak for the case of $Pr = 0.2$ resides at $y^+ \approx 50$ which is also observed in the RMS value of the scalar variance as shown in Figure 8 (b). If the spanwise spectrum of θ_1 ($Pr = 0.2$) is scaled by θ_{rms}^2 instead of θ_τ^2, the peak extends towards $y^+ \approx 10$, however the corresponding fluctuations θ_{rms} close to the wall are extremely small.

4. Conclusions

A direct numerical simulation (DNS) of a spatially developing turbulent boundary layer with passive scalars over a flat plate under zero pressure gradient (ZPG) has been carried out. The Reynolds number based on the inlet displacement thickness $Re_{\delta_0^*}$ is 450, and Prandtl numbers are varying from 0.2 to 2 while two wall boundary conditions, i.e. isoscalar and isoflux, are employed. The highest Reynolds number obtained is $Re_\theta = 850$ based on the momentum thickness θ. The computed velocity and scalar fields are compared with existing data from the literature and the agreement is very good in general.

The main conclusions of the present study are summarised as follows:

• The mean scalar profiles are virtually independent of the employed wall boundary conditions whereas the effects on the scalar variances are obvious in the near-wall region. Further away from the wall, the effects from different wall boundary conditions are negligible. The skewness and flatness profiles are different up to about 150 in viscous units, i.e. to the middle of the boundary layer for the present simulation parameters.

• The results (mean scalar profiles, Pr_t, JPDF, two-point correlations etc.) for θ_2 with $Pr = 0.71$ and isoscalar boundary condition obtained from the present DNS and those from Kim and Moin (1989) using an internal heat source appear similar in the near-wall region. This implies that these two boundary conditions might not have a significant influence on the low-order statistics in the near-wall region.

• All the terms in the Reynolds-stress and scalar-flux budgets are explicitly evaluated including the pressure terms. Far away from the wall, both the mean convection and the turbulent diffusion term become balancing terms in the scalar-flux budgets, together with the pressure-diffusion term. This is in good agreement to the Reynolds-stress budgets.

• Prandtl-number scalings for the scalar-flux budgets and several other scalar quantities in both inner and outer units are proposed based on the present data, however, further investigations at wider Pr range are needed to validate the results.

• The intermittency in the outer region is identified and quantified via higher-order statistics and PDF distributions.

• The scalar with isoscalar boundary condition is highly correlated with the streamwise velocity component in the near-wall region, however showing the influence of the wall boundary condition. Near the boundary-layer edge, a mild correlation between these two quantities was observed, especially independent of the boundary condition.

• All the scalar streak spacings grow downstream with increasing Reynolds numbers. The scalar streak spacings pertaining to the isoflux boundary condition and lower Pr grow faster.

• The large-scale structures could be identified with the help of the premultiplied spanwise energy spectra. There certainly exist large-scale structures for the velocity field and scalar with $Pr = 0.71$. For the higher Pr cases, no large-scale structures are identified. The inner spectra peaks move away from the wall and towards larger wavelengths λ_z as Pr decreases.

• Even though the Reynolds number considered in the present study is so far the highest with such a variety of scalars, it is still low compared to the experiments. Therefore, low Reynolds-number effects are important and play a role when interpreting the results.

In the future, the large amount of data from the simulation will be further processed and new and existing LES/RANS closures for modelling the scalar-fluxes will be developed and critically evaluated against the present database.

The present database will be open to public access through the following link: http://www.mech.kth.se/.

Acknowledgements

Computer time was provided by the Center for Parallel Computers (PDC) at the Royal Institute of Technology (KTH) and the National Supercomputer Center (NSC) at Linköping University in Sweden.

References

Abe, H., Kawamura, H., 2002. A study of turbulence thermal structure in a channel flow through DNS up to $Re_\tau = 640$ with $Pr = 0.025$ and 0.71. In: Castro, I. P., Hancock, P. E., Thomas, T. G. (Eds.), Advances in Turbulence IX. CIMNE, Barcelona, Spain, pp. 399–402.

Abe, H., Kawamura, H., Matsuo, Y., 2001. Direct numerical simulation of a fully developed turbulent channel flow with respect to the Reynolds number dependence. J. Fluids Engng. 123 (2), 382–393.

Abe, H., Kawamura, H., Matsuo, Y., 2004. Surface heat-flux fluctuations in a turbulent channel flow up to $Re_\tau = 1020$ with $Pr = 0.025$ and 0.71. Int. J. Heat Fluid Flow 25 (3), 404–419.

Antonia, R. A., Danh, H. Q., 1977. Structure of temperature fluctuations in a turbulent boundary layer. Phys. Fluids 20 (7), 1050–1057.

Antonia, R. A., Kim, J., 1991. Turbulent Prandtl number in the near-wall region of a turbulent channel flow. Int. J. Heat Mass Transfer 34 (7), 1905–1908.

Antonia, R. A., Kim, J., 1994. Low-Reynolds-number effects on near-wall turbulence. J. Fluid Mech. 276, 61–80.

Antonia, R. A., Krishnamoorthy, L. V., Fulachier, L., 1988. Correlation between the longitudinal velocity fluctuation and temperature fluctuation in the near-wall region of a turbulent boundary layer. Int. J. Heat Mass Transfer 31 (4), 723–730.

Bell, D. M., Ferziger, J. H., 1993. Turbulent boundary layer dns with passive scalars. In: So, R. M. C., Speziale, C. G., Launder, B. E. (Eds.), Near-Wall Turbulent Flows. Elsevier, pp. 327–366.

Bertolotti, F. P., Herbert, T., Spalart, P. R., 1992. Linear and nonlinear stability of the Blasius boundary layer. J. Fluid Mech. 242, 441–474.

Brandt, L., Schlatter, P., Henningson, D. S., 2004. Transition in boundary layers subject to free-stream turbulence. J. Fluid Mech. 517, 167–198.

Chevalier, M., Schlatter, P., Lundbladh, A., Henningson, D. S., 2007. A pseudo-spectral solver for incompressible boundary layer flows. Tech. Rep. TRITA-MEK 2007:07, Royal Institute of Technology, Stockholm.

Corrsin, S., 1952. Heat transfer in isotropic turbulence. J. Appl. Phys. 23 (1), 113–118.

del Álamo, J. C., Jiménez, J., 2003. Spectra of the very large anisotropic scales in turbulent channels. Phys. Fluids 15 (6), L41–L44.

Durst, F., Jovanovic, J., Kanevce, L., 1987. Probability density distribution in turbulent wall boundary-layer flows. In: Durst, F., Launder, B. E., Lumley, J. L., Schmidt, F. W., Whitelaw, J. H. (Eds.), Turbulent Shear Flows 5. Springer-Verlag, Berlin, pp. 197–220.

Hattori, H., Houra, T., Nagano, Y., 2007. Direct numerical simulation of stable and unstable turbulent thermal boundary layers. Int. J. Heat Fluid Flow 28 (6), 1262 – 1271.

Hetsroni, G., Kowalewski, T. A., Hu, B., Mosyak, A., 2001. Tracking of coherent thermal structures on a heated wall by means of infrared thermography. Exps. Fluids 30 (3), 286–294.

Hishida, M., Nagano, Y., 1979. Structure of turbulent velocity and temperature fluctuations in fully developed pipe flow. ASME J. Heat Transfer 101, 15–22.

Hutchins, N., Marusic, I., 2007. Evidence of very long meandering features in the logarithmic region of turbulent boundary layers. J. Fluid Mech. 579, 1–28.

Kader, B. A., 1981. Temperature and concentration profiles in fully turbulent boundary layers. Int. J. Heat Mass Transfer 24 (9), 1541–1544.

Kasagi, N., Ohtsubo, Y., 1993. Direct numerical simulation of low Prandtl number thermal fluid in a turbulent channel flow. In: Durst, F. (Ed.), Turbulent Shear Flows 8. Springer-Verlag, Berlin, pp. 97–119.

Kasagi, N., Tomita, Y., Kuroda, A., 1992. Direct numerical simulation of passive scalar field in a turbulent channel flow. ASME J. Heat Transfer 114, 598–606.

Kawamura, H., Abe, H., Matsuo, Y., 1999. DNS of turbulent heat transfer in channel flow with respect to reynolds and prandtl number effects. Int. J. Heat Fluid Flow 20 (3), 196–207.

Kawamura, H., Ohsaka, K., Abe, H., Yamamoto, K., 1998. DNS of turbulent heat transfer in channel flow with low to medium-high prandtl number fluid. Int. J. Heat Fluid Flow 19 (5), 482–491.

Kays, W. M., Crawford, M. E., 1993. Convective Heat and Mass Transfer, 3rd Edition. McGraw-Hill, New York, U.S.A.

Kim, J., 1989. On the structure of pressure fluctuations in simulated turbulent channel flow. J. Fluid Mech. 205, 421–451.

Kim, J., Moin, P., 1989. Transport of passive scalars in a turbulent channel flow. In: André, J.-C., Cousteix, J., Durst, F., Launder, B. E., Schmidt, F. W. (Eds.), Turbulent Shear Flows 6. Springer-Verlag, Berlin, pp. 85–96.

Kim, J., Moin, P., Moser, R., 1987. Turbulence statistics in fully developed channel flow at low Reynolds number. J. Fluid Mech. 177, 133–166.

Komminaho, J., Skote, M., 2002. Reynolds stress budgets in Couette and boundary layer flows. Flow, Turbulence Combust. 68 (2), 167–192.

Kong, H., Choi, H., Lee, J. S., 2000. Direct numerical simulation of turbulent thermal boundary layers. Phys. Fluids 12 (10), 2555–2568.

Krishnamoorthy, L. V., Antonia, R. A., 1987. Temperature-dissipation measurements in a turbulent boundary layer. J. Fluid Mech. 176, 265–281.

Li, Q., Schlatter, P., Brandt, L., Henningson, D. S., 2008. Direct numerical simulation of a turbulent boundary layer with passive scalar transport. In: Direct and Large-Eddy Simulation VII. Springer-Verlag, Berlin.

Mosyak, A., Pogrebnyak, E., Hetsroni, G., 2001. Effect of constant heat flux boundary condition on wall temperature fluctuations. ASME J. Heat Transfer 123 (2), 213–218.

Nagano, Y., Tagawa, M., 1988. Statistical characteristics of wall turbulence with a passive scalar. J. Fluid Mech. 196, 157–185.

Nagib, H. M., Chauhan, K. A., Monkewitz, P. A., 2007. Approach to an asymptotic state for zero pressure gradient turbulent boundary layers. Phil. Trans. R. Soc. A 365, 755–770.

Nordström, J., Nordin, N., Henningson, D. S., 1999. The fringe region technique and the Fourier method used in the Direct Numerical Simulation of spatially evolving viscous flows. SIAM J. Sci. Comp. 20 (4), 1365–1393.

Österlund, J. M., 1999. Experimental studies of zero pressure-gradient turbulent boundary layer flow. Ph.D. thesis, Royal Institute of Technology, Stockholm, Sweden.

Österlund, J. M., Johansson, A. V., Nagib, H. M., Hites, M. H., 1999. Wall shear stress measurements in high Reynolds number boundary layers from two facilities. AIAA J. 1999-3814.

Perry, A. E., Hoffmann, P. H., 1976. An experimental study of turbulent convective heat transfer from a flat plate. J. Fluid Mech. 77, 355–368.

Pope, S. B., 2000. Turbulent Flows. Cambridge University Press, Cambridge, U.K.

Purtell, L. P., Klebanoff, P. S., Buckley, F. T., 1981. Turbulent boundary layer at low Reynolds number. Phys. Fluids 24 (5), 802–811.

Redjem-Saad, L., Ould-Rouiss, M., Lauriat, G., 2007. Direct numerical simulation of turbulent heat transfer in pipe flows: Effect of Prandtl number. Int. J. Heat Fluid Flow 28 (5), 847–861.

Roach, P. E., Brierley, D. H., 1992. The influence of a turbulent freestream on zero pressure gradient transitional boundary layer development, part I: Test cases T3A and T3B. In: Numerical Simulation of Unsteady Flows and Transition to Turbulence, ERCOFTAC. Cambridge University Press, Cambridge, U.K., pp. 319–347.

Rogers, M., Moin, P., Reynolds, W., 1986. The structure and modeling of the hydrodynamic and passive scalar fields in homogeneous turbulent shear flow. Tech. Rep. TF-25, Stanford University, U.S.A.

Schlatter, P., Örlü, R., Li, Q., Brethouwer, G., Fransson, J. H. M., Johansson, A. V., Alfredsson, P. H., Henningson, D. S., 2009. Turbulent boundary layers up to $Re_\theta = 2500$ studied through numerical simulation and experiments. Phys. Fluids, Accepted.

Spalart, P. R., 1988. Direct simulation of a turbulent boundary layer up to $Re_\theta = 1410$. J. Fluid Mech. 187, 61–98.

Subramanian, C. S., Antonia, R. A., 1981. Effect of Reynolds number on a slightly heated turbulent boundary layer. Int. J. Heat Mass Transfer 24 (11), 1833–1846.

Tiselj, I., Bergant, R., Mavko, B., Bajsić, I., Hetsroni, G., 2001. DNS of turbulent heat transfer in channel flow with heat conduction in the solid wall. ASME J. Heat Transfer 123, 849–857.

Tohdoh, K., Iwamoto, K., Kawamura, H., 2008. Direct numerical simulation of passive scalar transport in a turbulent boundary layer. In: Proceedings of the 7^{th} International *ERCOFTAC* Symposium on Engineering Turbulence Modelling and Measurements, Limassol, Cyprus, 2008. pp. 169–174.

Warhaft, Z., Lumley, J. L., 1978. An experimental study of the decay of temperature fluctuations in grid-generated turbulence. J. Fluid Mech. 88, 659–685.

Wikström, P., 1998. Measurements, direct numerical simulation and modeling of passive scalar transport in turbulent flows. Ph.D. thesis, Royal Institute of Technology, Stockholm, Sweden.

Paper 5

5

Simulations of heat transfer in a boundary layer subject to free-stream turbulence

By Qiang Li, Philipp Schlatter, & Dan S. Henningson

Linné Flow Centre, KTH Mechanics
SE-100 44 Stockholm, Sweden

Published in TSFP-6, Seoul, South Korea, 2009

The present study investigates the effects of the ambient free-stream turbulence (FST) on the momentum and heat transfer in a turbulent flat-plate boundary layer via large-eddy simulations (LES) using the ADM-RT model. Due to a FST of 20%, the skin-friction coefficient c_f and Stanton number St are substantially elevated up to 15% in the fully turbulent region. The depression of both the mean velocity and temperature profiles in the wake region due to the FST is observed, however, the influence on the wall-normal heat flux in the near-wall region is negligible.

1. Introduction

The aim of this study is to perform numerical simulations to investigate the influence of free-stream turbulence (FST) on the momentum and heat transfer in a spatially evolving, fully turbulent boundary layer. Due to the ambient turbulence, such a boundary layer will undergo rapid bypass transition see *e.g.* Brandt *et al.* (2004) before reaching a turbulent state. This problem is of interest in many industrial applications in particular related to turbomachinery. Bradshaw (1974) performed the landmark work in this field and later a series of studies have been carried out, *e.g.* by Simonich & Bradshaw (1978), Hancock & Bradshaw (1983, 1989). These authors analysed the influence of the grid-generated FST in terms of both turbulence level and turbulent length scale. Up to 30% increase in the Stanton number due to 6% FST is reported. Blair (1983*a*,*b*) also reported that the momentum and heat transfer is augmented by grid-generated FST and that the heat transfer seems to be much more affected in a turbulent boundary layer. However, only as much as 20% increase for the heat transfer of a boundary layer under 7% FST was reported. Using the wake of a free jet as the inflow FST, Maciejewski & Moffat (1992*a*,*b*) reported a 1.8 $\sim$ 4 fold absolute augmentation in Stanton number due to free-stream turbulent fluctuations from 20% $\sim$ 60%. The extraordinarily high increase in the Stanton number might, however, be due to the incoming large-scale, anisotropic FST. In spite of the number of studies during the last decades, the problem at hand is still not fully understood. The conclusions from all the studies are general,

but the magnitude of the heat transfer enhancement varies considerably from one study to another (Maciejewski & Moffat 1992*a*,*b*).

Therefore, one could resort to numerical simulation. As the modern computers developed during the last 20 years, numerical simulation, in particular direct numerical simulations (DNS) and large-eddy simulations (LES), have become important tools for transition and turbulence research. Péneau *et al.* (2000, 2004) investigated the influence of high levels of FST on a spatially evolving turbulent boundary layer using LES with a dynamic mixed subgrid-scale (SGS) model. Some of the previous experimental observations were reproduced by their simulations. They further reported that the mean temperature profiles exhibit different slopes in the logarithmic region with increasing FST intensity whereas the velocity profiles remain essentially unchanged. Jacobs & Durbin (2000) have performed DNS of bypass transition at lower turbulence intensities including heat transfer ($Pr = 0.71$) and found a generally high correlation between the temperature and (streamwise) velocity during transition. In the turbulent regime, a minor reduction of the temperature profile in both the wake and logarithmic region could be observed.

The aim of the present study is to numerically examine the influence of ambient FST on the momentum and heat transfer at the wall in a fully turbulent boundary layer. Open questions related to quantifying the increase of the friction coefficient and the Stanton number due to high levels of FST shall be addressed. Coupled to these issues is the validity of the Reynolds analogy commonly applied for modelling purposes. As also suggested by Blair (1983*a*,*b*), effects of the FST on turbulent heat transfer within the boundary layer are discussed.

2. Numerical methodology

2.1. *Numerical method and SGS modelling*

The filtered three-dimensional, time-dependent, incompressible Navier–Stokes equations are solved using a pseudo-spectral method (Chevalier *et al.* 2007), *i.e.* Fourier series are employed in the wall-parallel directions and the wall-normal direction is discretised with Chebyshev polynomials. One more equation governing the heat transfer is solved with the same discretisation with the Prandtl number being 0.71. Since there is no feedback force, the temperature field is considered as a passive scalar. No-slip and isothermal wall boundary conditions are employed for velocity and temperature, respectively. The subgrid scale stress model used is the ADM-RT model (Schlatter *et al.* 2004) extended to also include passive scalars. Time is advanced with a mixed Runge–Kutta/Crank–Nicolson scheme. At the downstream end of the domain, a "fringe region" is added to fulfil the periodic boundary condition in the streamwise direction. In this region, the outflow is forced by a volume force to the laminar inflow condition, *i.e.* the Blasius boundary-layer profile. In addition, to trigger rapid laminar-turbulent transition, a random volume forcing located at a short distance downstream of the inlet ($x = 10, Re_x = 33400$) is used.

2.2. *Free-stream turbulence generation*

The boundary layer is subject to external disturbances, *i.e.* free-stream turbulence which is generated by a superposition of eigenmodes of the Orr-Sommerfeld/Squire operator from the continuous spectrum (Brandt *et al.* 2004). A similar way is also used by Jacobs & Durbin (2000). The generated FST is designed to be homogeneous and isotropic, following the von Kármán spectrum,

$$E(\kappa) \propto \frac{\kappa^4}{(C+\kappa^2)^{17/6}} \tag{1}$$

with C being a constant and κ denoting the spatial wavenumber. For small wavenumbers κ, *i.e.* large scales, such a spectrum is asymptotically proportional to κ^4, whereas the Kolmogorov $-\frac{5}{3}$ spectrum is recovered for large κ. Following Tennekes & Lumley (1972), an integral length scale L characterising the FST is defined as

$$L = \frac{1.8}{\kappa_{max}} \ , \tag{2}$$

where κ_{max} is the wavenumber of the maximum energy.

Note that each individual eigenmode of the Orr-Sommerfeld/Squire operator satisfies the continuity constraint, so the disturbances obtained by summing up different modes satisfy continuity as well. These disturbances are then introduced in the fringe region and subsequently advected downstream. Due to the high level of FST at the top boundary, the time step is limited and numerical instabilities might appear. Therefore, all the eigenfunctions are multiplied by a smooth step function above certain hight y_{damp} (non-dimensionalised by the displacement thickness at the inlet δ_0^*). In the present simulations, y_{damp} is chosen to be $y_l - 20$ where y_l is the total height of the computational domain.

Besides the free-stream turbulence in the velocity field, ambient disturbances in the temperature field are generated in a similar fashion as generating the "velocity" turbulence, but based on the continuous spectrum of the linearised temperature equation. The intensities of both the velocity and temperature disturbances can be controlled independently, therefore their influences on transitional and turbulent heat transfer can be examined individually.

The comparisons from different cases are made at the same Reynolds number based on certain measures of the boundary-layer thickness, *e.g.* $Re_\theta = \frac{U_\infty \theta}{\nu}$ or $Re_\tau = \frac{u_\tau \delta_{95}}{\nu}$ where U_∞ is the free-stream velocity, u_τ the friction velocity, θ the momentum thickness and δ_{95} the 95% boundary-layer thickness. By using these Reynolds numbers, the effect of the transition location on the data is removed. Due to the high FST levels, the momentum thickness θ is not appropriate, therefore, another definition θ_{95} defined by only integrating up to the 95% boundary-layer thickness is used in some cases. For the present numerical setup, possible history effects of the FST cannot be considered, *i.e.* the FST effects only depend on the local turbulence intensity and the length scale. To investigate the historical effects of the FST, one has to include the leading edge of the plate.

TABLE 1. Spatial resolution and box dimensions (including fringe region) for the present simulations.

	$x_l \times y_l \times z_l$ δ_0^*	$N_x \times N_y \times N_z$ (resolution)	$Re_{\delta_0^*}$
Box 1	$1000 \times 60 \times 50$	$256 \times 121 \times 36$	300
Box 2	$1500 \times 90 \times 90$	$384 \times 121 \times 96$	300
Box 3	$1500 \times 180 \times 180$	$384 \times 201 \times 128$	300
Box 4	$750 \times 40 \times 34$	$1024 \times 289 \times 128$	450

TABLE 2. Parameters used to define the FST and the corresponding computational domain for the simulations. Note that in Case 1, laminar-turbulent transition is only due to the FST whereas in the other cases an additional random forcing close to the inflow, *i.e.* the trip forcing, is active such that a large part of the computational box is turbulent. Case 5 corresponds to the DNS simulation by Li *et al.* (2008).

	Tu %	T_θ %	L δ_0^*	Box
Case 1	4.7	0, 4, 10, 40, 80	5	Box 1
Case 2	0	0	0	Box 2
Case 3	4.7, 20	0	2.5, 5, 7.5	Box 2
Case 4	4.7, 20	0	5, 7.5, 15	Box 3
Case 5	0	0	0	Box 4

2.3. *Simulation parameters*

The main parameters defining the problem are the Reynolds number, the intensities of both the velocity free-stream turbulence Tu and the thermal free-stream turbulence T_θ and the corresponding turbulence length scale L. The size of the computational box has to be large enough to accommodate the largest scales of the FST, in particular its width and height which does restrict the admissible inflowing FST modes. Therefore, different computational boxes have been chosen depending on the length scale L of the FST, see Table 1 and 2. The inflow Reynolds number is defined by the displacement thickness of the boundary layer at the inflow boundary of the computational domain (δ_0^*) and was chosen 300 for all cases; thus the laminar inflow is located at $Re_x \approx 30400$. All the quantities are non-dimensionalised with the inlet displacement thickness δ_0^* and the free-stream velocity U_∞.

3. Results

3.1. *Validation of the LES results*

The ADM-RT model has been shown to obtain accurate results at a fairly low computational cost in turbulent channel flows by Schlatter *et al.* (2004, 2006). Recently, this model has been extended also to include passive scalar by assuming a constant turbulent Prandtl number Pr_t being 0.6. A comparison with the DNS results obtained by Li *et al.* (2008) at $Re_\theta = 800$ is shown in Figure 1. In general, the results of both the velocity and heat transfer compare reasonably well with the DNS data, especially the turbulence intensities and the heat fluxes are predicted accurately. The larger discrepancies in the mean temperature profile are mainly due to the low resolution used in the streamwise direction. The grid spacing in the streamwise direction Δx^+ (the wall units are calculated based on the friction velocity u_τ at centre of the domain) for the present LES is about 60.

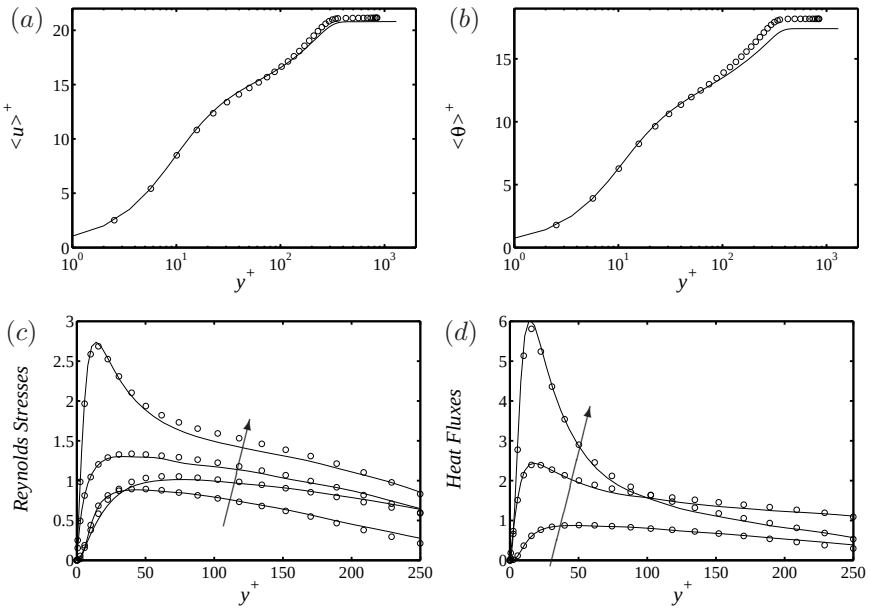

FIGURE 1. Validation of the LES results (Case 2) at $Re_\theta = 800$. ——Present LES data, ∘ DNS data from Li *et al.* (2008). (*a*) Mean streamwise velocity, (*b*) Mean temperature, (*c*) Reynolds stresses, the arrow indicates the quantities: $-\langle u'v'\rangle^+$, v^+_{rms}, w^+_{rms}, u^+_{rms}, (*d*) Heat fluxes, the arrow indicates the quantities: $-\langle v'\theta'\rangle^+$, θ^+_{rms}, $\langle u'\theta'\rangle^+$.

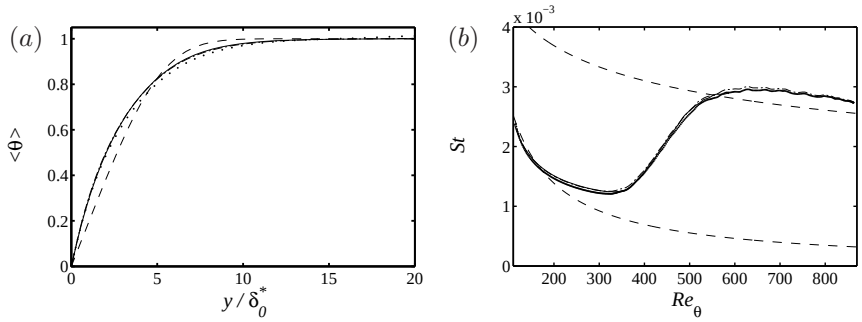

FIGURE 2. Influence of the thermal free-stream turbulence (Case 1). ——T_θ = 0%, –·–T_θ = 10%, ·····T_θ = 80%, (a) Mean temperature profile at $Re_\theta = 395$ ($Re_x = 210400$), – – –laminar temperature profile, (b) Stanton number, – – –laminar and turbulent correlation.

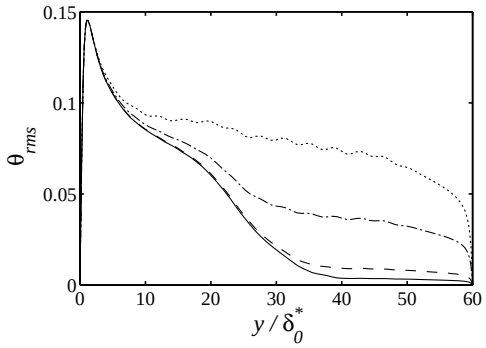

FIGURE 3. RMS fluctuation of the temperature at $Re_\theta = 790$ ($Re_x = 390400$) (Case 1). ——T_θ = 4%, – – –T_θ = 10%, –·–T_θ = 40%, ·····T_θ = 80%.

3.2. *Influence of the thermal free-stream turbulence T_θ*

The influence of the thermal free-stream turbulence $T_\theta = \theta_{rms}$ has been investigated in a smaller computational box (Box 1). In Figure 2, the mean temperature at a fixed downstream position, $Re_x = 210400$ or $Re_\theta = 395$, as well as the evolution of the Stanton number are shown. The laminar temperature profile is also included for comparison. For these cases, the velocity disturbance level is fixed at $Tu = 4.7\%$ while the thermal intensity T_θ is varied from 0% up to 80%. Nevertheless, the changes in the mean profile and the Stanton number are almost negligible. It can therefore be concluded that a higher fluctuation level of the temperature will not lead to an increased heat transfer at the wall. To further confirm these findings, the distributions of the

temperature fluctuations at $Re_x = 390400$ or $Re_\theta = 790$ are compared in Figure 3. Note that the decay of the fluctuations for $y > 45$ is due to the employed damping function in the free stream. The high levels of temperature fluctuations outside the boundary layer do not influence the growth of the streaky disturbances close to the wall. Consequently the heat transfer at the wall is not increased even for $T_\theta = 80\%$, as shown in Figure 2 (b). Therefore, only Tu will be considered afterwards, and T_θ is set to zero.

3.3. *Decay of the free-stream turbulence*

The FST is well characterised by both the turbulence intensity of the three different velocity components and a measure of the length scale together with energy spectrum. At the inlet, the generated FST is supposed to be nearly isotropic and homogeneous. In particular, the decay rate of the FST is similar to that of the grid turbulence widely used in the experiments. Figure 4 shows the downstream decay of the FST. Tu at different wall-normal positions above the boundary layer and the differences among the velocity intensity components indicate that the homogeneity and the isotropy of the FST are well achieved. It is possible to show that the decay obeys an power law and a more rapid decay of the FST for smaller length scale can be observed (not shown here) which is consistent with the previous results by Brandt *et al.* (2004).

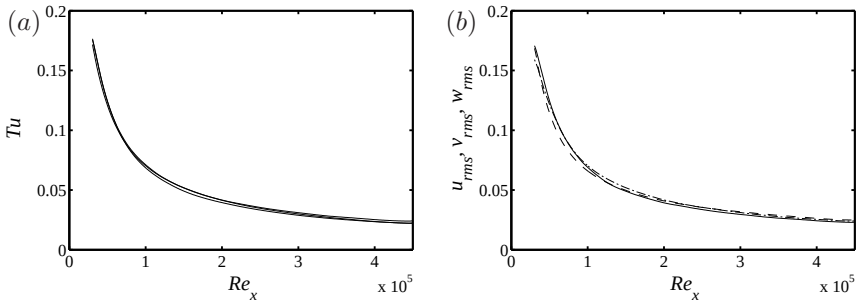

FIGURE 4. Downstream decay of the FST (Case 4). (a) Turbulence intensity versus the Reynolds number at $y = 50, 100, 150$ with $L = 7.5$, (b) Root-mean-square of the velocity fluctuations versus the Reynolds number at $y = 50$ with $L = 7.5$. ——— u_{rms}, - - - v_{rms}, —·— w_{rms}.

3.4. *Averaged results*

The averaging denoted by the angular brackets $\langle\rangle$ is performed over both the homogeneous spanwise direction and time. The corresponding fluctuating part is denoted by a prime. The influence of the free-stream turbulence level Tu and length scale L on the skin-friction coefficient c_f and the Stanton number St for

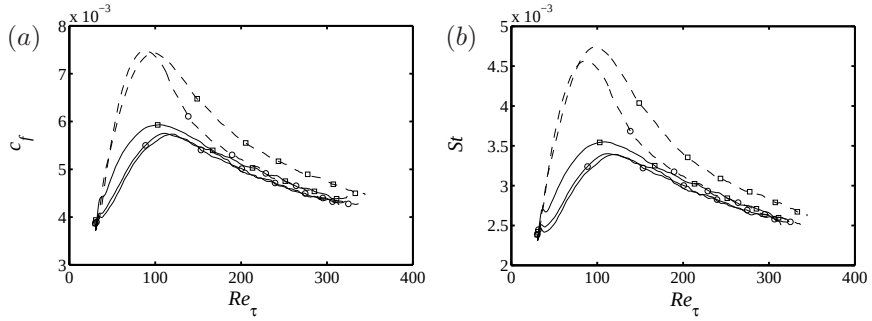

FIGURE 5. Influence of the turbulence intensity on the skin-friction coefficient c_f and Stanton number St. ——Case 2, –○–, Case 3 with $Tu = 4.7\%$, $L = 2.5$, –□–, Case 4 with $Tu = 4.7\%$, $L = 7.5$, – –○– –, Case 3 with $Tu = 20\%$, $L = 2.5$,– –□– –, Case 4 with $Tu = 20\%$, $L = 7.5$, (a) c_f, (b) St.

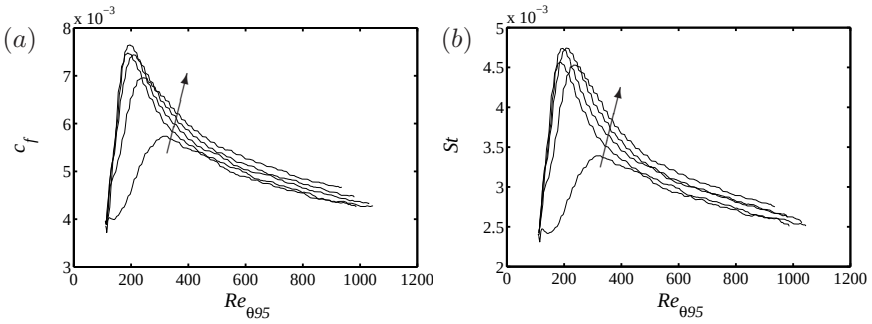

FIGURE 6. Influence of the length scale on the skin-friction coefficient c_f and Stanton number St with $Tu = 20\%$. The arrow indicates the increasing $L = [0, 2.5, 5, 7.5, 15]$. (a) c_f, (b) St.

$Pr = 0.71$ are shown in Figures 5 and 6. The present LES results of the skin-friction coefficient c_f and the Stanton number St from the no FST reference case (Case 2) are about 4% and 7% larger than the DNS results by Li *et al.* (2008). Consistent results for the skin-friction coefficient c_f compared to the previous numerical simulations, *e.g.* Brandt *et al.* (2004), can be established: For a higher turbulence intensity Tu, a clearly earlier transition to turbulence leading to an increase of c_f can be observed. A similar behaviour also applies to the Stanton number St. Different trends were observed in the simulations by Péneau *et al.* (2000). All the increases in the skin-friction coefficient c_f are about the same for the FST intensities investigated in their simulations from $7\% \sim 21\%$. Due to the small length scale $L = 2.5$, the effects from the FST are

much reduced (Hancock & Bradshaw 1983). The FST decays very rapidly and therefore the distributions of both skin-friction coefficient c_f and the Stanton number St are almost lying on top of the case with no FST in the fully turbulent region. Once the length scale is increased, the FST will decay slower and this will lead to elevation in both c_f and St. For the length scales examined in the present study, the larger the length scale is, the more the skin-friction coefficient and Stanton number will increase. However, the skin-friction coefficient and Stanton number will start decreasing if the length scale is too large compared to the boundary-layer thickness, assuming at a given FST level Tu (Hancock 1978). The reason for the decreased effects of the FST for increasing length scale is that the no-slip condition of the wall-normal velocity at the wall reduces the intensity of the wall-normal velocity component (Thomas & Hancock 1977). This effect is not observed in the present simulation due to the comparably small length scales of the generated FST. As noted by Blair (1983*a*,*b*), the impact of the length scale of the FST is to reach the maximum at $\frac{L_u}{\delta_{99}} = 1$ with L_u being the streamwise dissipation length scale and δ_{99} being the 99% boundary-layer thickness. For the ratio which is either significantly larger or smaller than unity, the effects would be expected to diminish.

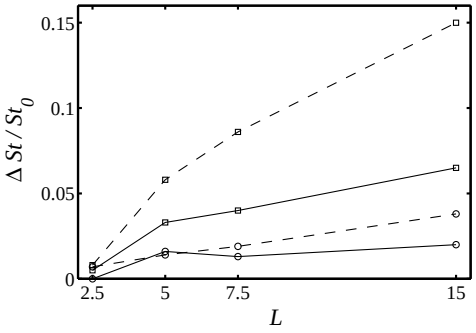

FIGURE 7. Increase of Stanton number St versus the length scale L. ——— at $Re_{\theta_{95}} = 800$, - - - at $Re_\tau = 300$, ∘ at $Tu = 4.7\%$, ▫ at $Tu = 20\%$.

The increases of St compared to Case 2, (*i.e.* no FST reference case, denoted by a suffix "0",) at $Re_{\theta_{95}} = 800$ and $Re_\tau = 300$ are plotted in Figure 7. Similar results are obtained also for c_f (not shown). In general, for both c_f and St when plotted against $Re_{\theta_{95}}$, the increase is less than when plotted against Re_τ. For the present simulations at $Re_\tau = 300$, a maximum of 15% for St at the turbulence intensity of 20% is achieved. However, Simonich & Bradshaw (1978) reported that at a nominal turbulence intensity of 7% in the fully turbulent region, 10% increase for c_f and 30% for St was observed. At essentially the same turbulence intensity, Blair (1983*a*,*b*) reported that both c_f and St increase as much as 20% in the fully turbulent region. In the simulations by

Péneau *et al.* (2000), an increase of 10% in c_f and 20% in St are obtained at a turbulence intensity of 21% at $Re_\theta \approx 1100$. At $Re_\theta = 800$, Jacobs & Durbin (2000) obtained about 5% increase in c_f and 12% in St with turbulence intensity around 4%. The considerably larger increase in St than in c_f observed in the experiments by Simonich & Bradshaw (1978) and the mentioned other simulations are not confirmed in the present simulations. This might be due to the present employed LES model and the low resolution used for the simulations. However, as pointed out in Maciejewski & Moffat (1992*a*,*b*), the larger effects observed by Simonich & Bradshaw (1978) are possiblely due to the change in the transition location on the flat plate. The FST for the present simulation decays fast compared to the experiments due to relatively small length scales. The local FST level at $Re_{\theta_{95}}$ or $Re_\tau = 300$ is less than 3% (see Figure 4). Taking this into account, 15% increases of both c_f and St for a local $Tu = 3\%$ are comparable to the experiments.

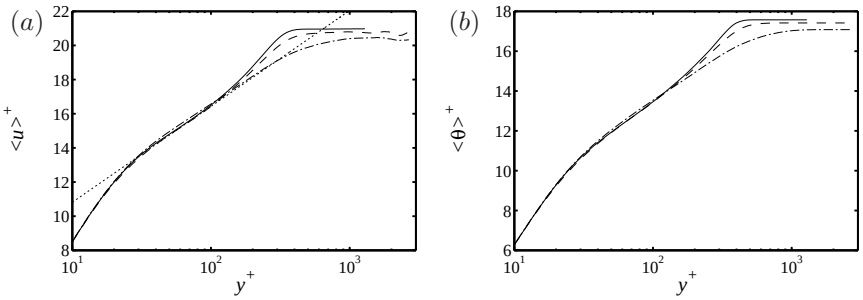

FIGURE 8. Influence of the FST on the mean profiles of velocity and temperature at $Re_{\theta_{95}} = 800$. ——— Case 2, - - - Case 4 with $Tu = 4.7\%$, $L = 15$, -·-·- Case 4 with $Tu = 20\%$, $L = 15$, ····· $\langle u \rangle^+ = \frac{1}{0.41} \ln y^+ + 5.2$. (*a*) $\langle u \rangle^+$, (*b*) $\langle \theta \rangle^+$.

The mean velocity and temperature profiles from Case 4 showing the influences of the FST are plotted in Figure 8. All of the profiles are taken at $Re_{\theta_{95}} = 800$. The log-law is also included for comparison. It is clearly seen that the profiles in the logarithmic region are insensitive to the FST whereas in the wake region significant depression of the boundary-layer wake starts appearing. Especially for the case of $Tu = 20\%$, the wake region even vanishes. For the temperature profiles, a similar conclusion can be drawn, *i.e.* only the wake region is influenced by the FST while the viscous sub-layer and logarithmic region are unchanged. These results are consistent with the previous experimental work by Blair (1983*a*,*b*). However, Maciejewski & Moffat (1992*a*,*b*) reported that only for the temperature profile, the depression extends even below the wake region down to the logarithmic region. The results by Péneau *et al.* (2000) show that the slope of the logarithmic region varies significantly with Tu for the temperature profile, which can not be confirmed here.

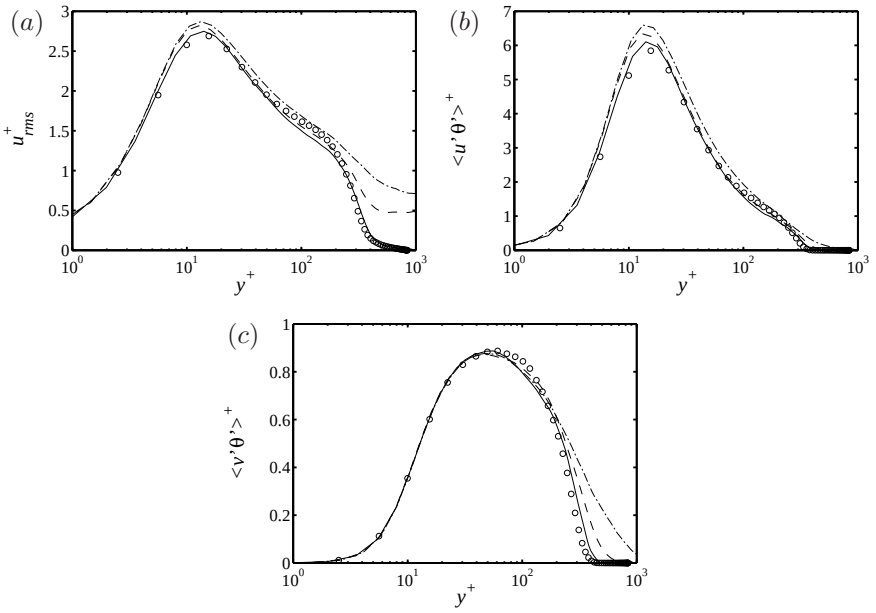

FIGURE 9. Influence of the FST on the turbulent intensity, heat fluxes and turbulent Prandtl number at $Re_{\theta_{95}} = 800$. ——Case 2, – – –Case 4 with $Tu = 4.7\%$, $L = 15$, —·—Case 4 with $Tu = 20\%$, $L = 15$, ∘ DNS data from Li *et al.* (2008). (*a*) u^+_{rms}, (*b*) $\langle u'\theta'\rangle^+$, (*c*) $\langle v'\theta'\rangle^+$.

The RMS fluctuation of the streamwise velocity for different turbulence intensities together with the DNS data from Li *et al.* (2008) are shown in Figure 9 (*a*). A slight increase of the peak value and a decrease of the peak position from the wall for the u_{rms} are observed. The relatively large increase far away from the wall, *i.e.* $y^+ > 200$, due to the FST is also noticeable. A similar behaviour also exists for the temperature fluctuations. On the contrary, the shear stress $\langle u'v'\rangle^+$ (not shown here) and the wall-normal heat flux $\langle v'\theta'\rangle^+$ remain unchanged except in the outer part of the boundary layer. The reason for the unaltered profiles of $\langle u'v'\rangle^+$ and $\langle v'\theta'\rangle^+$ in the near-wall region might be that the perturbations enter the boundary layer mainly in the streamwise velocity component (Brandt *et al.* 2004). However, Péneau *et al.* (2000) observed a different trend: The peak values of $\langle u'v'\rangle^+$ and $\langle v'\theta'\rangle^+$ are increased considerably in both the logarithmic and wake region and the peak positions are displaced noticeably towards the wake.

4. Conclusions and outlook

Simulations of turbulent boundary-layer flow with heat transfer under the influence of free-stream turbulence have been performed. Since the behaviour of

the velocity disturbances inside and outside the boundary layer for a transitional case is well understood, see *e.g.* Brandt *et al.* (2004), the focus of the present contribution is to examine the influences of the ambient turbulence on momentum and heat transfer in a fully turbulent flow; in particular whether an increased Stanton number can be observed for high turbulence intensities.

A detailed parameter study varying both the turbulence intensity and the length scale of the velocity has been conducted. In particular, the simulation domains are chosen large enough such that the relevant part of turbulent boundary-layer flow can be included in the computational domain. The results obtained are consistent with previous observations. The LES results with no FST are validated against the DNS results and the agreement in general is reasonably good.

The mean velocity and temperature profiles are unaffected by the FST in the viscous sub-layer and the logarithmic region. On the other hand, more depression of the wake region can be observed with increasing turbulence intensity. Both the skin-friction coefficient and the Stanton number increase with increasing free-stream turbulence intensity (as much as 15% for a nominal turbulence intensity of 20% at the inlet). Taking into account the low local turbulence intensity, the increase is on the same level as observed in the experiments. In the future, to validate the heat-transfer results with FST, a series of direct numerical simulations shall be carried out to ensure the accuracy of the current LES predictions.

References

Blair, M. F. 1983*a* Influence of free-stream turbulence on turbulent boundary layer heat transfer and mean profile development, Part I – Experimental data. *ASME J. Heat Transfer* **105**, 33–40.

Blair, M. F. 1983*b* Influence of free-stream turbulence on turbulent boundary layer heat transfer and mean profile development, Part II – Analysis of results. *ASME J. Heat Transfer* **105**, 41–47.

Bradshaw, P. 1974 Effect of free-stream turbulence on turbulent shear layers. *Tech. Rep* Aero Report 74-10. Imperial College of Science and Technology, Department of Aeronautics, London, U.K.

Brandt, L., Schlatter, P. & Henningson, D. S. 2004 Transition in boundary layers subject to free-stream turbulence. *J. Fluid Mech.* **517**, 167–198.

Chevalier, M., Schlatter, P., Lundbladh, A. & Henningson, D. S. 2007 A pseudo-spectral solver for incompressible boundary layer flows. *Tech. Rep* TRITA-MEK 2007:07. Royal Institute of Technology, Stockholm.

Hancock, P. E. 1978 Effect of free-stream turbulence on turbulent boundary layers. PhD thesis, Imperial College of Science and Technology, London, U.K.

Hancock, P. E. & Bradshaw, P. 1983 The effect of free-stream turbulence on turbulent boundary layers. *ASME J. Fluids Engng.* **105**, 284–289.

Hancock, P. E. & Bradshaw, P. 1989 Turbulence structure of a boundary layer beneath a turbulent free stream. *J. Fluid Mech.* **205**, 45–76.

Jacobs, R. G. & Durbin, P. A. 2000 Bypass transition phenomena studies by computer simulation. *Tech. Rep* TF-77. Stanford University, U.S.A.

Li, Q., Schlatter, P., Brandt, L. & Henningson, D. S. 2008 Direct numerical simulation of a turbulent boundary layer with passive scalar transport. In *Direct and Large-Eddy Simulation VII*. Springer-Verlag, Berlin.

Maciejewski, P. K. & Moffat, R. J. 1992*a* Heat transfer with very high free-stream turbulence. I: Experimental data. *ASME J. Heat Transfer* **114** (4), 827–833.

Maciejewski, P. K. & Moffat, R. J. 1992*b* Heat transfer with very high free-stream turbulence. II: Analysis of results. *ASME J. Heat Transfer* **114** (4), 834–839.

Péneau, F., Boisson, H. C. & Djilali, D. 2000 Large eddy simulation of the influence of high free-stream turbulence on a spatially evolving boundary layer. *Int. J. Heat Fluid Flow* **21** (5), 640–647.

Péneau, F., Boisson, H. C., Kondjoyan, A. & Djilali, D. 2004 Structure of a flat plate boundary layer subjected to free-stream turbulence. *Int. J. Comput. Fluid Dynamics* **18** (2), 175–188.

Schlatter, P., Stolz, S. & Kleiser, L. 2004 LES of transitional flows using the approximate deconvolution model. *Int. J. Heat Fluid Flow* **25** (3), 549–558.

Schlatter, P., Stolz, S. & Kleiser, L. 2006 LES of spatial transition in plane channel flow. *J. Turbulence* **7** (33), 1–24.

Simonich, J. C. & Bradshaw, P. 1978 Effect of free-stream turbulence on heat transfer through a turbulent boundary layer. *ASME J. Heat Transfer* **100** (4), 671–677.

Tennekes, H. & Lumley, J. L. 1972 *A First Course in Turbulence*. The MIT Press, Cambridge, U.S.A.

Thomas, N. H. & Hancock, P. E. 1977 Grid turbulence near a moving wall. *J. Fluid Mech.* **82**, 481–496.